THE EFFECT OF MICROCARS' LIGHTNESS AND COMPACTNESS ON SAFETY IN SIDE IMPACTS

Tetsuya Matsushita
Takayuki Shimizu
Shuichi Osato
Autoliv Japan Ltd.
Japan

Paper number 23-0027

ABSTRACT

In this paper, the term 'microcar' refers to a car which is categorized as L7 by the UN and conforms to the Ultra Compact Mobility regulation in Japan. The car is much lighter and smaller than a conventional passenger vehicle. It is generally understood that a microcar has poorer crash safety performance than a conventional passenger car. In particular, the microcar would seem to have a disadvantage in terms of side-crash protection performance, since a smaller gap between an occupant and the door means a shorter distance to absorb the impact energy. On the other hand, having a lighter mass, it moves earlier when struck, meaning that the speed and depth of the door intrusion is reduced: an advantage. Thus the severity of a microcar side crash is not obvious. The aim of this study is to find out how the lightness and compactness of the microcar affect its side-crash protection performance.

This study was conducted using a numerical simulation of a Japanese K-car full-vehicle model. Two kinds of parameters were created. One is the Vehicle mass, the other is the Gap between the door inner panel and an occupant.

Three levels of mass were investigated (351 kg, 658 kg, and 1000 kg) by removing parts which do not contribute to vehicle body strength or adding weight to the center of gravity. The UN R95 load case was selected for the evaluation. To simulate the microcar, the crash dummy and the seat were repositioned outboard laterally from the original position, the seatbelt was fastened without a pretensioner, and there was no airbag.

The struck microcar's velocity was obviously affected by its vehicle mass: the lighter the mass, the sooner the vehicle moved after the Moving Deformable Barrier (MDB) impact. However, the door velocity profile was almost the same in every vehicle mass condition up to the time of the peak injury value, so the injuries were at the same level—except for the head region, which was impacted by the roof rail. The lighter vehicle produced the higher head impact velocity, resulting in higher head injury values.

As for the effect of door clearance, larger clearance seemed to reduce the injury level—slightly but demonstrably.

This study indicated that the effect of vehicle mass (in the 358 kg–1000 kg range) on crash severity seems to be very small for the chest-to-pelvis region. On the other hand, the lighter vehicle mass seems to carry a higher injury risk for the head region. Thus it is suggested that the focus for microcars' side-impact safety should be on protection performance for the head rather than the chest-to-pelvis area.

INTRODUCTION

Reflecting zero-emission vehicle requirements in this decade, small Electric Vehicles (EV) have been developed all over the world as one solution. These vehicles are seen mostly in Europe, China, and Japan. Europe and Japan already have official categories for EVs, and China has announced that Micro EV unique safety ratings will start soon in their New Car Assessment Program (NCAP).

The cars in the L7 category defined by the United Nations (UN), and the Ultra-Compact Mobility (UCM) category recently defined in Japan, are characterized by their small size and light weight. They are even smaller and lighter than a K-car, which is a major category in Japan. In this paper these L7 and UCM cars are called microcars. The definitions of L7, UCM, and K-car are shown in Tables 1 to 3 as a reference.

There is not much literature which describes the safety of this kind of car, although the EuroNCAP did release the results of the frontal-crash and side-crash tests for L7-category quadricycles in 2014 [1] and 2016 [2] as their safety campaign. Although the test protocol was a little more relaxed than the one for normal passenger cars, the results indicated very high injury risks for every tested vehicle.

Innovative micro-size concept cars equipped with a lightweight, stiff structure and high-performance restraint system have been developed, with the general understanding that a smaller vehicle has a higher injury risk than

a larger vehicle. Unselt et al. [3] created an ultra-compact electric vehicle concept named Visio.M which has a carbon fiber-reinforced plastic monocoque body, an aluminum crush structure, and advanced airbags (both inside the cabin and at the front of the body structure) to protect occupants by increasing energy absorption in a frontal crash. The concept achieved protection performance equivalent to normal passenger cars in both front- and side-crash tests. Fresnillo et al. [4] created a lightweight electric vehicle concept of similar size named BEHICLE, applying sandwich panels and foam to realize the light weight. In their unique concept, a driver is seated in the center in order to acquire enough clearance to the door panel to provide side-crash protection. In addition, the driver seat is equipped with a 4-point seatbelt system. The concept boasted excellent side-crash protection performance and acceptable front-crash protection performance, although it appears to be very expensive and looks much different than the current generic microcar.

In a frontal collision, when a small vehicle and a large vehicle crash, the small vehicle has the disadvantage in terms of protection performance. The issue has been understood as an incompatibility, and several methods to assess it have been proposed [5] [6]. The EuroNCAP started a compatibility rating in 2020 [7]. Mizuno et al. [8] clearly explain the disadvantage of small vehicles (K-cars in their paper), comparing data on deceleration levels, ride-down efficiency, injury severity, and firewall intrusion to other sizes of vehicle.

Because a microcar is one of the smallest vehicle categories, the collision partner will just about always be a larger and heavier vehicle; we have to realize that this load case is normal for microcars. It is difficult for microcars to have a sufficient crushable zone in front of the cabin to absorb the impact energy from larger vehicles. Thus it is natural that the microcar has a disadvantage in front-crash protection performance.

What about side impacts? Barbat et al. [9] evaluated which elements of geometry, stiffness, and mass are most relevant for determining crash severity; however, the striking vehicle mass ranged from 1680 kg to 2360kg, and was (as a single parameter) 1724 kg for the struck vehicle, which is far from the mass of a microcar. The main purpose of their paper was to grade the effect level of each parameter; in this paper, we focus on the mass parameter of the struck vehicle alone. Terazawa et al. [10] evaluated the side-impact protection performance of a microcar with full-scale physical testing. Their object vehicle was even smaller than the microcar defined in this paper and had no side door. In addition, the impact speed was 30kph, which is much lower than Japan's UCM regulation. Furthermore, the only injury probability evaluated was for the pelvis.

We have not found any literature that clearly explains how a microcar's compactness and light weight affect the occupant protection performance in a side crash from an injury mechanism approach. However, in spite of the lack of research, some effects can be inferred from the laws of physics. Downsizing certainly has the disadvantage that the gap between the door and the occupant becomes smaller, so there is less time and distance for the absorption of the impact energy, and the peak load to the occupant is greater. However, a lighter weight vehicle tends to move faster than a heavy vehicle when it is struck. It can be expected that the amount of door intrusion tends to be smaller than that of heavier vehicles, because the intrusion can be calculated as the time integral of the door's relative velocity against the moving vehicle body's velocity: when the moving body's velocity increases, the door's relative velocity decreases. This is an advantage for the occupant protection performance. When these facts are considered together, it is difficult to conclude whether the compactness and lightness result in an overall advantage or disadvantage in terms of crash safety performance. The aim of this paper is to clarify how the small size and light weight of the microcar affect the occupant protection system performance in a side collision using an injury mechanism approach.

As a side note, Davies et al. [11] indicated injury risks induced from the small car features and analyzed a crash case by reviewing the statistical data. Considering small cars' unique features together with the needs of the market and society, they proposed that a different safety assessment be developed, rather than applying the existing one which focuses on normal passenger cars.

Table 1.
L7 category definition

L7 vehicle image	Description
	✧ Vehicle weight (passenger) ≤ 400 kg (exclude battery for EV) ✧ Vehicle weight (commercial) ≤ 550 kg (exclude battery for EV) ✧ Maximum speed ≥ 45 kph ✧ Max. Net Power ≤ 15 kW ✧ No definition of vehicle size

Table 2.
Japanese UCM definition

UCM vehicle image	Description

	◇ Length: ≦ 2.5m
	◇ Width: ≦ 1.3m
	◇ Height: ≦ 2.0m
	◇ Rated power: ≧0.6kW
	◇ Max traveling speed: 60km/h
	◇ Sticker stating the vehicle must be driven < 60km/h shall be pasted on rear window
	◇ Not allowed on motorway
	◇ Crash regulations
	  ✓ UN R137: Full Rigid Barrier 40km/h
	  ✓ UN R94: Offset Deformable Barrier 40km/h
	  ✓ UN R95: Side MDB 50km/h

Table 3.
Japanese K-car definition

K-car vehicle image	Description
	◇ Length: ≦ 3.4m ◇ Width: ≦ 1.48m ◇ Height: ≦ 2.0m ◇ Displacement: ≦ 660 cc ◇ Rated power: ≧ 47kW ◇ Crash regulations ✓ Same as normal passenger cars

METHOD

All evaluations were performed by numerical simulation. It is difficult to define a generic microcar model, since no microcar model has ever been shared as an open source. However, there are many evaluation reports from Japan NCAP (JNCAP) regarding the Japanese K-car, the world's most widely available small car. Therefore, we have chosen a K-car sedan as the base model, modified to reflect the microcar features. In order to evaluate the effect of the lightness and compactness, two parameters were used: the vehicle mass and the gap between the inner door panel and the occupant.

For the vehicle mass parameter, three models were created. As a baseline, the base K-car model was applied as is; in addition, a lighter model was created by removing components from the base, and a heavier model was created by adding balance weights to the center of gravity. The adjusted masses are 351 kg, 658 kg, and 1000 kg, reflecting a microcar, the lightest (base) K-car, and the heaviest K-car, respectively. The distribution of the K-cars' masses, using data collected from models sold in the Japanese market in 2022 (65 cars), is illustrated in Figure 1. The data on the distribution of microcars' masses, in Figure 2, were collected from the available cars in the Japanese market in 2022 (11 cars).

Two models were created for the gap-to-door parameter. As a baseline, the K-car model as is was used. The second model, simulating the microcar, shortened the gap by 33mm by moving the occupant and the seat laterally outboard. The original gap setting was obtained from one microcar sold in Japan.

In order to evaluate the above two parameters, other conditions were held constant, as described below.

The occupant model was a well-known side impact Anthropomorphic Test Device (ATD), ES2. It was seated on the driver's seat according to the United Nation Regulation No.95 (UN R95) test protocol. The restraint system was modeled on a simple, low-cost system, given the price range of microcars. The seatbelt had only a locking function (when the belt is pulled out rapidly in an emergency), and there was no pretensioner (to reduce belt

slack in a crash) or load limiter (to avoid excessive belt tension). Side and curtain airbags were not installed, both to simulate the basic microcar and to avoid complicating mechanical factors.

The UN R95 load case condition for Moving Deformable Barrier (MDB) impact was applied. It is well known as a major testing protocol for automotive safety experts, and Japan adopted it as the side-crash regulation for UCM in 2021. This load case was selected since it is the one prioritized for side crashes in Japan. Every velocity evaluated in this paper is relative to the ground. Further details of the evaluation settings are explained below.
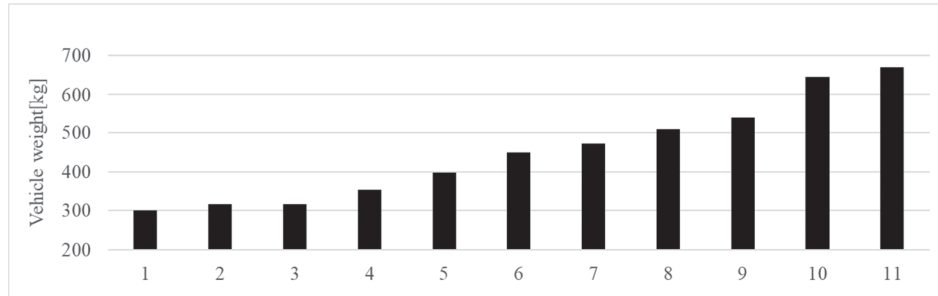

Figure 1. Microcar Mass Distribution in Japan

Figure 2. K-car Mass Distribution in Japan

Vehicle mass adjusted for Lighter model: 351 kg
The parts listed in Table 4 were removed. Before removal, the stress level of every part was reviewed to ensure that it underwent no stress in a side crash.

Table 4.
Removed parts list

Engine Compartment	Steering	Relay Box Right	Canister
Fuel Tank	Radiator	ABS	EPI
Door Metal Front Left	Hood	Air Cleaner	Horn
Back Door	Seat Rear	AB Pipe	Fuse Box
Door Metal Rear Left	Bumper Front	Fuel Pipe	
Seat Front Left	Relay Box Left	Head Lamp Left	
Battery	Wiper Front	Head Lamp Right	
Weight	Master Vac	Cowl Top	
Exhaust Pipe	Fender Left	Pedal	
Unit IP	Center Console	Glass Wind Shield	

Vehicle mass adjusted for Heavier model: 1000 kg
The weights were placed at the center of gravity of the vehicle.

Sensor location

In order to measure the velocities of the vehicle and the door intrusion, accelerometers were placed at appropriate locations. For the vehicle velocity, to avoid impact vibration noises, the side sill of the unstruck side was chosen, at the longitudinal center of the vehicle geometrically.

To measure door intrusion, three measuring points (UPR, MID, and LWR, as shown in Figure 3), corresponding to the ES2's body regions of chest, abdomen, and pelvis, respectively, were positioned on the driver door.
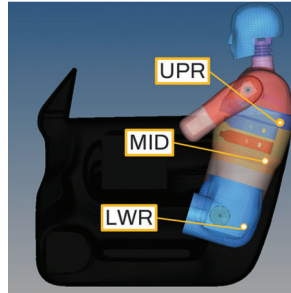

Figure 3. Accelerometer locations on the door

Gap-to-door setting

As noted, the gap between the ES2 and door panel was set to one of two distances. One, the K-car equivalent, is the original gap of the base K-car as is. The other, the microcar equivalent, comes from the benchmarked microcar—adjusted to the same clearance at the pelvis by moving the ES2 outboard (the seat was moved the same distance). The gaps are illustrated in Figure 4.
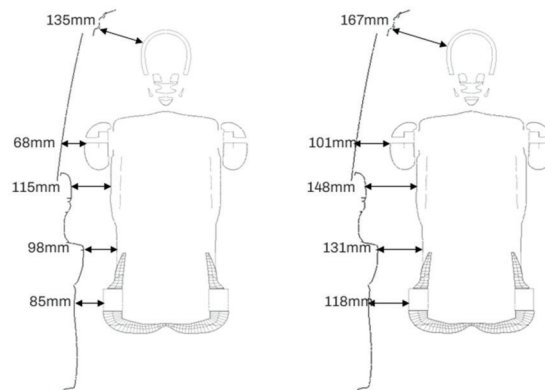

Figure 4. Gap-to-door (Left: microcar equivalent, Right: K-car equivalent)

Occupant model description

Side impact ATD of ES2 was selected. It represents the size of the 50%ile adult male, adapted to the UN R95 protocol. The model is produced by LSTC, version V0.101.

In order to evaluate how much external force is loaded onto which body regions, the contact areas were defined as in Figure 5.
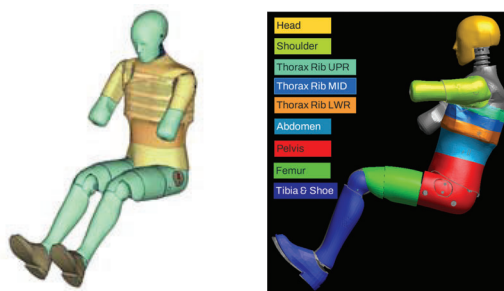

Figure 5. Contact area definitions of ES2

Crash condition

The key information about the UN R95 lateral collision test protocol is shown in Figure 6. Reflecting right-hand drive in Japan, the MDB strikes the right-hand side. The driver is the only occupant of the vehicle.
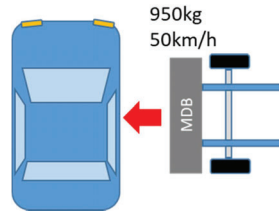

Figure 6. Crash condition

Test Matrix

The test matrix is shown in Table 5.

Table 5.
Test matrix

ID#	Gap-to-door	Vehicle Mass	Load case	ATD	with Seatbelt	with Airbag
1	microcar	351 kg	UN R95	ES2	Yes	No
2	↑	658 kg	↑	↑	↑	↑
3	↑	1000 kg	↑	↑	↑	↑
4	K-car	351 kg	↑	↑	↑	↑
5	↑	658 kg	↑	↑	↑	↑
6	↑	1000 kg	↑	↑	↑	↑

RESULTS

Velocity profiles: MDB and Vehicle

The results of IDs# 1 to 3 are overlaid onto Figure 7, left, to demonstrate the vehicle mass effect in the microcar gap condition. Hereinafter the striking vehicle is called the "MDB" and the struck vehicle is called the "Vehicle". The lighter the vehicle, the higher and earlier the end velocity. This result is no surprise, since it merely complies with the laws of physics.

The MDB velocity profile, rather, should be focused on. Because the MDB front surface and the vehicle door merge just after the door has been crushed, in principle the MDB velocity is correlated with door intrusion velocity, which is one of the most critical causes of occupant injuries. The change in MDB velocity is much slower than that of the vehicle. The obvious change can be seen after 40ms.

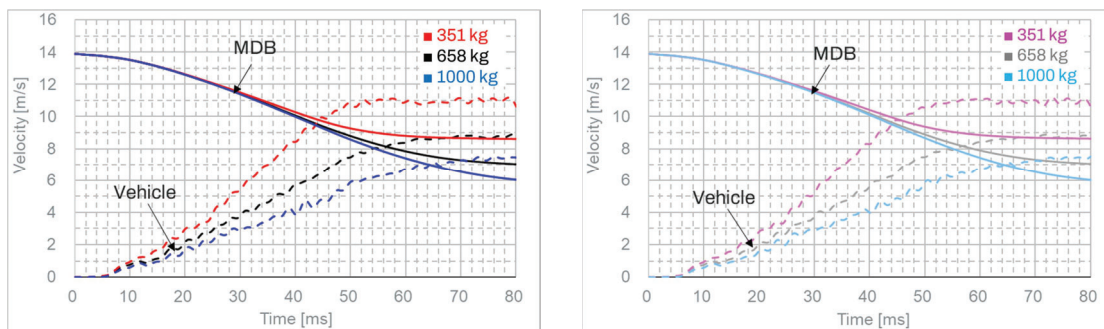The same trend is indicated for the K-car gap condition of IDs# 4 to 6, shown in Figure 7, right.

Figure 7. Velocity of MDB and Vehicle (Left: IDs#1–3, Right: IDs#4–6)

Injury indicator Summary

The Injury indicators of IDs# 1 to 3 are summarized in Figure 8, to demonstrate the vehicle mass effect in microcar gap condition. The evaluated injury indicators are Head Injury Criterion 36 (HIC36) for the head, Thorax Rib deflection for the chest, Abdomen force for the abdomen, and Pubic force for the pelvis. These are the major injury risk indicators for regulations and NCAPs globally. The regulation threshold values are shown as 100% in the graphs; lower percentage means lower injury risk.

The results at chest and pelvis were no different regardless of the Vehicle mass. This is due to the similarities of the door speed velocity profiles (illustrated in Figure 10). The results at the head were high percentages for the Vehicle masses of 351kg and 658kg, exceeding 200% of regulation threshold. In these tests, the roof rail of the Vehicle impacted the occupant's head, due to the fact that the Vehicle moving speed and acceleration increase as the vehicle becomes lighter as explained in the former paragraph.

It is the same pattern of results for the K-car gap condition of IDs# 4 to 6, the lighter vehicle produced the drastically higher HIC36 injury values and similar injury values at chest and pelvis, are indicated, shown in Figure 9.
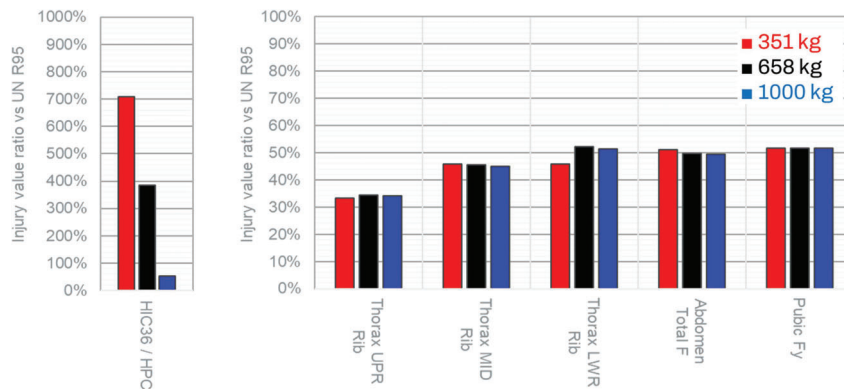

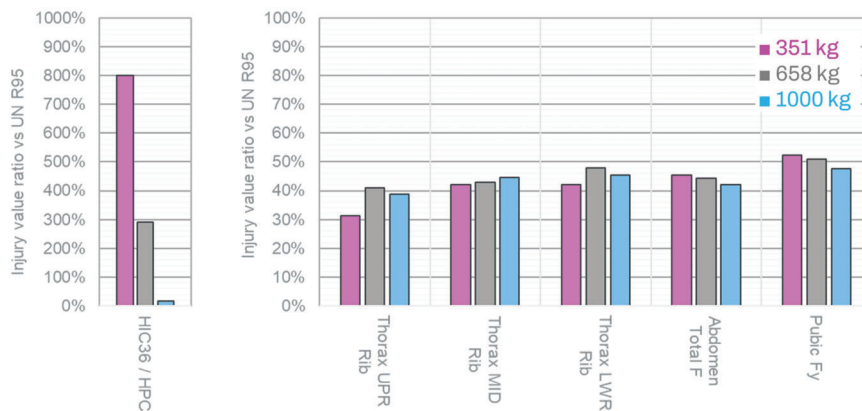*Figure 8. The injury values as percentages of the regulation threshold (IDs#1–3)*

Figure 9. The injury values as percentages of the regulation threshold (IDs#4–6)

Door Velocity

The door velocity was measured at three points to evaluate how the door impacts the ES2 (Figure 3).

The velocity profiles are illustrated in Figure 10. At the left is the microcar Gap case, at the right the K-car case. The red vertical line indicates the timing of the peak injury value. The door UPR graph shows the Chest deflection, door MID shows the Abdomen force, and door LWR shows the Pelvic force. Because the timing was slightly different depending on the Vehicle mass, the line thickness indicates the range from the earliest to latest peak timing of each case. Every UPR, MID, and LWR location resulted in a very similar profile regardless of the Vehicle mass, until the time of the peak injury value. The K-car Gap case produced very similar profiles, regardless of the Vehicle mass.
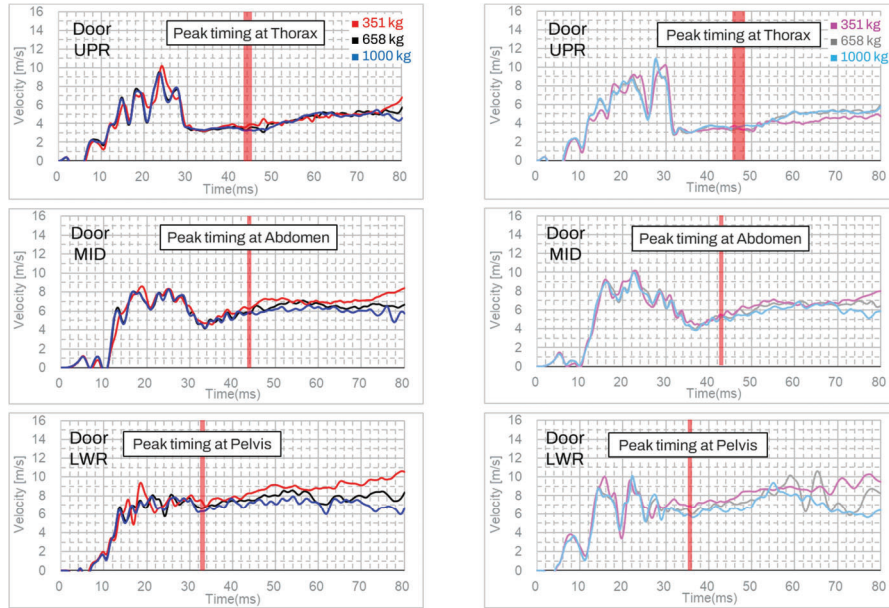
Figure 10. Door Velocity (Left: IDs#1–3, Right: IDs#4–6)
red vertical line indicates range of timing for injury peak

ATD Velocity

Impact severity at the ATD is assessed by measuring its moving velocity. The velocities were measured at T1 (first thoracic vertebra), T12 (twelfth thoracic vertebra), and the Pelvis. The results are illustrated in Figure 11. The velocity profiles were almost the same regardless of the Vehicle mass until the injury value reached its peak, for all three locations. The left graphs in Figure 11 show the results of the microcar gap cases (IDs# 1–3) and those on the right show the K-car gap cases (IDs# 4–6). For the chest (thorax) region, it was confirmed that the impact severity for ES2 did not depend on the Vehicle mass, as stated previously. As in the Door velocity graphs, the thickness of the red vertical line indicates the range from the earliest to latest peak timing of each case.
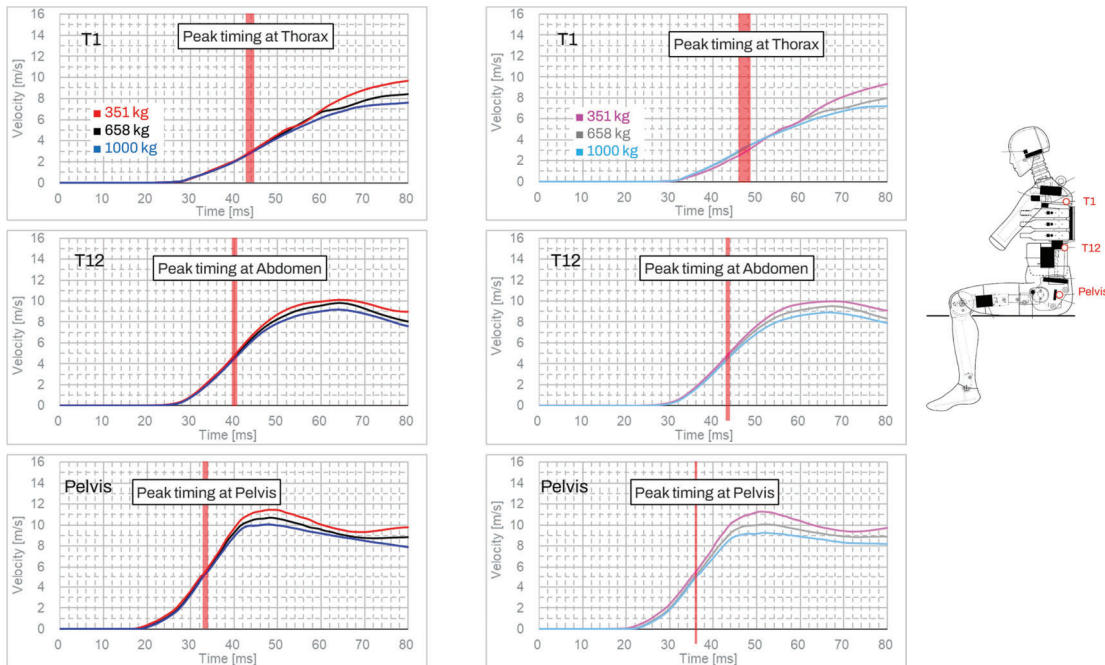

Figure 11. ATD moving Velocity (Left: IDs#1–3, Right: IDs#4–6)
red vertical line indicates range of timing for injury peak

Door intrusion

The door velocity was given in Figure 10 and the Vehicle moving velocity was given in Figure 7. The door intrusion displacement can be calculated as the time integral of the door velocity relative to the Vehicle moving velocity; the peak intrusion results are illustrated in Figure 12. The left is the microcar Gap condition, and the right is the K-car Gap condition. The graphs clearly indicate that the lighter the vehicle, the smaller the door intrusion, and vice versa.
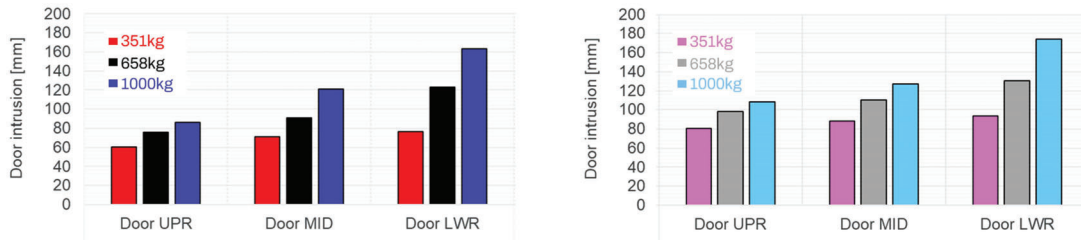

Figure 12. Door intrusion (Left: IDs#1–3, Right: IDs#4–6)

Gap effect

Figure 13 shows the effect of the Gap for each of the Vehicle mass conditions. For the MID and LWR regions, the K-car Gap injury ratios were less than those of the microcar Gap in every Vehicle mass condition.

However, for the HIC36 and UPR regions, the difference between the two Gap distances did not seem to follow a pattern; for example, in the 351kg case, the K-car gap produced a higher HIC36—but in the 658kg case the microcar gap produced a higher HIC36. The reason is that when the side window breaks later, it can restrain the shoulder longer, reducing the head's potential kinetic energy; as a result, head injury can be reduced. It appears that the higher the UPR deflection, the lower the HIC36 injury, and vice versa. Based on this observation, the side window of the 351kg vehicle was broken earlier than its counterpart in the heavier vehicles. Since the lighter vehicle has the larger inertia force in the crash, it leads to quicker and larger deformation of the door.

The direct injury factor of the contact force between the door and ES2 is shown in Figure 14, indicating clearly that the wave shape is similar even in the different gap conditions, although the timing differs. The peak forces of the K-car Gap were a little less than those of the microcar Gap. The graphs in Figure 14 show the 351kg case; the other Vehicle mass cases show the same trend.

The actual timing of the side window's breakage depends on a vehicle's design. However, a generic evaluation of the Gap effect can be made: a larger Gap has the potential to reduce injury levels even in these small cars with tiny door clearance. The potential injury reduction is slight but demonstrable.
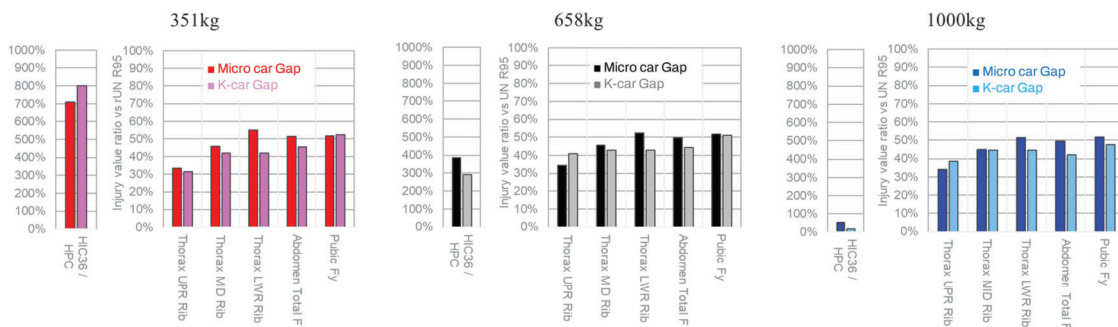

Figure 13. The injury values as percentages of the regulation threshold ; microcar gap vs K-car gap
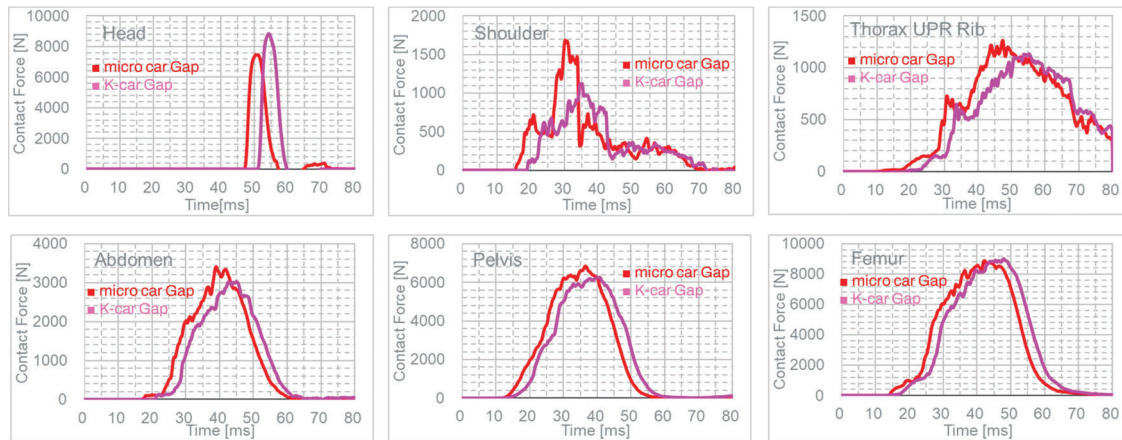
Figure 14. Contact force between door and ATD; microcar gap vs K-car gap (351kg Vehicle mass)

DISCUSSION

Same injury level regardless of the Vehicle mass

Although the head injury level was affected by the Vehicle mass, the chest-to-pelvis region injury level was not affected. The mechanism is explained below. The severity levels at the various regions are related to how the door impacts the side of occupant, and the most reasonable indicator of door impact severity is door velocity. This logic is supported by the work of Sunnevång et al. [12], who compared the occupant protection performance of modern versus older cars, using indicators of Door velocity and chest deflection. The indicators showed good correlation. In our study, the door velocities did not vary, regardless of the Vehicle mass, up until the time of the injury indicator peak.

The MDB velocity profiles were also almost all the same, until the time of the injury indicator peak. The merged final velocity of the MDB and Vehicle complies with the law of conservation of momentum; however, the temporal process was different from our expectation. The velocity of the MDB changed more slowly than that of the Vehicle: the difference can be seen after the injury peak.

Other interior parts have the potential to affect injuries in a crash event, such as the seat and seatbelt, which contact the occupant. The seatbelt applied in our tests did not have a pretensioner, so it could not create effective restraint friction, and the seat was responsible for only a small friction force through the seat cushion.

In summary, an occupant is in contact with the door, seatbelt, and seat in a crash. The most critical factor, the door velocity, remained almost the same because of the slow MDB velocity change; the other factors, seatbelt and seat, could not change very much—that is, the mechanism of injury is the same regardless of the Vehicle mass. This summary applies to the chest-to-pelvis region, not the head region.

A larger Gap has greater safety potential

Although there was almost no effect of Vehicle mass, the Gap parameter demonstrated some effects. As discussed, the biggest injury-causing impact element is the door, and the MDB velocity and Door velocity should be correlated in principle. As seen in Figure 7, the ES2 started to move at 20ms (Figure 11); the MDB velocity (= door velocity) at this point is nearly 13m/s, and the difference between the two Gap conditions is 33mm. The time duration to intrude 33mm is approximately 2ms, so we can calculate the difference in door impact velocity between the two, in this case approximately 0.2–0.3m/s—which can be roughly estimated from Figure 7. Velocity is squared for impact energy calculation, so even a slight difference in velocity can make a big difference in impact. Thus it can be said that the larger Gap definitely contributes to improved side-crash protection performance. The cabin of a microcar does not have any room to spare, but somehow (perhaps with seat layout) the challenge of making a larger Gap should be explored.

As one example of addressing this challenge, the CITROEN AMI (Figure 15) has a unique seat layout: the driver seat and front passenger seat are offset fore and aft, allowing the front seats to be closer than those in other microcars. We expect that this layout creates as large a door clearance as possible while avoiding interaction between occupants' shoulders. This type of innovation is needed to achieve user comfort, acceptable safety, and a reasonable price at the same time.

Figure 15. CITROEN AMI: Seat Layout

Head injury
This study indicated that the head could be impacted by the roof rail, whose velocity is affected by the Vehicle mass: the lighter the vehicle, the higher the impact velocity. As a result, the microcar has more need for head protection than larger, normal passenger cars. The head is an important body region which must be protected to avoid severe injuries. Although it is understood that a microcar will have a super low cost, the risk of head injury has to be reduced as much as possible.

As one solution, a higher roof which could avoid head impact is suggested. This requirement would restrict the design freedom, and some potential for neck injury could be expected instead, but it is just one of many ideas which will hopefully be proposed in the future.

LIMITATIONS

A K-car has a monocoque body structure like a normal passenger car, but a microcar would not normally have that kind of structure, considering the production volume and the tooling cost. It is not easy to determine which body structure would have a safety advantage. While there are many other possible kinds of structure (like ladder frame or pipe frame), this paper is based on a microcar with a monocoque structure.

In addition to the structure, benchmarking the microcar category, the material should be discussed. Microcars use resin a lot rather than metal, which might affect the body and door deformation characteristics.

Finally, the door thickness varies greatly, depending on the make of microcar, but generally microcars have thinner doors than K-cars. This difference means that the door contact timing to ES2 would be earlier than it was in our simulations, so the door impact velocity would be higher than in a K-car. As a result, the severity would be higher than reported in this paper.

CONCLUSION

The remarkable feature of a microcar is its small size and light weight. In this paper, we evaluated how these characteristics affect side-crash protection performance using vehicle mass and door clearance parameters.

The first key finding is that the injury level of chest-to-pelvis is not affected by the struck vehicle mass. In other words, every vehicle mass produced the same door intrusion velocity regardless of the struck vehicle mass. In principle, the door intrusion velocity is correlated to MDB velocity. While the velocities of the MDB and the struck vehicle were both affected by the vehicle mass, the MDB's velocity change was too slow to affect the injury level, which was already determined before the MDB velocity decreased. Secondly, the velocity of the struck vehicle was affected by its mass and this trend appeared from the beginning. The lighter vehicle moved faster. The ES2 head contacted the roof rail in the crash, and the lighter the vehicle the higher the impact speed to the head. Thus a microcar presents a more severe injury risk to the head region than a normal passenger vehicle. Thirdly, a larger gap between an occupant and the door can potentially reduce injuries, even in such a very small car.

Based on these findings, three suggestions can be made. First, acquiring as much door clearance as possible must be a priority, even in a microcar. Second, a microcar should have a door specification equivalent to that of a K-car, which gave an acceptable performance in this study as well as in JNCAP. And as a final suggestion, a head protection system should be prioritized, rather than a chest-to-pelvis protection system.

REFERENCES

[1] European New Car Assessment Programme (Euro NCAP). (2014). 2014 Safety of Quadricycles. Available from https://www.euroncap.com/en/vehicle-safety/safety-campaigns/2014-quadricycles-tests/

[2] European New Car Assessment Programme (Euro NCAP). (2016). 2016 Quadricycles' Tests. Available from https://www.euroncap.com/en/vehicle-safety/safety-campaigns/2016-quadricycles-tests/

[3] Unselt, T. Unger, J. Krause, M. & Hierlinger, T. (2015) "The Integrated Safety Concept of the Ultra-Compact Electric Vehicle." 24th ESV

[4] Fresnillo, R. M., Almarza, E. C., Zink, L., Edwards, M. J., Holtz, J., Pedersen, M. S., & Heras, R. T. (2017). "Passive Safety Strategy for Electric Lightweight Vehicles with Multimaterial Body and Centered Driver Position-Opportunities and Limitations." 25th ESV

[5] Edwards, M. J., Davies, H., Thompson, A., & Hobbs, A. (2003). "Development of test procedures and performance criteria to improve compatibility in car frontal collisions." Proceedings of the Institution of Mechanical Engineers, Part D: Journal of Automobile Engineering, 217(4), 233-245.

[6] Sadeghipour, E., Duddeck, F., & Lienkamp, M. (2014). "Crash Compatibility of Microcars: A Study on Current Test Approaches". crash. tech. congress

[7] European New Car Assessment Programme (Euro NCAP). (2020). Mobile Progressive Deformable Barrier. https://www.euroncap.com/en/vehicle-safety/the-ratings-explained/adult-occupant-protection/frontal-impact/mobile-progressive-deformable-barrier/

[8] Mizuno, K., Arai, Y., Hosokawa, N., & Hollowell, W. (2013). "The crashworthiness of minicars in frontal impact tests". 23rd ESV.

[9] Barbat, S., Li, X., & Prasad, P. (2007). "Vehicle-to-Vehicle Front-to-Side Crash Compatibility Analysis Using a CAE Based Methodology". 20th ESV (No. 07-0347).

[10] Terazawa, et al. (2022). "Occupant injury of Minicar in Side Collision with Passenger Car". JSAE Congress (Autumn), paper ID 20226201 (in Japanese)

[11] Davies, et al. (2021). "An approach for the crash safety assessment of smaller and lightweight vehicles". Transport Policy Volume 105, May 2021, Pages 12-21

[12] Sunnevång, C., Rosén, E., Boström, O., & Lechelt, U. (2010). "Thoracic injury risk as a function of crash severity–car-to-car side impact tests with WorldSID compared to real-life crashes". In Annals of Advances in Automotive Medicine/Annual Scientific Conference (Vol. 54, p. 159).

THE ANALYSIS OF MECHANISM AND COUNTERMEASURE FOR REDUCING THORACOABDOMINAL INJURY RISK CAUSED BY FAR-SIDE IMPACT

Hitoshi Ida, Yoshito Kusuhara, Masashi Aoki, Michihisa Asaoka

Toyoda Gosei Co., Ltd.

JAPAN

Ning Zhang

Toyoda Gosei North America Corp.

U.S.A.

Shiro Ohara

TGR Technical Center, LLC

U.S.A.

ABSTRACT

The European New Car Assessment Programme (Euro NCAP) added requirements in 2020 for the protection of far-side occupants. This is because in a side-impact accident, serious injuries can occur to passengers not only on the near (collision) side but also on the counter-collision (far) side.

Analysis of National Automotive Sampling System/Crashworthiness Data System (NASS-CDS) far-side accidents from 2002 to 2015 revealed that serious injuries occurred not only to the head but also to the chest and abdomen. Liver injury accounts for 48% of all abdominal injuries in occupants with seat belts, and is a type of trauma that must be noted in traffic accident lifesaving.

For head protection, the Euro NCAP test provides criteria for head movement, but no method has been established to quantify liver injury. We attempted to quantify liver injury by simulation using a human body model.

The simulation used the THUMS (Total HUman Model for Safety) human body model in which the shapes of major organs had been modeled. First, the load-displacement characteristics of the liver were modeled from the specimen level to those of the whole organ. Using the liver model, we simulated the behavior of the body in the far-side sled test performed by Pintar et al. [1], and investigated the liver injury index.

We found the maximum principal strain in the liver to range from 60% to 120% in the current model, resulting in laceration of the liver. Using the human body model, we then clarified the injury mechanism of the liver and examined how to reduce injury. In far-side accidents, it was found that the injury was caused by the upper body being catapulted toward the impact side.

A simulation was conducted to determine whether a load on the right side of the occupant to prevent this

sudden and forcible upper body could lessen liver injury.

Simulation results show that the maximum principal strain on the liver can be cut from 120% to 60% by reducing the displacement of the tenth thoracic vertebrae (T10), corresponding to the height of the liver, to within 190 mm on the impact side.

INTRODUCTION

An increasing number of vehicles are installed with side or curtain airbags to protect near-side occupants from side collision from serious injury on collision with another vehicle, a pole or the inside of the car door. A shoulder seat belt can be ineffective, as it tends to disengage from the far-side occupant, and if the occupant moves too far, he or she may be injured by collision with the inside of the car door or with other passengers. It is difficult to protect these far-side occupants with side or curtain airbags, so a different approach is needed for occupant protection than is used for near-side occupants.

For this reason, requirements to protect against far-side accidents were added to the Euro NCAP in 2020. In this test, pole side impact and side impact by AE-MDB (Advanced European Mobile Deformable Barrier) are modeled in sled tests, using WorldSID (World Side Impact Dummy) to evaluate safety in far-side accidents.

The test provides evaluation criteria for head movement, so it is also effective as an indicator of reduction of serious head injury.

In the NASS/CDS survey made by Augenstein et al. [2], 30.5% of chest and abdominal injury sources were identified as due to collision-side interiors, with 22.6% caused by seat belts. However, this data is from 1988 - 1998 and may not be relevant to vehicles manufactured in the 2000s. We therefore newly analyzed far-side accidents using NASS/CDS data from 2002 - 2015 to investigate the effect of seat belts and the patterns of chest and abdominal injuries. These injuries were then reproduced in a simulation model by Ida et al. [3]. This study extended to analyze the mechanisms of injury and to examine countermeasures.

METHODS

Field data analysis

We used the North American Vehicle Accident Database (NASS/CDS) published by NCSA, the statistical control center of NHTSA, in our accident investigation. Injury analysis was conducted on 411 occupants of the driver's seat with AIS 2 or higher injuries and the left side of the second row of ordinary passenger and commercial vehicles involved in far-side accidents over the 13-year period from 2002 to 2015.

Far-side collisions in this report refer to cases of damage to the side of a vehicle in the direction of a collision between 60 - 120 degrees. An analysis of injury tendencies was conducted for occupants taller than 140 cm to evaluate the patterns seen in typical adults. They then analyzed the differences in mortality between occupants wearing and not wearing seat belts, as well as the locations of serious injuries and patterns of abdominal organ injuries.

Development of human body model injury criteria

We developed a simulation model to evaluate liver injury, which frequently occurs in thoracoabdominal injuries caused by far-side accidents.

To analyze the mechanism of liver injury development, we developed a simulation model for liver injury assessment using the THUMS Version 6.1 human body model, which models the structure of the liver.

The approach to developing the simulation model for injury assessment was to first validate the liver material model at the tissue level, then at the whole-organ level, and finally at the whole-body level. (Figure 1)
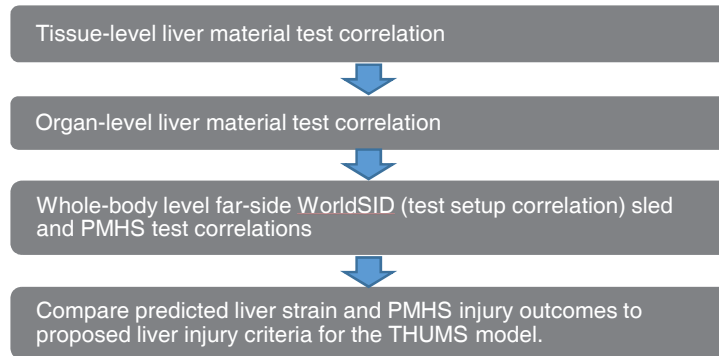

Figure 1. General strategy for human model injury criteria development

Tissue level liver material correlation

Tensile testing of the dog bone-type specimen was simulated using the same element type, size, and hourglass controls as the THUMS liver organ model. The specimen was modeled as 12 mm wide, 40 mm gauge length, and 5 mm thick (Figure 2). Tensile specimens were discretized using a one-node pressure tetrahedral element (LS-DYNA solid element type 13) with an average size of 1 mm. A simplified foam/rubber material model was used to model liver tissue with a bulk modulus of 4.59 MPa, and tensile/compressive material test curves were used to define material behavior. A linear total strain hourglass control (LS-DYNA Type 7) was selected for the solid liver material. A 20 mm stroke was applied to the tensile specimen model over 1 second, producing an approximately 50% engineering strain in the displacement-controlled test mode. The green strain along the tensile direction of the element near the center of the specimen was used as the strain output, the Cauchy stress tensor from the same element was used as the stress output, and the strain-stress curve was then plotted. Strain-stress curves from model simulations were validated against test data [4].

Next, a cylindrical specimen was used to simulate a uniaxial compression material test. Using a symmetric boundary condition, only a quarter of the cylinder was modeled. The specimen was 25.4 mm in diameter and 10 mm in height. A rigid disk was used to apply a 5 mm/s to the specimen, resulting an engineering strain of approximately 50% being applied to the specimen. The friction between the jig and the liver specimen was assumed to be zero. Strain was calculated as engineering strain, and stress was calculated as the contact force in the direction of compression divided by the cross-sectional area. The compressive strain-stress curve from the model simulation was validated against the test data [4].

Finally, to achieve better correlation, the tensile and compressive material curves defining the material properties of the liver were scaled from the current material properties of the THUMS model. The scaled liver material curves were later used for further correlation at the organ and whole-body levels.
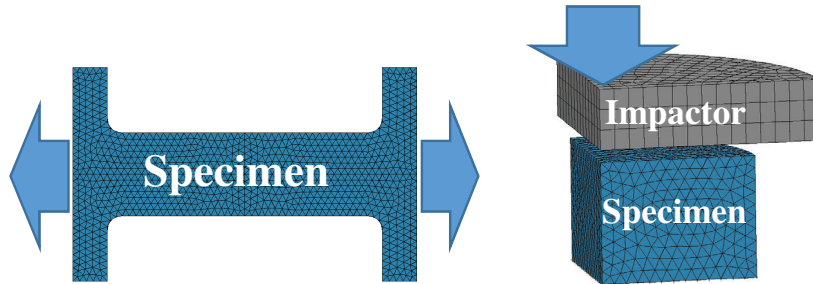

Figure 2. Model shapes of dog bone tensile specimen and cylindrical compressive specimen

Organ-level liver model correlation

The physical properties of the human model were verified using tensile and compression tests of the liver obtained by Kemper et al. from PMHSs (Post Mortem Human Subjects) [4]. A cylindrical impactor with a cross-sectional area of 11.6 cm^2 was impinged on the liver at a constant speed of 200 mm/s (Figure 3). The total stroke of the impactor was 15 mm.
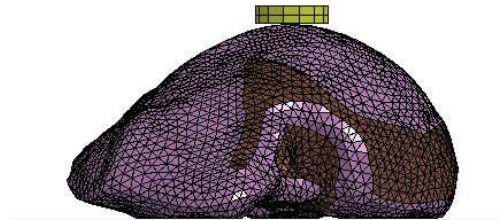

Figure 3. Organ-level liver impactor test setup

Whole-body level correlation

First, the 13 far-side PMHS sled tests performed by Pintar et al. [1] were selected for whole-body level correlation. Test videos and test results were downloaded from NHTSA's Biomechanics Test Database [5].

Second, test fixtures, constraints, and sensor output models were first validated using a test data set from 18 pairs of WorldSID dummies with the same collision severity and constraints as in the PMHS test (Table 1, Figure 4). The WorldSID dummy model from Livermore Software Technology was used. Dummy kinematics, load cell output from the impact wall, and dummy sensor output were verified against the test results. We selected CORA software [6] to quantify the correlation results. CORA's Weight calculated the correlation using a Cross correlation function of 0.667 and Size and Phase shift of 0.167.

Table 1.

Cases used for whole body level correlation. (18 cases selected from the NHTSA biomechanics database to correlate the far-side impact fixture setup; 9 (gray rows) of 18 had a matched pair test with male PMHS.)

[I/B: Inboard, O/B: Outboard, PT: Pretensioner]

| NHTSA ID	Test ID	Impactor angle	Velocity (m/s)	Shoulder plate	Thorax plate	Seat belt configuration
10158	FSDS107	90	3.25	Yes	No	D-ring at I/B, Low position
10159	FSDS108	90	8.87	Yes	No	D-ring at I/B, Low position
10160	FSDS109	90	8.84	Yes	No	D-ring at O/B, PT
10161	FSDS110	90	3.13	No	Yes	D-ring at I/B, Low position
10162	FSDS113	90	8.69	No	Yes	D-ring at I/B, Low position
10163	FSDS114	90	8.64	No	Yes	D-ring at O/B, PT
10164	FSDS115	90	3.21	No	No	D-ring at I/B, Low position
10165	FSDS118	90	8.92	No	No	D-ring at I/B, Low position
10166	FSDS119	90	8.85	No	No	D-ring at O/B, PT
10167	FSDS121	90	8.57	No	No	D-ring at I/B, Low position, PT
10168	FSDS122	60	3.12	No	Yes	D-ring at I/B, Low position, PT
10169	FSDS123	60	8.20	No	Yes	D-ring at I/B, Low position, PT
10170	FSDS124	60	3.11	No	No	D-ring at I/B, Low position, PT
10171	FSDS126	60	8.47	No	No	D-ring at I/B, High position
10172	FSDS127	60	8.42	No	No	D-ring at I/B, Low position, PT
10174	FSDS130	60	8.13	No	No	D-ring at O/B, PT
10175	FSDS132	90	3.27	No	No	D-ring at O/B, D ring forward
10176	FSDS133	90	8.02	No	No	D-ring at O/B, D ring forward
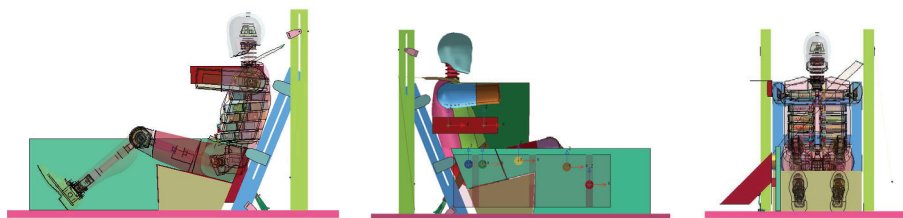
Figure 4. Whole body level far-side sled test setup with WorldSID

Third, the WorldSID dummy model was replaced with a THUMS V6.1 human model, and the impact simulation was repeated to output the kinematics of the human body, deformation of the chest band, rib fractures near the liver, load cell output of the impact wall, and accelerometer output of the first thoracic vertebra (T1), T4,

T12, and the sacrum. CORA scores from these channels were reported for assessment of correlation levels. Thirteen test cases with male subjects close to the 50 percentile physique were reported.

As another set of PHMS tests, simulations were also performed using the 75-degree angle Euro NCAP pulses used in the tests by Petit et al. [7]. The PMHS test by Petit et al., using Euro NCAP pulses, uses the same fixture as the PMHS test by Pintar et al., but the height of the console and the gap between the console and the occupant are different from the test by Pintar et al.

Development of liver injury threshold

After the whole-body correlation had been obtained, the distribution of maximum principal strain (MPS) in the liver was output. Because liver lacerations occur most frequently on the anterior and superior sides of the liver surface [8], elements in these areas were grouped together to obtain time-history curves of strain. Finally, peak strain values and locations were determined. Strain levels were compared to the injury results described in the PMHS autopsy report, and strain values for lacerated liver injuries were derived based on this series of PMHS test data.

RESULTS

Field data analysis

We first analyzed the relationship between using seat belts and injury (Table 2). It was found that occupants who used seat belts had a mortality rate of 18%, while that for occupants not using seat belts was 26%. The average barrier conversion speed of occupants who died using seat belts was 58.66 km/h, while the average barrier conversion speed of occupants who died without seat belts was 42.34 km/h. The results suggest the benefits of seat belt use even in far-side accidents.

Table 2.

Far-side accident occupant data with AIS 2 or higher (survival/death, with or without seat belts)

	With seat belts Survival	With seat belts Death	Without seat belts Survival	Without seat belts Death
Number of Occupants	224	50	101	35
Ave. Age	41.50	43.46	32.88	44.20
Ave. Height	170.04 cm	170.60 cm	172.16 cm	176.06 cm
Ave. Weight	76.15 kg	85.12 kg	84.91 kg	86.37 kg
BMI	26.34	29.25	28.65	27.87
Barrier Equivalent Speed	36.34 km/h	58.66 km/h	32.15 km/h	42.34 km/h
MAIS	2.72	4.52	2.99	4.29
ISS	12.26	40.14	15.82	37.03
Number of injuries	6.53	14.28	8.67	15.20
	Death rate : 18%		**Death rate : 26%**	

However, because 18% of occupants with seat belts died, we next analyzed the location of AIS4 or higher injuries in occupants with seat belts (Figure 5).

The most common injured body site was to the head, which suggests that the shoulder, whether restrained by a seat belt or kept at the waist, can slip through the seat belt and collide with an interior component on the collision side.

On the other hand, serious injuries to the abdomen, which is relatively close to the waist while being restrained by a seat belt, accounted for 10% of all serious injuries.
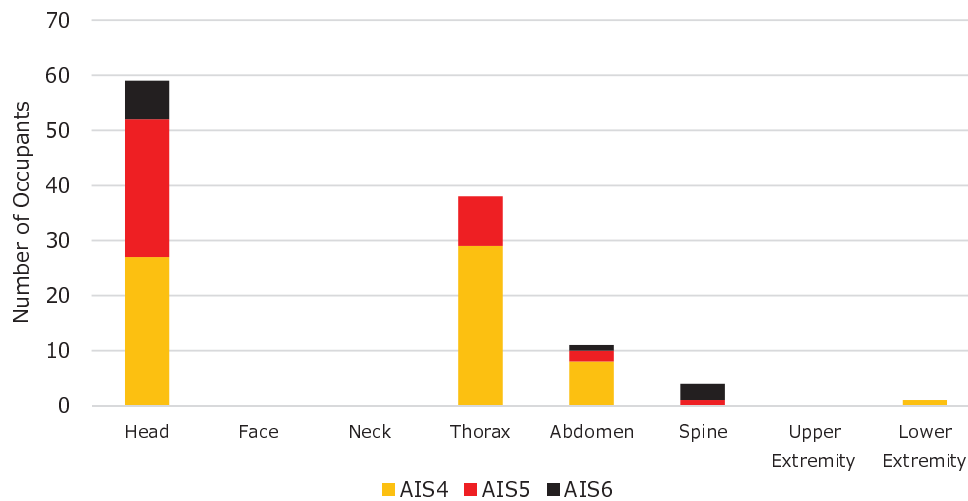

Figure 5. Number of occupants who sustained injuries in far-side accidents of AIS4 or higher with seat belts

Ida 7

Further analysis of the injured organs in the abdominal injuries of occupants with seat belts found that damage to the liver accounted for almost half of the injuries (Figure 6).

Of a total of 53 patients with blunt liver trauma who underwent surgery at the First Affiliated Hospital of the Wenzhou Medical College between 1999 and 2009, 67.9% are reported to have sustained injuries in the right lobe. Major lacerations may be associated with rupture of the right hepatic vein [9].

The superior surface of the liver is attached to the diaphragm by the falciform ligament, suggesting that blunt force to the right side of the right lobe can cause lacerations.
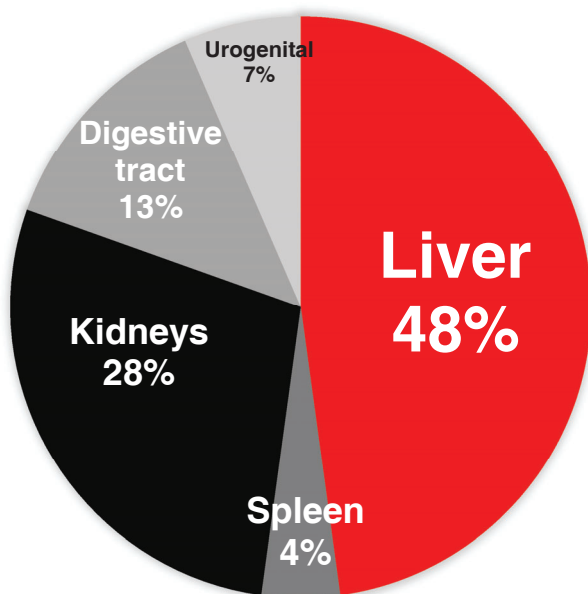

Figure 6. Abdominal organ injury distribution with seat belts (AIS2 or higher)

Development of Human Body Model Injury Criteria

Tissue-level liver material correlation

A simulation model was developed to reproduce the incidence of liver lacerations.

At the tissue level, early THUMS liver material models of THUMS V6.1 were softer than tests showed. Simulations of the material response of the dog bone-type tensile specimens showed the tensile stiffness of the THUMS liver material model to be within the test range but very close to its lower limit. After scaling up the tensile liver material curves by a factor of 1.5, the tensile test results were consistent with the average tensile test data (Figure 7). For compressed material test simulations, the model results were within the test corridor up to 35% of the engineering strain, with the curve close to the lower limit of the corridor. When the load exceeded 35% of the engineering strain, the model results exited the test range and dropped significantly. Based on the

initial results, the stiffness of the liver compression material was scaled up by a factor of four from more than 20% compression strain. After enlarging the compressed liver material curve, the simulated results curve of the compression test remained within the test results corridor (Figure 8). The altered liver material properties were applied to the next steps in organ and whole-body research.
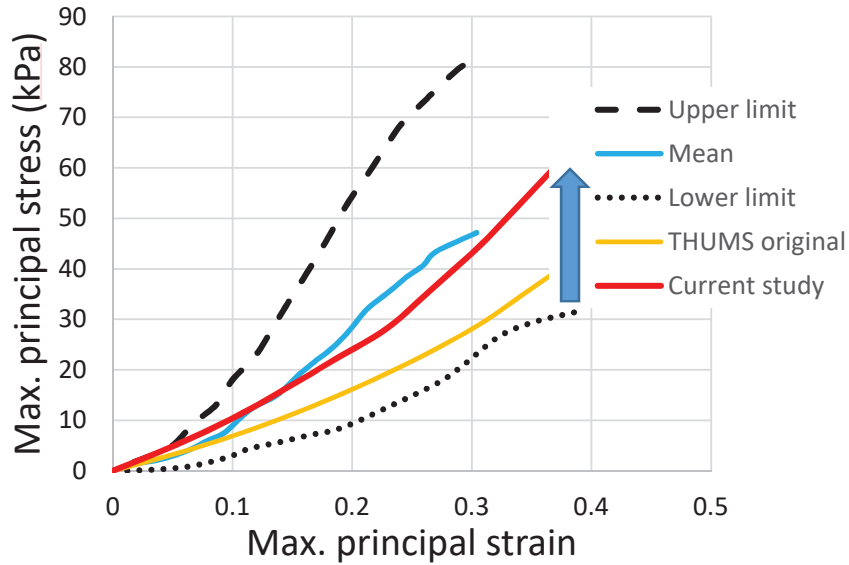

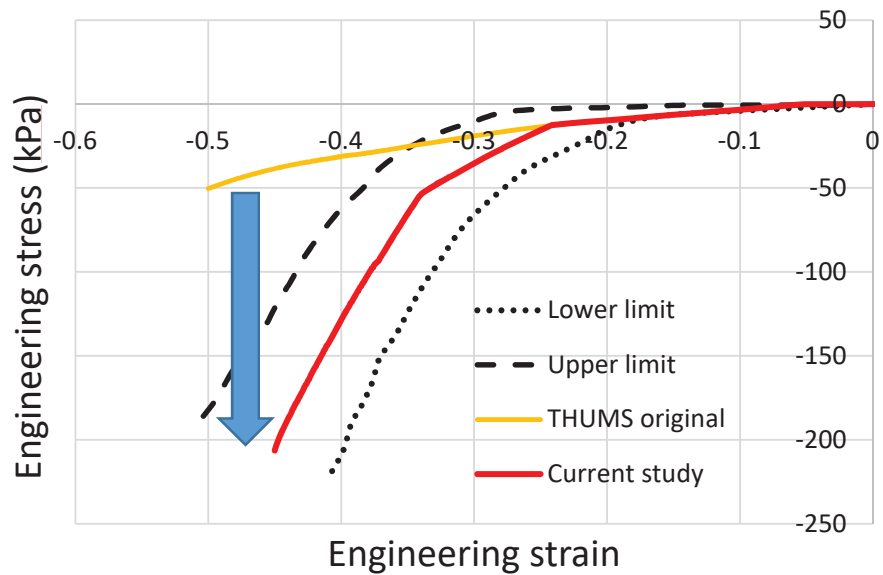*Figure 7. Correlation of liver specimen with tensile tests*

Figure 8. Correlation of liver specimen with compressive test

Organ-level liver model correlation

Simulations were performed using cylindrical impactors at the organ level using physical properties correlated

at the tissue level. The results confirmed that the compression characteristics of the PMHS and those of the simulation model were consistent. (Figure 9)
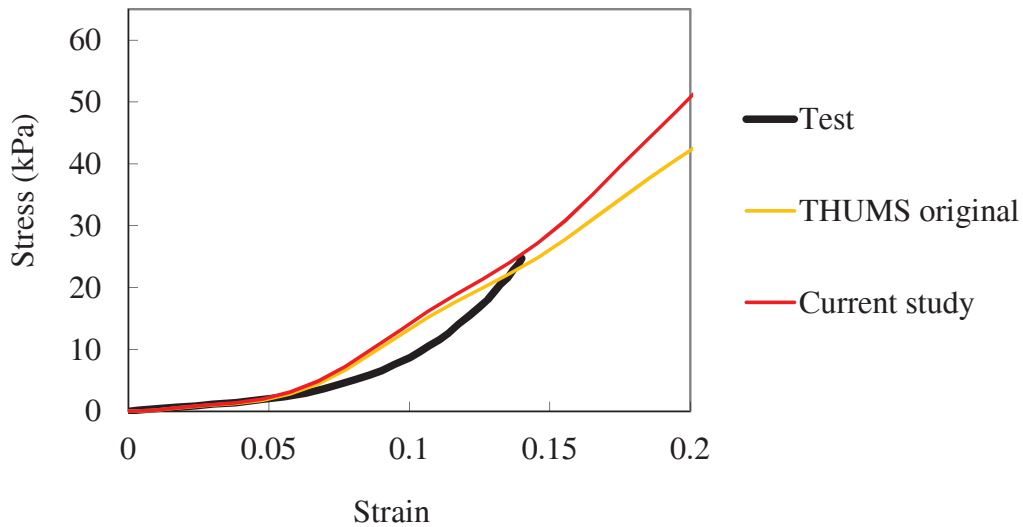

Figure 9. Correlation of liver organ level tests

Whole-body-level correlation

  A good kinematic correlation was obtained between the simulation and the test for the WorldSID dummy motion in the sled test by comparing video material (Figure 10, Figure 11). The average CORA score for a total of 18 far-side impact tests was 0.62. The correlation of head acceleration was good. Spinal acceleration correlated well (average CORA score for T1 on Y axis was 0.69, T12 on Y axis was 0.56). Pelvic acceleration correlated well (average CORA score was 0.70 on the y-axis). The correlation level of the load wall force varied according to the location of the load cell (average CORA score for pelvic wall load cells was 0.84, average CORA score for shoulder wall load cells was 0.59).
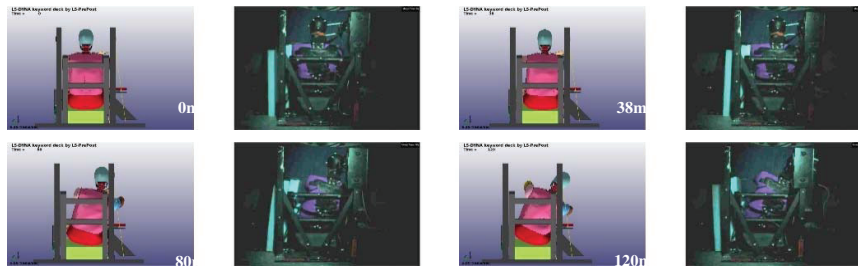

Figure 10. Kinematics comparison between simulation and test videos for WorldSID Case 101
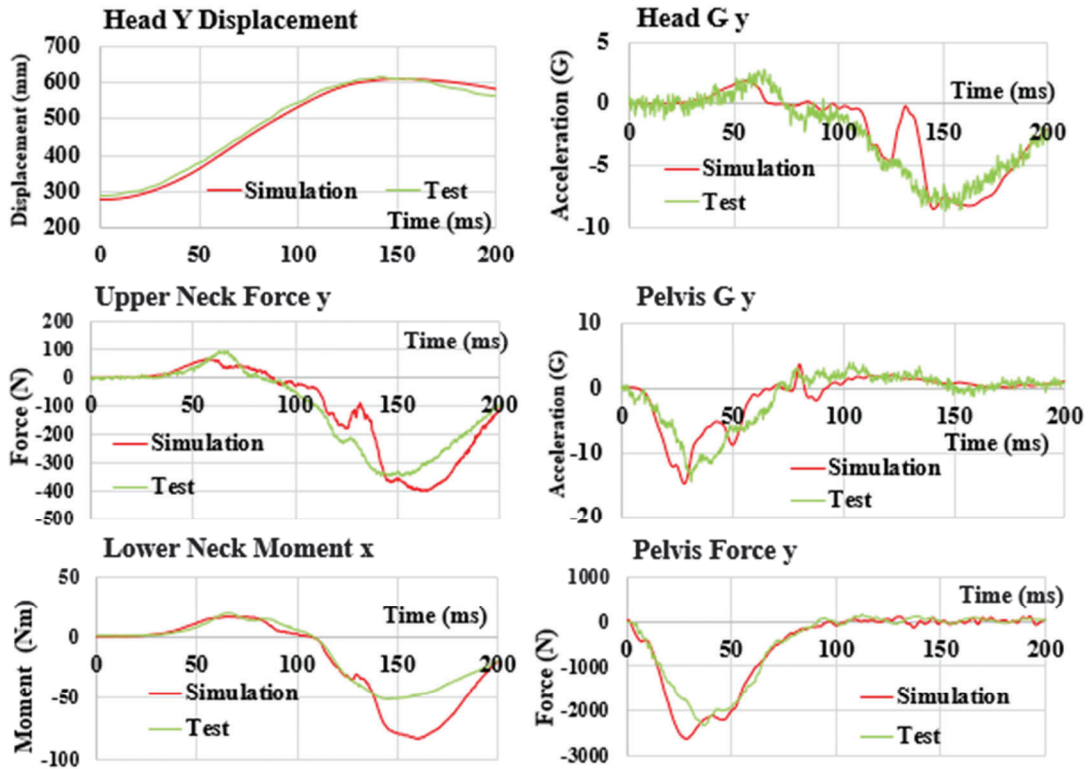
Figure 11. Curve comparison between simulation and test videos for WorldSID Case 10164

The THUMS model of sled simulation yielded good kinematic correlations (The average CORA score for head displacement was 0.92 on the y-axis and 0.65 on the z-axis). Belt force correlation was good (average shoulder belt force CORA score was 0.73). The force correlation of the load wall varied according to the location of the load cell (load cells in the pelvic wall had an average CORA score of 0.82 and load cells in the shoulder wall had an average CORA score of 0.59).

The correlation between rib and spine acceleration was acceptable (mean CORA score was 0.51 for T12 and 0.65 for the sacrum).

Because the rib and spine transducers are noisy, these accelerometers have lower CORA scores (Figure 12). Significant deformation at the lower rib cage level, where it interacts with the console and seat belt, was identified in the simulation (Figure 13), and the deformation of the section in the simulation matched the sled test chest band data corresponding to the height of this console (Figure 14).
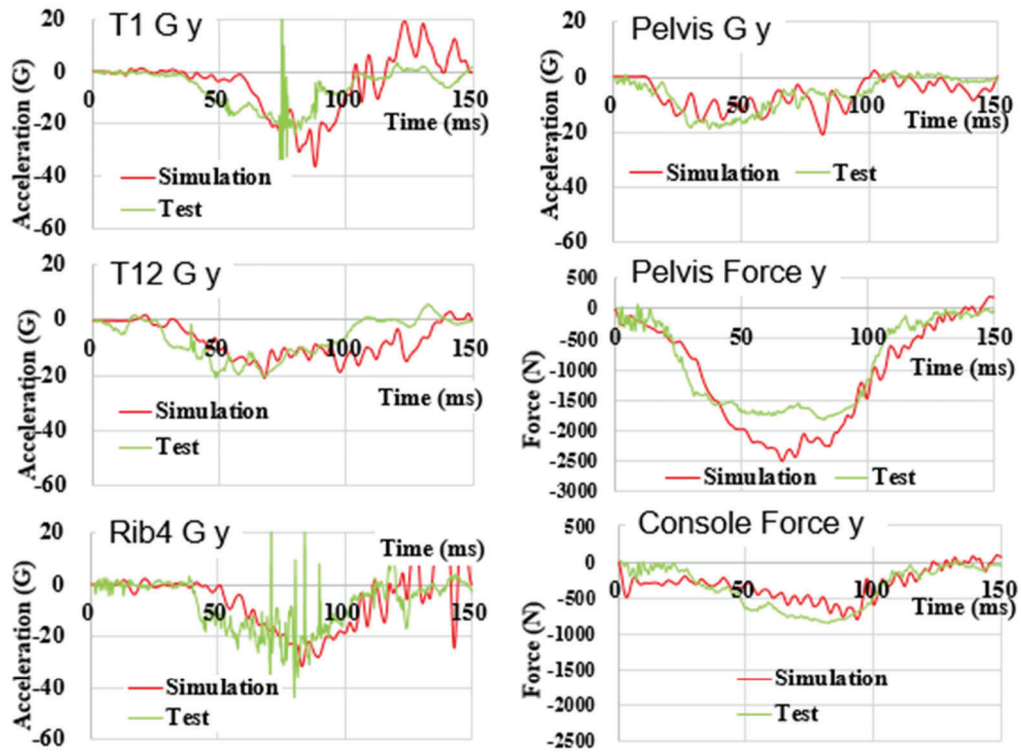
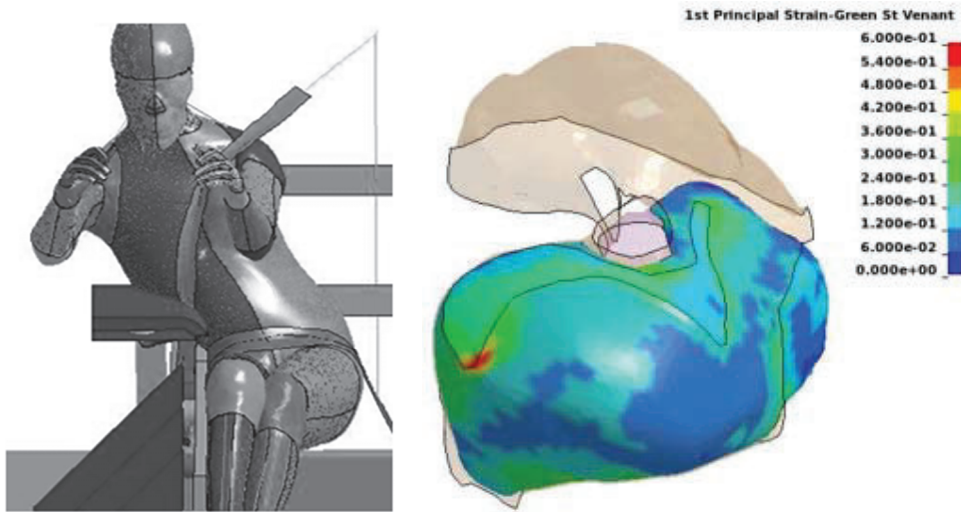*Figure 12. Curve comparison between simulation and test for PMHS Case 10044*

Figure 13. Global kinematics (Left), local liver strain of Case 10045 (Right)
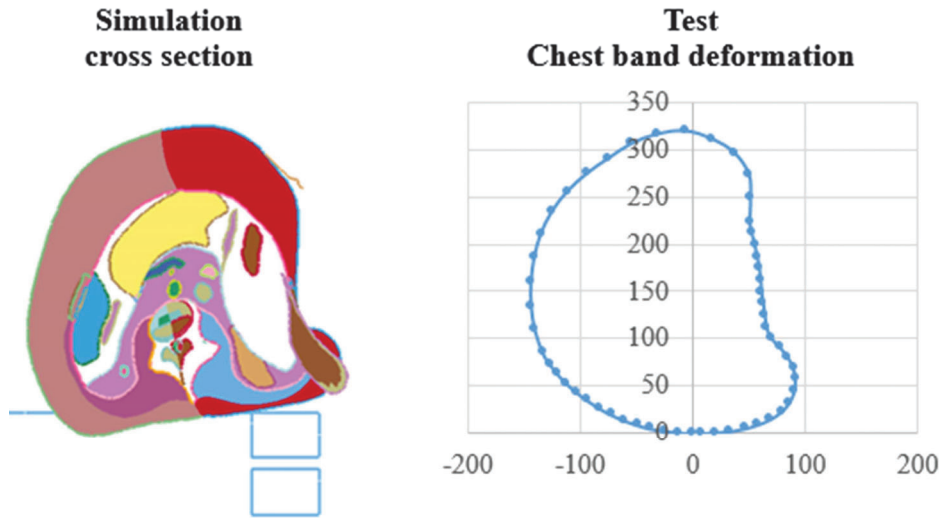
Figure 14. Simulation cross section at console height and chest band deformation from test (Case 10045)

Development of Liver Injury Threshold

   Comparison of the maximum principal strain (MPS) of the liver in THUMS mimicking the behavior between studies in which liver lacerations occurred and those in which liver lacerations did not occur confirmed an MPS of 59% in the PMHS study of Pintar et al. [1] and an MPS of 123% in the PMHS study of Petit et al. [7] in which liver lacerations occurred. (Table 3) We assumed an MPS of 60% as the threshold for the risk of liver laceration because the MPS was 28% in cases in which no liver laceration occurred.

   In addition, the lateral displacement of tenth thoracic vertebra (T10), which is located at the level of the liver, increased to 249 mm in cases with liver lacerations compared to 188 mm in cases without liver lacerations.

   These results suggest that the increased movement of the occupant toward the impact side increases the maximum principal strain in the liver.

Table 3.

Comparison of liver damage between PMHS test and THUMS simulation

PMHS test results			THUMS	THUMS lateral displacement (mm)			
Console height	Test No.	Liver laceration	Liver MPS	Head Y	T1 Y	T10 Y	Pelvis Y
Baseline	10049	No	28%	413	249	188	47
Baseline	10045	Yes	59%	651	451	295	86
Baseline + 50 mm	740	Yes	123%	575	384	249	116

DISCUSSION

Liver injury mechanism

The location of maximum principal strain on the liver surface was the upper surface of the right lobe of the liver where the liver was attached to the diaphragm (Figure15). The reason for the concentration of maximum principal strain here is thought to be that the diaphragm and part of the rib cage moved toward the impact side and pulled the upper surface of the right lobe of the liver that is attached to the diaphragm. The mechanism of this liver injury was also consistent with reports based on clinical data by Jin et al. [9].
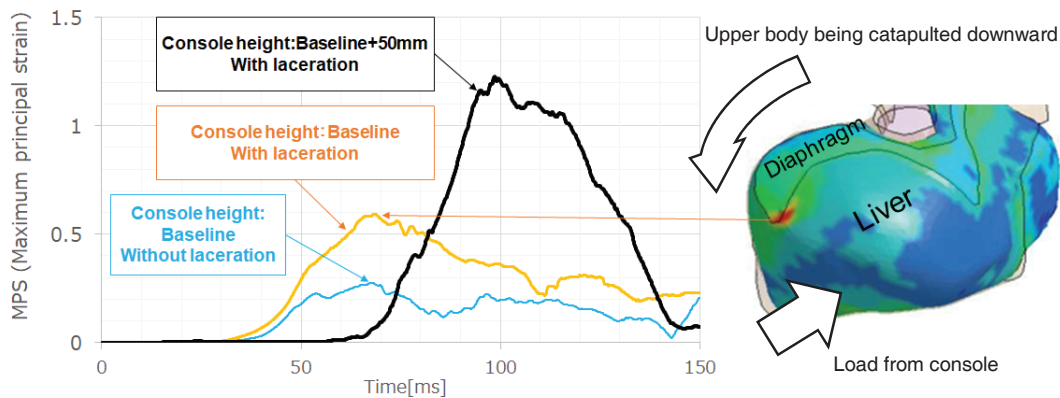

Figure 15. Liver MPS (With/Without laceration)

To confirm the effect of console height on the risk of liver laceration, simulations were performed with the console height increased by 50 mm from baseline. The result showed that when the console height increased by 50 mm, the T10 displacement decreased by 46 mm, but the liver MPS increased more than twice (Table 3). This may be due to the high height of the console, and the lower part of the liver, which receives a blunt impact from the console, could not follow the lateral movement of the ribcage, and the upper surface of the right lobe of the liver attached to the diaphragm may be pulled laterally. (Figure 15, Figure 16).
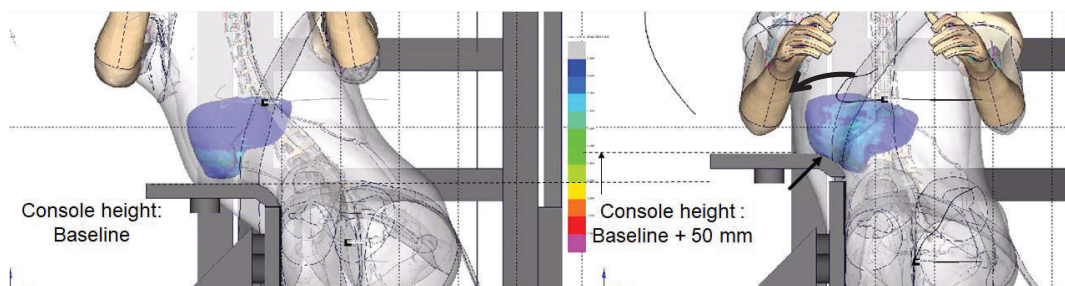

Figure 16. Console height comparison between two simulation cases

In addition, when the console height was increased by 50 mm from baseline, the MPS of the upper surface of

Ida 14

the liver attached to the diaphragm was twice that of the lower surface of the liver that received to blunt force from the console (Figure 17).

These results suggest that it is effective for the protection of abdominal organs to minimize not only the direct external force exerted by the console but also the forced movement of the upper body.
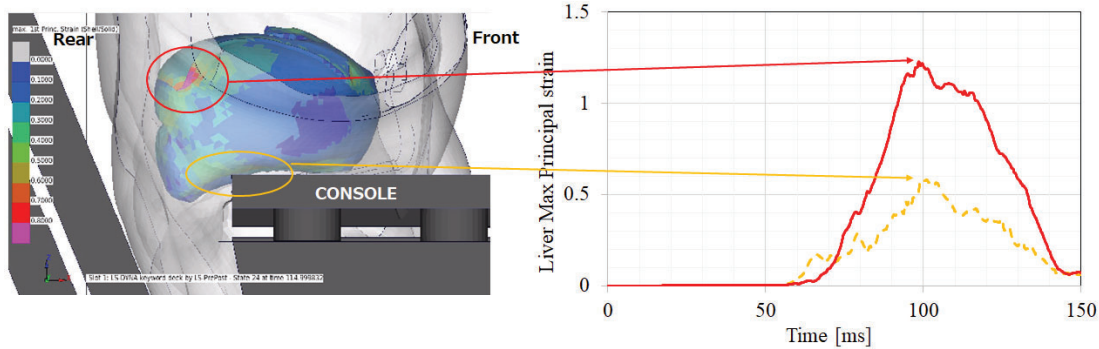

Figure 17. Liver MPS (Upper area/Lower area), Console height: baseline + 50 mm Case

Countermeasures to liver injuries

To confirm the effect of minimizing the forced movement of the upper body, a simulation was performed by applying an external force virtually from the right side of the occupant under the condition of the MPS of the liver being 123% that increased console height 50 mm from baseline (Figure 18).

For the external force from the right, rigid plates covering the occupant's head, shoulders, chest and abdomen, and lower back, which can move only laterally, were placed on the right side. Each rigid plate was given a lateral Force-Displacement characteristic to adjust the movement of the upper body.

As a result of adjusting the movement of T10 to be smaller than in Test No. 10049 without liver laceration as seen in Table 3, the MPS of the liver could be reduced to 55%. (Table 4, Figure 18, Figure 19)

From these results, it was found that to reduce liver injury, it is effective to apply an external force such that the MPS of the liver does not exceed 60% and thus preventing the forced movement of the upper body.

Table 4.

Results of countermeasure

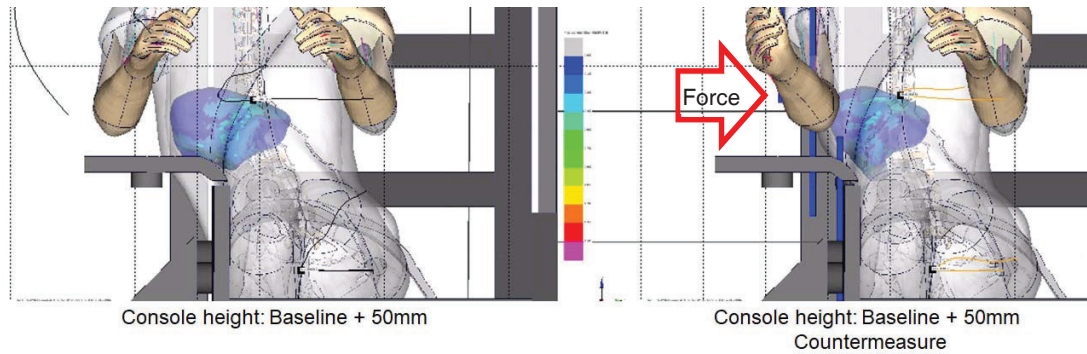| PMHS test results			THUMS	THUMS lateral displacement (mm)			
Console height	Test No.	Liver laceration	Liver MPS	Head Y	T1 Y	T10 Y	Pelvis Y
Baseline + 50 mm	740	Yes	123%	575	384	249	116
Countermeasure (Added lateral force to control body)			55%	317	221	172	114

Figure 18. Liver MPS, Console height: Baseline + 50 mm (Left) and Countermeasure (Right)
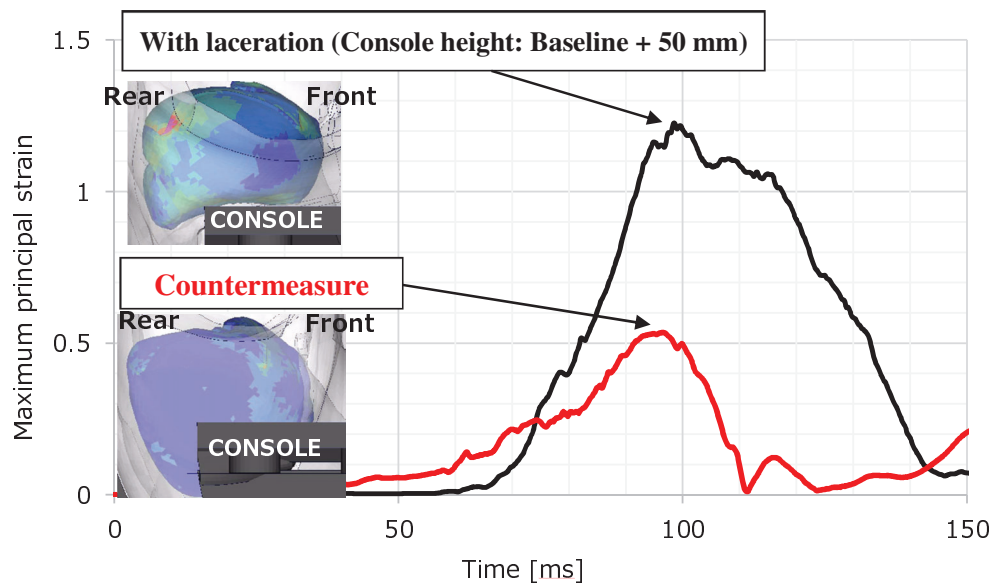
Figure 19. Liver MPS (With laceration / Countermeasure)

CONCLUSIONS

・Analysis of far-side accidents using NASS/CDS accident investigation results showed that 10% of serious injuries to seat belt occupants also included injuries to the abdomen.

・Liver injury accounts for the highest proportion (48%) of abdominal injuries in occupants with seat belts

・To analyze the mechanism of the development of liver injury, a human model THUMS liver was subjected to a donation test.

The behavior of the PMHS sled test was reproduced by checking the material level and the organ alone.

・In the PMHS study, the maximum principal strain (MPS) of the liver of THUMS under conditions where liver laceration occurred exceeded 60%, which was judged to be the threshold for the risk of liver laceration.

・We found that the MPS of the liver was also affected by the height of the console, and that the risk of laceration of the top surface of the liver was likely to increase when the lower end of the liver was loaded by the

console.

・To reduce the risk of liver laceration, it is effective to prevent the forcible movement of the entire upper body.

ACKNOWLEDGEMENTS

REFERENCES

[1] Pintar, F., Yoganandan, N., & Stemper, B. (2007). Comparison of PMHS, WorldSID, and THOR-NT Responses in Simulated Far Side Impact. Stapp Car Crash Journal, Vol. 51, 313-360

[2] Augenstein, J., Perdeck, E., Martin, P., Bowen, J., Stratton, J., Horton, T., … Steps, J. (2000). Injuries to restrained occupants in far-side crashes. Association for the Advancement of Automotive Medicine. Vol. 44, 57-66

[3] Ida, H., Aoki, M., Asaoka, M., Zhang, N., Ohara, S., Diederich, A., Hoffmann, J. (2022, November). The development of a thoracoabdominal organ injury index for far-side car occupants exposed to side impacts. Airbag 2022 (15th International Symposium and Exhibition on Sophisticated Car Safety Systems), Mannheim, Germany

[4] Kemper, A., Santago, A., Sparks, J., Thor, C., Gabler, HC., Stitzel, J, & Duma, S. (2011, June). Multi-scale biomechanical characterization of human liver and spleen. 22nd ESV Conference; Washington D.C., USA.

[5] NHTSA, Research Testing Database. (2021). Retrieved from https://www.nhtsa.gov/research-data/databases-and-software

[6] Partnership for Dummy Technology and Biomechanics. (2021). CORA (3.6.1). Retrieved from https://www.pdb-org.com/en/information/18-cora-download.html

[7] Petit, P., Trosseille, X., Uriot, J., Poulard, D., Potier, P., Baudrit, P., Compigne, S., Kunisada, M., & Tsurui, K. (2019, November). Far Side Impact Injury Threshold Recommendations Based on 6 Paired WorldSID /Post Mortem Human Subjects Tests. Stapp Car Crash Journal, Vol. 63, 127-146

[8] Slotta, J.E., Justinger, C., Kollmar, O., Kollmar, C., Schäfer, T., & Schilling, M.K. (2014). Liver injury following blunt abdominal trauma: a new mechanism-driven classification. Surg Today. 44, 241–246.

[9] Jin, W., Deng, L., LV, H., Zhang, Q., & Zhu, J. (2013). Mechanisms of blunt liver trauma patterns: An analysis of 53 cases. Experimental and Therapeutic Medicine. 5, 395–398.

Crash Simulations of FMVSS No. 214 Safety Performance

Rudolf Reichert
Steve Kan, Ph.D.
George Mason University

United States

Paper Number 23-0036

ABSTRACT

Objective: Federal Motor Vehicle Safety Standard (FMVSS) No. 214 requires doors in applicable vehicles to meet minimum force requirements when subjected to a static load in addition to the occupant protection requirements for the dynamic moving deformable barrier (MDB) and vehicle-to-pole (VTP) side impact tests. This paper explores how non-compliance of a single test condition affects the compliance and performance of the other two tests. Additionally, potential dynamic measurements that could be considered as a surrogate for the static test procedure, are discussed.

Methods: Validated FE models of a 2015 Toyota Camry sedan, and a 2020 Nissan Rogue SUV were used to understand the mutual effect of FMVSS-214 non-compliance. Modifications to the baseline model(s) were developed that demonstrated non-compliance to the static test. Simulations were then performed to evaluate how this affected vehicle and occupant responses in the dynamic tests. The effect of MDB and VTP non-compliance on the respective other two configurations were studied in the same manner. Measurements from the dynamic tests, such as deformation metrics, accelerometer, and load cell force data, were analyzed to determine if they can indicate performance in the static door crush test.

Results: Baseline simulation results showed FMVSS-214 compliance of the sedan vehicle for all three impact conditions. A first modified FE model was developed by reducing the door beam strength, resulting in non-compliance in the static test. Using this model, higher vehicle and occupant metrics were observed in the dynamic tests, while still clearly complying with FMVSS-214 requirements. A second and third modified FE model was developed by mainly reducing the strength of B-Pillar and sill components, resulting in non-compliance to the dynamic MDB and VTP conditions, respectively. Reduced door strength was observed using these models in the static test, while complying with FMVSS-214 static requirements. Limited correlation between measurements from the dynamic tests and door strength in the static test was observed

Discussion and Limitations: The three FMVSS-214 configurations engaged different main load paths. Door beam strength was most relevant for the static test but did not significantly affect performance in the dynamic tests. B-Pillar and sill strength were most relevant for the MDB and VTP tests, respectively, but did not notably affect performance in the static test. The static door crush test impactor does neither overlap with the B-Pillar nor the sill. Similar results with respect to the static door crush test were observed using a validated FE model of a 2020 Nissan Rogue SUV. Since two specific vehicles representing the sedan and SUV categories were used, conclusions can not necessarily be generalized for other vehicles.

Conclusions: The research is relevant to understanding side impact performance measures. Structural vehicle modifications that resulted in non-compliance for the FMVSS-214 static test did not cause non-compliance in the dynamic MDB and VTP tests, and vice versa. There are significant limitations of using dynamic performance measurements from the dynamic tests as a surrogate for the static test due to the different main load paths engaged by the respective FMVSS-214 configurations.

INTRODUCTION

FMVSS No. 214 requires doors in applicable vehicles to meet minimum force requirements when the door is statically loaded (crushed) by a rigid steel cylinder or semi-cylinder. Additionally, FMVSS No. 214 requires occupant protection during dynamic MDB and VTP tests. This project explores options for developing performance criteria so that the FMVSS No. 214 dynamic MDB and/or VTP tests could be used as replacements for the static door crush resistance requirements of FMVSS No. 214, thus allowing the static requirements to be eliminated without reducing safety. Neither of the existing dynamic FMVSS No. 214 test procedures measure door crush resistance force.

The scope of this project consisted of developing, validating, and using detailed finite element (FE) models for use in side impact test procedures for two vehicles with different side impact characteristics. The FE models were to be used to compare intrusions, applied forces, and occupant injury metrics among baseline and modified vehicle simulations. The vehicle modifications were to be developed to meet or only partially meet FMVSS No. 214 static and dynamic test requirements. The results were then to be evaluated to consider the feasibility of using the dynamic performance measurements as a surrogate for the static test.

OBJECTIVE

The objective of this research was to develop and use detailed FE vehicle models to simulate FMVSS No. 214 static door crush, dynamic MDB, and VTP test conditions. The baseline FE simulations were to be validated against test data where available. Testing was to be conducted or contracted to provide additional validation data where needed. In addition to the baseline validation, three model variations were to be developed to demonstrate non-compliance with a single test condition. Simulations for each model variation were to be performed in each of the three test conditions. The simulation results for the modified vehicle models had to be analyzed to consider how non-compliance with a single test condition affects the compliance and test performance of the other two test conditions. Additionally, the feasibility of dynamic measurements that could be considered as a surrogate for the static test procedure had to be evaluated, if applicable.

Specifically, the objectives were the following.
- Devise at least two different vehicles for side crash simulation development and testing. The vehicle selection should consider the diversity of vehicle geometry, design, and crash kinematics.
- Where required purchase vehicles, measure and conduct testing to support the development and validation of simulation models.
- FE models shall be developed for the selected vehicles in each of the three test conditions. Each model shall be validated against test data. Objective rating methods shall be used to evaluate the correlation between test and simulation results. For the dynamic tests, it is sufficient to validate against the vehicle intrusion and intrusion velocity measurements rather than the resulting occupant injury criteria.
- Develop, simulate, and evaluate vehicle modifications. The first modifications will demonstrate minimal non-compliance to the static FMVSS No. 214 test. Simulations will be performed to evaluate how non-compliance affects the vehicle response in the MDB and VTP tests.
- Similarly, develop modifications that produce minimal non-compliance with the MDB and VTP dynamic FMVSS No. 214 configurations. Evaluate how this would affect the vehicle response in the static and VTP/MDB test, respectively.
- Evaluate the simulation results for compliant and non-compliant vehicle models and evaluate the feasibility of using measurements from the dynamic tests to predict compliance with the static 214 test requirements.

METHODS

Vehicle Selection
FMVSS No 214 static door crush and dynamic pole requirements apply to vehicles with a Gross Vehicle Weight Rating (GVWR) up to 10,000 pounds, while the FMVSS No. 214-MDB compliance is required for passenger cars with GVWRs up to 10,000 pounds but to multipurpose passenger vehicles, trucks, and buses with a GVWR up to 6,000 pounds. Vehicles with a GVWR above 6,000 pounds were not considered for this research. The identification of two different vehicles was important to assess variations in vehicle designs. The criteria that were used to identify the most suitable vehicle types for this research are outlined below.

The first vehicle selection criteria included the evaluation of design concepts and side crash characteristics. Different vehicle geometries and classes show significantly different behavior in side impact in general and in FMVSS No. 214 configurations in particular. Three vehicle types/classes, which represent the most important differences in crash kinematics due to vehicle and sill height, vehicle mass, and door length were considered.

Four-door sedan
This vehicle class was important for this research, representing a large percentage of vehicles on the road. Typically, the MDB partially overrides and does not engage the sill of the vehicle and loads are transferred into the door and B-pillar.

Pickup or SUV
This vehicle class can be less critical with respect to occupant protection in the MDB configuration. Due to the different vehicle dimensions and higher occupant seating position, the MDB typically engages with the sill area of the vehicle. Loads are transferred into the sill/floor, the door, and the B-pillar. In contrast, VTP configurations can be more critical compared to sedans, due to the higher vehicle mass, which can result in higher forces and intrusions. Two different pole locations can be tested according to FMVSS No. 214: the first one is aligned with the head of the 5th percentile occupant in a more forward seating position, the second one is positioned to hit the head of a 50th percentile occupant in a longitudinal mid position. The more forward position was considered more critical with respect to vehicle intrusion criteria.

Two-door sedan coupe or convertibles
While the overall sales numbers are smaller than for the previously described vehicle types, the two-door coupe type vehicles often have longer doors and can present challenges in side impact protection. Specific structural countermeasures and restraint system solutions are needed to overcome these challenges.

Sales numbers and rating results
The second vehicle selection criteria included sales numbers and rating results. An analysis was performed on how well a candidate vehicle represents cars in the US market and how well the vehicle performed in side impact consumer information crash tests. A vehicle with higher sales numbers was considered a better candidate vehicle for this study. All applicable vehicles on U.S. roads fulfill the FMVSS No. 214 requirements. Differences exist in side impact NCAP (SINCAP) and Insurance Institute for Highway Safety (IIHS) rating tests. Vehicles with higher ratings were considered to have better structural design and are therefore more likely to be used in future vehicle structures and hence were judged better candidates for inclusion in this research.

Availability of FE models
Several publicly accessible FE vehicle models are available from NHTSA (www.nhtsa.gov/crash-simulation-vehicle-models). The models were developed using a reverse engineering process. FE model examples include the 2015 Toyota Camry, the 2014 Honda Accord, and the 2018 Dodge Ram. A candidate vehicle model for this study was the detailed Toyota Camry FE model. A vehicle would be a good candidate for this study if a baseline model is already available and has been used and validated in previous studies. An available FE model of the 2018 Ram was considered, but dismissed because of a GVWR above 6,000 lbs. Instead, a FE model of the popular crossover SUV vehicle class, a 2020 Nissan Roque was developed, using a reverse engineering process in course of this research.

Selected sedan vehicle: 2015 Toyota Camry
Based on the criteria defined above, the 2015 Toyota Camry was selected for this research, representing the 4-door sedan vehicle class with a low sill as well as a door and B-pillar design characterizing many sedan vehicles. It has

been one of the top selling vehicles in the United States in recent years. The Toyota Camry received a 5-Star SINCAP and a "GOOD" IIHS crash rating for the 2015 as well as for the 2020 model year. FMVSS No. 214-pole and SINCAP MDB test data exists, and a detailed FE model of a Toyota Camry was previously developed using a reverse engineering process. [1,2]

Selected SUV vehicle: 2020 Nissan Rogue
A 2020 Nissan Rogue was selected as a second vehicle to conduct the FMVSS No. 214 simulation study to understand the effect of mutual non-compliance. It represents the crossover vehicle class, which is a type of SUV with unibody structure. It has been one of the top selling SUV vehicles in the United States in recent years. The 2020 Nissan Rogue received a 5-Star SINCAP and a "GOOD" IIHS crash rating. FMVSS No. 214-pole and SINCAP MDB test data exists. A detailed FE model of a 2020 Nissan Rogue was developed using a reverse engineering process. [3]

SUV versus sedan side impact characteristics
SUV-type vehicles have significantly different side impact characteristics, especially in the 214-MDB test configuration, due to higher sill and occupant seating position, as shown in Figure 1. The higher seating position in a SUV affects load-paths and mitigates occupant loads in MDB side impact. It can be noticed from the cross-section view that the MDB bumper directly impacts the SUV's sill area, as highlighted by the red circle in Figure 1 (a), making the rocker and floor structural cross members a more significant load path for the SUV in the 214-MDB side impact configuration, compared to the sedan vehicle class. In contrast, the MDB honeycomb barrier face geometrically overlaps the entire chest and pelvis region of the occupant seated in the sedan vehicle, as shown in Figure 1 (b), while it only overlaps with the pelvis for the SUV-type vehicle. The bumper typically only partially overlaps with the sedan rocker area and overrides the sill in many cases, making the B-pillar and door the main load paths.
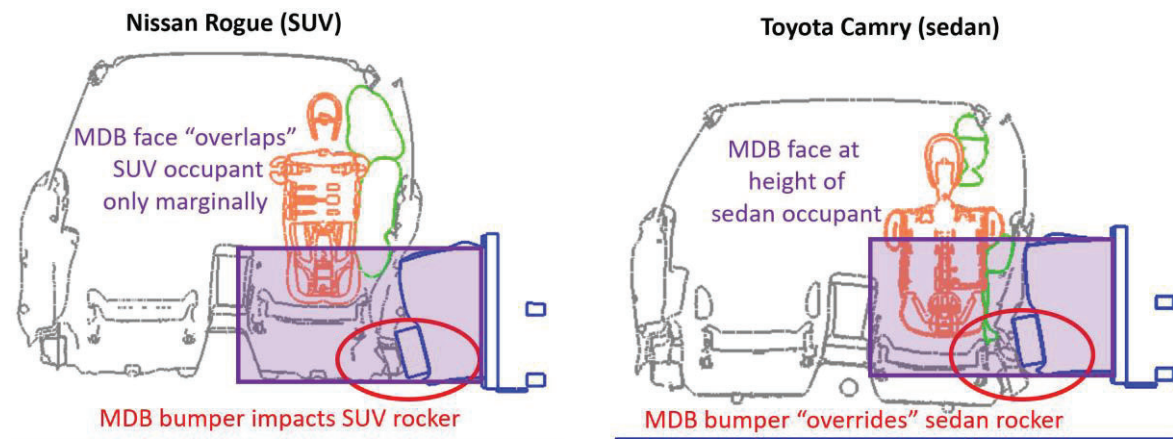

Figure 1. MDB impact location relative to sill and occupant (a) SUV; (b) sedan.

Methodology to Study the Effect of Mutual Non-Compliance

[1] Reichert, R., Mohan, P., Marzougui, D., Kan, C., & Brown, D. (2016, April 12-14), Validation of a Toyota Camry finite element model for multiple impact configurations (SAE Technical Paper 2016-01-1534). SAE 2016 World Congress and Exhibition, Detroit, MI. doi:10.4271/2016-01-1534.

[2] Reichert, R., & Kan, C.-D. (2017, May 9-11), Development of a 2015 mid-size sedan vehicle model. 11th European LS-DYNA conference, Salzburg, Austria.

[3] Reichert et. al. (2022). Nissan Rogue FE Model – Version 2, doi:10.13021/xb7g-8z06.

The baseline simulation model was validated using test data from the three FMVSS No. 214 impact configurations, and then modified to produce non-compliance for one of the requirements. Using the modified simulation model, the effect on the other two impact configurations was studied, as shown in Figure 2.
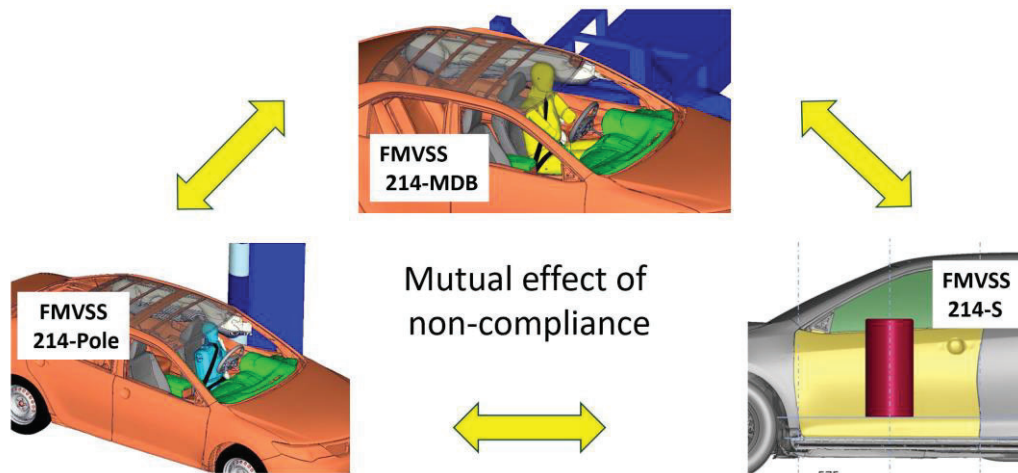

Figure 2. Process to study effect of mutual non-compliance.

The first modifications demonstrated minimal non-compliance to the static FMVSS No. 214 condition. Simulations were then performed to evaluate, how this non-compliance affected the vehicle response in the MDB and VTP conditions. Similarly, FE model variations that showed non-compliance for the MDB and VTP dynamic FMVSS No. 214 configurations were developed, and an evaluation was performed on how this would affect the vehicle response in the static and other dynamic impact configuration.

Observations that were made during the validation process and experience from previous side impact projects were used to determine reasonable structural modifications that produced the intended non-compliance for the respective impact condition. The simulation studies included the analysis of vehicle intrusion, vehicle pulse, and force criteria for the baseline and the modified simulation models.

Since dynamic FMVSS No. 214-MDB and pole impact compliance is based on anthropomorphic test device (ATD) metrics, simulations were conducted using validated models of 5th and 50th percentile side impact dummies, to verify the trends observed from the structural analyses.

Structural Performance Metric and Injury Mechanism

Velocity pulses at relevant vehicle locations, recorded by accelerometers, are a good indicator of structural performance in the FMVSS No. 214-MDB configuration, where the MDB impacts the stationary vehicle. From the author's experience working in industry and with major car manufacturers it is known that the B-pillar thorax location is used by some OEMs to judge the structural side impact performance of a vehicle. An accelerometer positioned at the middle of the B-pillar provides important information with respect to occupant loads caused by vehicle deformation and vehicle kinematics. In frontal impact configurations, interaction of the occupant with the seat and seat belt results in deceleration of the occupant coupled with the vehicle deceleration, called ride-down effect. Side impact injury mechanisms are different. In a collision where an occupied stationary vehicle is impacted by a striking vehicle from the side, occupant loads are mainly induced by the deformation of the vehicle structure and interior and the motion of the near side structure. The absolute B-pillar velocity describes the combination of the vehicle deformation and vehicle motion and is therefore a good indicator for loads relevant for occupant injury risk, which are then mainly mitigated by optimized air bags and interior components. To further explain the side impact characteristic, we can assume two extreme cases, (1) a small vehicle with low mass and no significant deformation, and (2) a heavy vehicle with a significant amount of deformation. The light vehicle would be pushed away during an impact and the heavy vehicle would not move but experience near-side structural deformation, while the occupant predominantly remains at the initial location without significant ride-down effect. The absolute velocity measured at the B-pillar is a good structural metric in side impact, because it captures well the load the occupant experiences for both cases, in the first case caused by vehicle motion, and in the second case mainly caused by vehicle deformation. Similarly, absolute velocities measured at the doors can be a good indicator for a vehicle's side impact performance,

while measurements from the doors are more likely to show questionable data in full-scale testing, due to local buckle effects and higher oscillations, compared to the B-pillar location.

The B-pillar and door locations are of special interest due to their proximity with the occupant's contact areas. Figure 3 shows an example of a door velocity and a driver's pelvis force profile. Later contact, i.e., larger initial dummy to interior clearance and lower velocity typically correlates with lower injury risk. Local effects, due to interior design and restraints also play an important role.
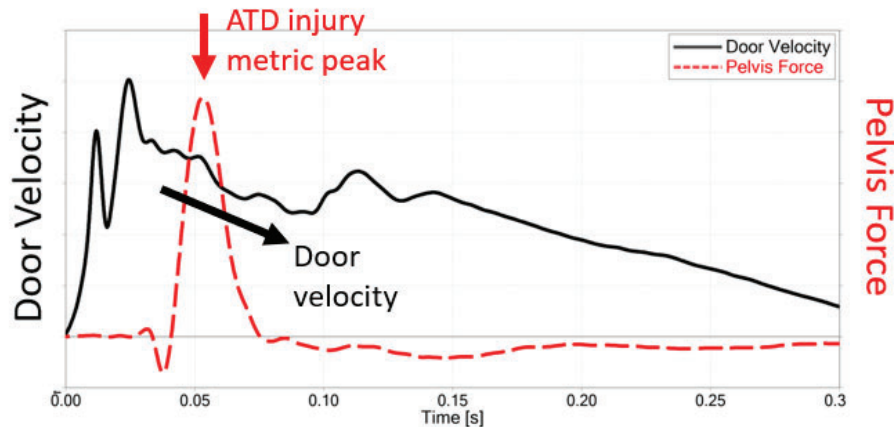

Figure 3. MDB velocity and ATD metric characteristics.

In contrast, during the FMVSS No. 214-pole configuration, the vehicle is positioned on a so-called "flying floor" and moves into the stationary rigid pole, which is aligned with the driver's head center of gravity. The vehicle is promptly decelerated and the velocity profiles at the door and B-pillar highly depend on the distance from the impact location. Therefore, the velocity profiles are less relevant in this configuration. Local effects involving the ATD, interior, and restraints play an important role.

Deformation and force versus deformation characteristics were monitored. Remaining occupant compartment space is another criterion, which is often used to judge the structural performance during a side impact, whereas deformation and contact characteristics in the early phase of the impact are relevant for FVMSS No. 214 ATD criteria. The force versus deformation criteria was used to judge the performance in the FMVSS No. 214 static (S) configuration.

Toyota Camry Sedan - Vehicle FE Model Validation

Toyota Camry sedan - MDB impact validation
Results from an existing MDB SINCAP test (NHTSA test # 9001, 2015 Toyota Camry) were used to validate the existing Toyota Camry FE model. The MDB was positioned according to the FMVSS No. 214 test procedure. Simulations were conducted with an impact velocity of 62 km/h. Crash pulses from test and simulation were compared using the objective rating tool CORA.[4] CORA rating scores range between 0 and 1, where 0 means no correlation and 1 means (close to) perfect correlation. Specifically, a CORA rating greater than 0.94 was considered excellent, values between 0.8 and 0.94 represented good, and values between 0.58 and 0.8 represented fair correlation.[5]

CORA values of 0.86 and 0.94 for vehicle and barrier acceleration pulses documented good to excellent correlation between test and simulation, respectively, as shown in Figure 4.

---

[4] Thunert, C. (2012), CORA Release 3.6 User's Manual, Version 3.6. GNS mbH, and Partnership for Dummy Technology and Biomechanics.

[5] Barbat, S., Fu, Y., Zhan, Z., Yang, R.-J., & Gehre, C. (2013, May 27-30). Objective rating metric for dynamic systems (Paper Number 13-0448). 23rd Enhanced Safety of Vehicles Conference, Seoul, Republic of Korea.
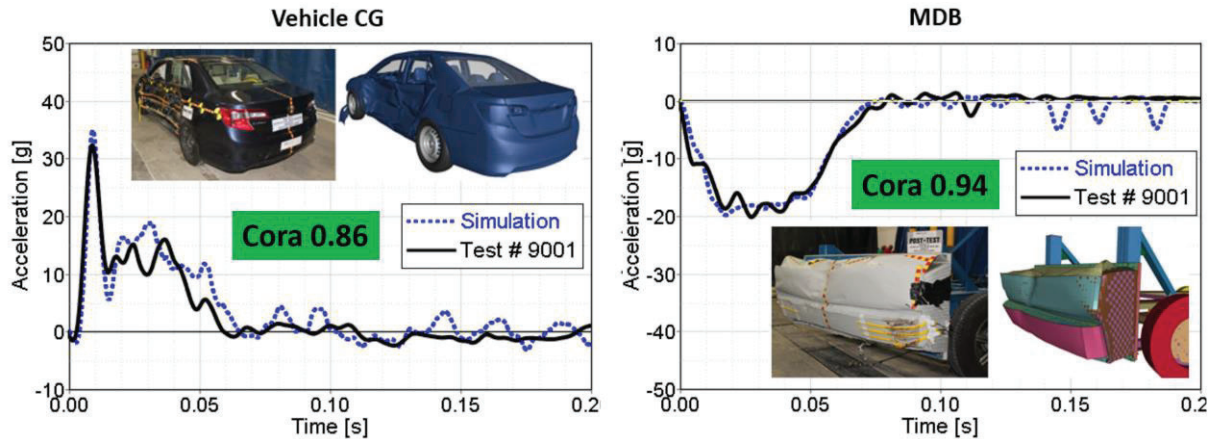
Figure 4. Toyota Camry acceleration pulse test versus simulation correlation for (a) vehicle and (b) MDB.

Deformation of the MDB honeycomb face showed similar characteristics for test and simulation, such as (1) downward tilting of the bumper and (2) higher deformation at the area that impacted the B-pillar. Exterior crush was measured at five different heights of the vehicle. The maximum value of 264 mm in the simulation compared reasonably well with the maximum value of 249 mm from the full-scale test.

Toyota Camry sedan - pole impact validation
Results from an existing FMVSS No. 214-pole test (NHTSA # 8558, 2014 Toyota Camry), were used to validate the existing Toyota Camry FE model. The vehicle was positioned at a 75° angle and impacted the stationary rigid pole according to the FMVSS No. 214-pole impact specification with 32 km/h. Figure 5 shows a top view of the exterior crush profile. The maximum value of 380 mm in the simulation compared well with the maximum value of 379 mm from the full-scale test.
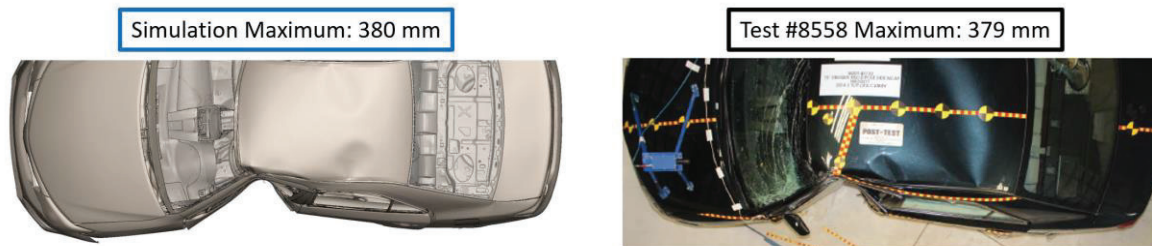

Figure 5. Toyota Camry pole impact post-crash (a) simulation and (b) test.

Crash pulses from test and simulation were compared using the objective rating tool CORA. A value of 0.96 for the comparison of the velocity pulse at the vehicle center of gravity documents excellent correlation.

Toyota Camry sedan – static door crush validation
FMVSS No. 214-static requires doors in applicable vehicles to meet minimum force requirements when the front and rear door is quasi-statically loaded with a rigid steel cylinder, as shown in Figure 6 (a). A typical force versus displacement plot is shown in Figure 6 (b). The initial and intermediate crush resistance values represent the average force to deform the door (area under force versus displacement curve divided by 6 / 12 inches). Minimum resistance force criteria depend on the test setup, i.e. with or without seats installed. A higher door crush resistance force is required for setups with seats installed, as shown in Figure 6 (c).
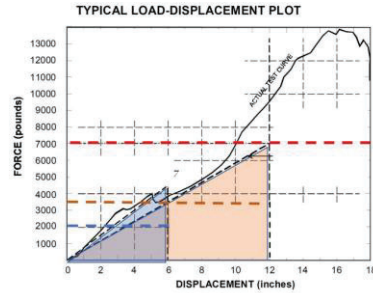
Figure 6. Sedan static door crush test (a) FMVSS 214-static setup; (b) typical force displacement plot; (c) criteria.

FMVSS No. 214-static door crush tests were conducted at the TRC in Ohio. A 2017 Toyota Camry representing the 2015 model year was purchased. The left front driver door was used to conduct the quasi-static door crush test with seat installed and the right front door was used to generate test data without seat. Figure 7 (a) and (b) show the comparison of test and baseline simulation with and without seat, respectively. The entire range of displacement until 18 inches was evaluated. Good correlation of the force versus displacement time history data was achieved represented by CORA scores of 0.90 and 0.93. Initial, intermediate, and peak resistance forces were well captured and showed values above the relevant required minimum criteria in test and simulation.
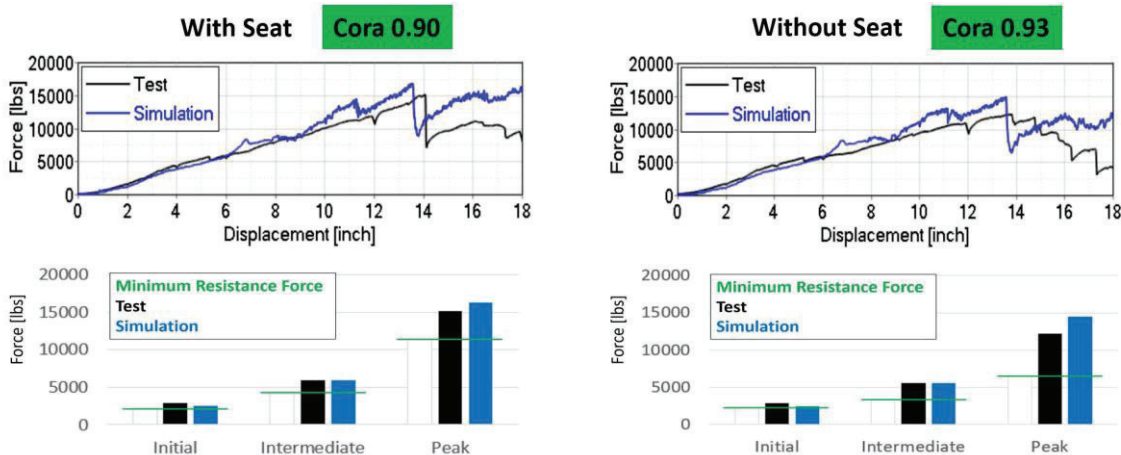

Figure 7. Sedan FMVSS 214-static validation (a) with seat; (b) without seat.

The baseline FE model was also validated using test data for the rear door. The test was automatically stopped after about 8 inches because the load cell had reached 95 percent of its capacity. Simulation and test results correlated well, represented by a CORA score of 0.91. All simulations were conducted using explicit time integration method used for dynamic crash applications. The Toyota Camry baseline FE model, which represents the 2012 and 2015 physical vehicles with respect to side impact performance, can be downloaded from GMU/CCSA's vehicle model website. [6]

Nissan Rogue SUV - Vehicle FE Model Validation

Nissan Rogue SUV - MDB impact validation
A FMVSS No. 214-MDB side impact test with a 2020 Nissan Rogue was conducted at Calspan to generate data for FE model validation. The vehicle was struck on the left side by a MDB, which was moving forward in a 27° crabbed position to the tow road guidance system at a velocity of 53 km/h. The target vehicle was stationary and was

---

[6] https://www.ccsa.gmu.edu/models

positioned at an angle of 63° to the line of forward motion. A perspective view of the conducted FMVSS No. 214-MDB test is shown in Figure 8.

Figure 8. 2020 Nissan Rogue FMVSS No. 214-MDB full-scale test.

Figure 9 shows the top view of the respective simulation using the developed 2020 Nissan Rogue FE model. Overall vehicle and barrier deformation was well captured, represented by the maximum exterior crush value of 190 mm for the test and 181 mm for the simulation. The y-velocity crash pulse time history data, which is in the dominant impact direction, showed "excellent" correlation represented by a CORA value of 0.96. The velocity time history measured at the CG of the MDB, showed excellent correlation with a CORA value of 0.96, as well.
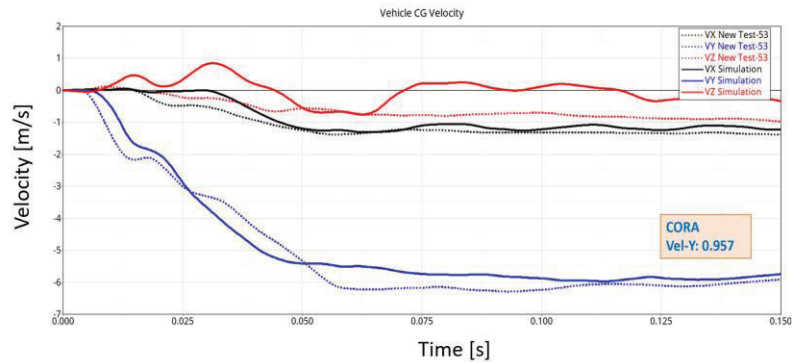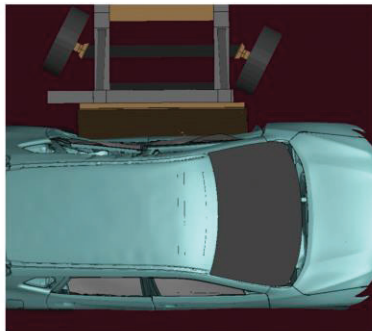

Figure 9. FMVSS No. 214-MDB validation (a) top view; (b) vehicle velocity crash pulse.

The developed 2020 Nissan Rogue FE model was also exercised at an impact velocity of 62 km/h according to the SINCAP rating procedure and compared to results from an existing full-scale test, NHTSA test #9786. Good correlation of FE model and respective test data was observed for the higher impact speed as well. The maximum exterior crush was 220 mm and 234 mm in test and simulation, respectively. The lateral velocity crash pulse time history compared well, represented by a "good" CORA value of 0.90. The MDB's velocity pulse time-history showed excellent correlation, characterized by a CORA value of 0.95.

The structural FE model was equipped with relevant interiors and restraints and the state-of-the-art 50-percent WorldSID FE model developed by PDB and distributed by Dynamore and Humanetics.[7] Figure 10 shows a comparison of characteristic values from test and simulation for the 53 km/h configurations. The maximum values compare well for all body regions. Green and red lines represent reference values for respective body regions.

---

[7] https://www.humaneticsgroup.com/products/virtual-models/side-impact-atd-virtual-models/worldsid-50m-fe
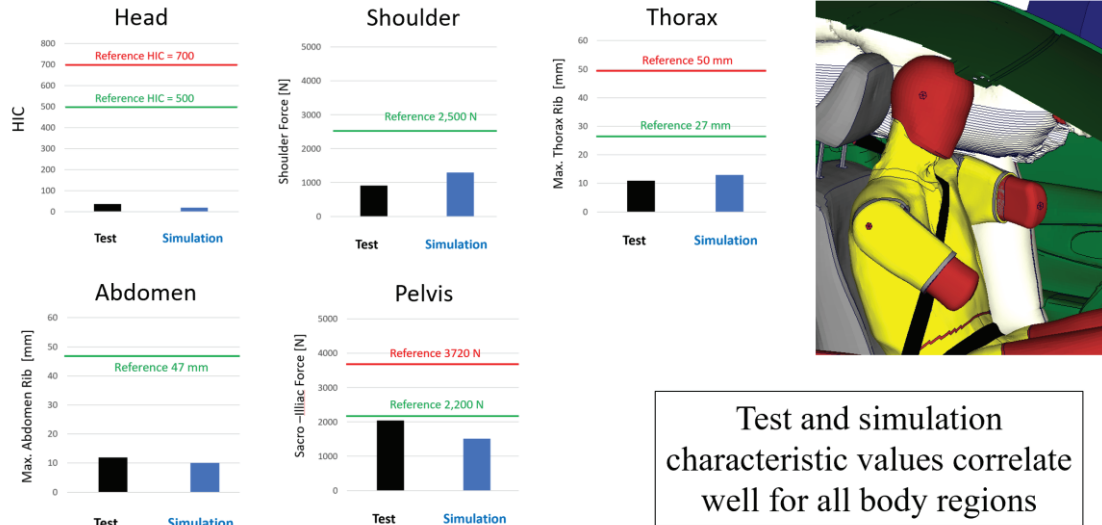
Figure 10. 53 km/h FMVSS No. 214-MDB occupant test versus simulation.

Figure 11 shows a comparison of characteristic values from test and simulation for the 62 km/h MDB configuration. Again, maximum values compared well for all body regions.
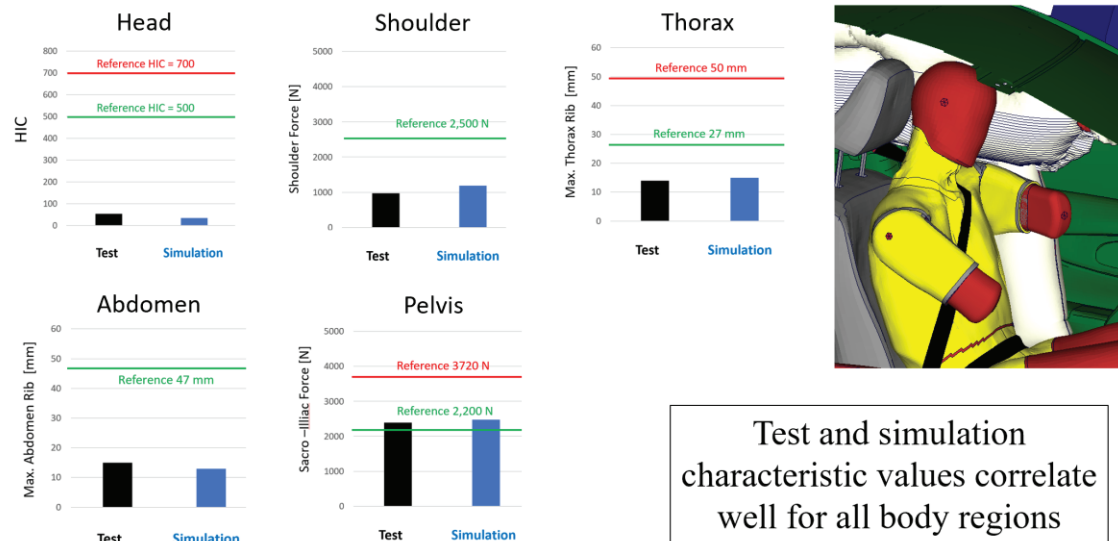
Figure 11. 62 km/h MDB occupant test versus simulation.

Nissan Rogue SUV - pole impact validation
A FMVSS No. 214-pole side impact test with a 2020 Nissan Rogue SUV was conducted at Calspan to generate data for FE model validation. The same vehicle that was previously impacted on the driver side with the MDB at 53 km/h was used. The vehicle showed no structural damage on the passenger side and could therefore be used again to conduct the FMVSS No. 214-pole impact. The subject vehicle was towed into the rigid pole at an angle of 75 degrees and a velocity of 31 km/h. One WorldSID dummy was placed in the front passenger designated seating position.
A perspective and side view of the conducted FMVSS No. 214-pole test is shown in Figure 12 (a) and (b), respectively.
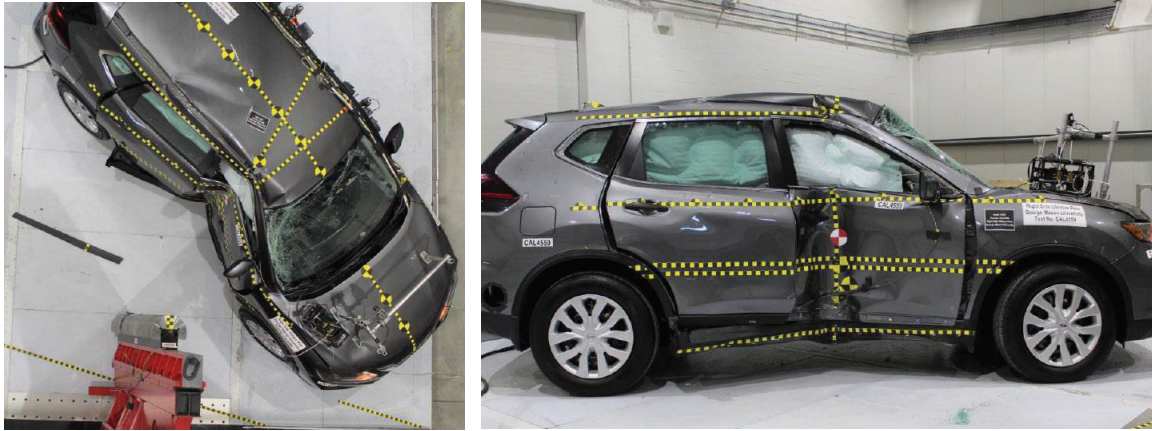
Figure 12. Nissan Rogue FMVSS No. 214-pole post-crash (a) top; (b) side view.

Figure 13 (a) shows the velocity crash pulse time history comparisons between test and simulation, which showed "good" correlation for x- and y-pulse based on a CORA value of 0.74 and 0.87, respectively. Figure 13 (b) depicts a top view of the simulation using the developed 2020 Nissan Rogue FE model. Overall vehicle deformation was reasonably well captured, represented by the maximum exterior crush of 420 mm for the simulation and 379 mm for the test. NTHSA test #9780, which was conducted at 32 km/h, showed a maximum exterior crush of 390 mm.
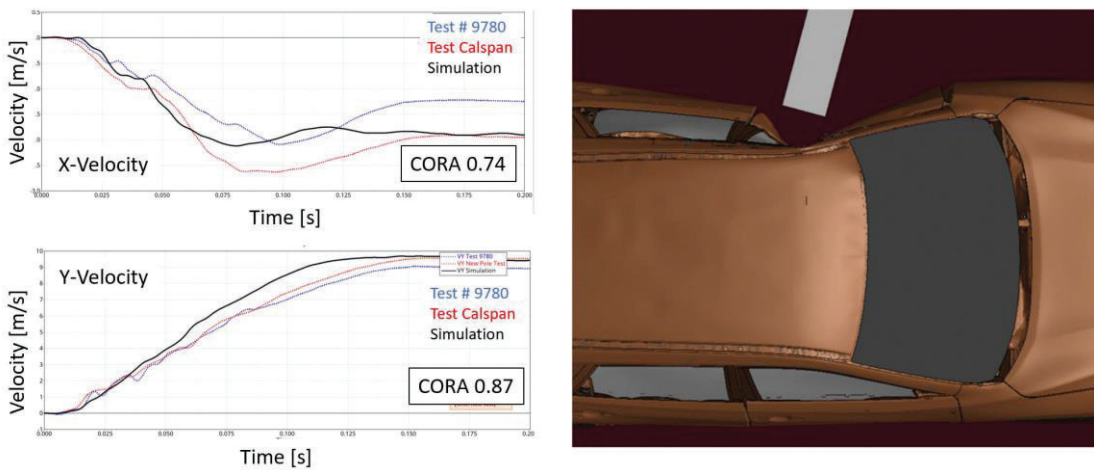
Figure 13. FMVSS No. 214-pole validation (a) velocity crash pulses; (b) top view.

Nissan Rogue SUV – static door crush validation

FMVSS No. 214-static requires doors in applicable vehicles to meet minimum force requirements when the doors are quasi-statically loaded with a rigid steel cylinder. Tests at the front and rear door of a 2020 Nissan Rogue were conducted and documented in cooperation with TRC, as shown in Figure 14.

Figure 14. Nissan Rogue FMVSS No. 214 static post crash front door.

The left front driver door was used to conduct the quasi-static door crush test with seat installed. Figure 15 shows the comparison of test and simulation.
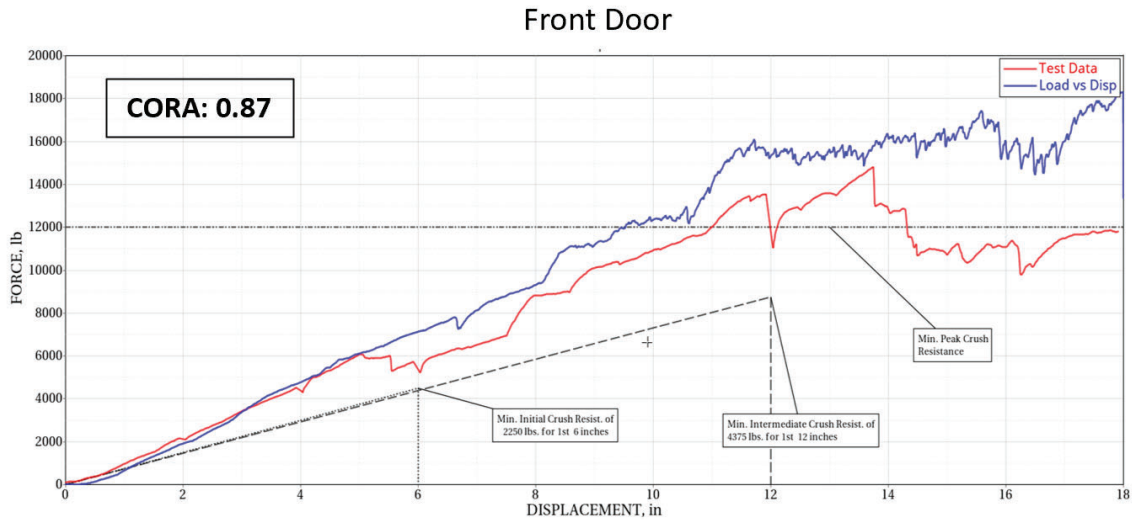
Figure 15. FMVSS No. 214 static door crush validation front door.

The entire range of displacement until 18 inches was evaluated. The FE model showed good correlation of the force versus displacement time history data, represented by a CORA value of 0.87 for the front door. Initial, intermediate, and peak resistance forces showed values above the relevant required minimum criteria in test and simulation, as shown in Figure 16.

Front Door

	Initial Force [lbs]	Intermediate Force [lbs]	Peak Force [lbs]
Requirement	2250	4375	12208 *
Test # 201103	3219	6358	14825
Simulation	3605	7878	18000

* 3.5 times the curb weight of the vehicle (3488 lbs)

Figure 16. Rogue FMVSS No. 214 static door crush resistance forces front door.

RESULTS

2015 Toyota Camry Sedan - Effect of Mutual FMVSS No. 214 Non-Compliance

2015 Toyota Camry sedan - effect of FMVSS No. 214-static non-compliance

The validated sedan baseline model was first modified in such a way that it showed non-compliance based on the minimum door crush resistance force criteria. It was found from the validation results that the initial FMVSS No. 214-static force requirement, defined for the first six inches of deformation, had the smallest margin to the minimum resistance force criteria, compared to the intermediate and peak resistance force criteria. According to the defined test procedure, the cylindric impactor does not overlap with the sill of the vehicle, as shown in Figure 17 (a). The door beam and the integrity of the door to B-pillar lock connections were found to have a significant effect on the FMVSS No. 214-static performance. Consequently, non-compliance was achieved by reducing the strength of the door beam, as shown in Figure 17 (b). The resulting initial resistance force for the first 6 inches of deformation using the modified FE model was below the required minimum force criteria, as shown by the red bar in Figure 17 (c). The intermediate resistance force showed a borderline value and was lower than in the baseline simulation. The peak resistance force was lower than in the baseline simulation as well but above the required minimum peak force requirement. Similar observations were made for the analysis with removed seat.
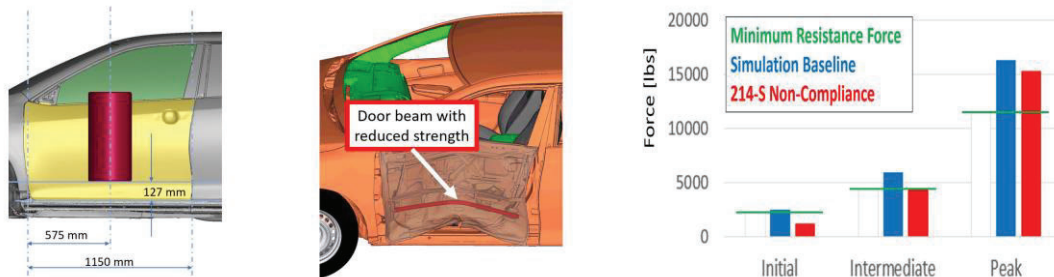
Figure 17. Sedan FMVSS No. 214-static (a) setup; (b) structural modifications; (c) force comparison.

The model that showed non-compliance for the FMVSS No. 214-static test configuration, depicted in Figure 18 (a) was then exercised in the FMVSS No. 214-MDB condition, as shown in Figure 18 (b). Structural modifications that resulted in FMVSS No. 214-static non-compliance resulted in marginally higher maximum velocity at the B-pillar and front door. Similarly, simulations with a 50th percentile WorldSID dummy in the driver seat indicated that the maximum chest deflection was marginally higher, while clearly below the defined reference criteria. The conducted simulations indicated FMVSS No. 214-MDB compliance despite 214-static non-compliance.
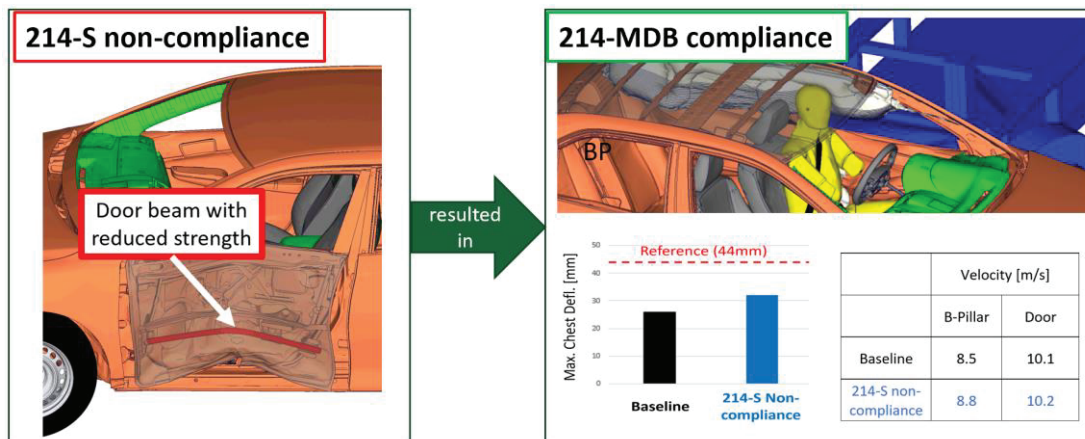
Figure 18. Sedan – Effect of FMVSS No. 214-static non-compliance for FMVSS No. 214-MDB.

The model that showed non-compliance for the FMVSS No. 214-static test configuration, depicted in Figure 19 on the left was then exercised in the FMVSS No. 214-pole condition, as shown in Figure 19 on the right. Structural modifications that resulted in FMVSS No. 214-static non-compliance resulted in similar structural deformation in

the 214-pole configuration as the FMVSS No. 214-static compliant baseline version. The maximum exterior crush was marginally higher. Similarly, simulations with a 5th percentile SID-IIs dummy model, developed by ANSYS LST, in the driver seat indicated that the maximum combined pelvis force was similar to the baseline simulation, clearly below the defined reference criteria. The conducted simulations indicated FMVSS No. 214-pole compliance despite 214-static non-compliance.
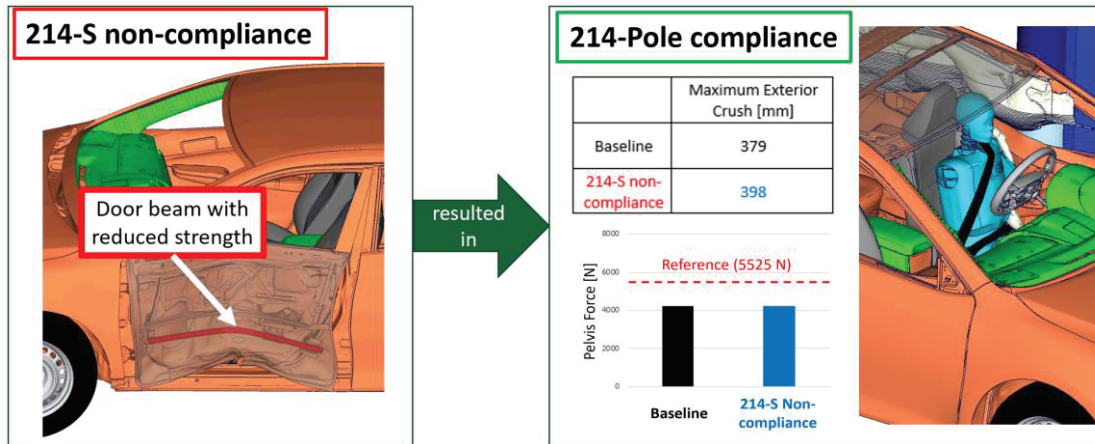
Figure 19. Sedan FMVSS No. 214-static non-compliance for FMVSS No. 214-pole.

The reduced strength for door beam, that resulted in 214-static non-compliance did not significantly affect the performance in the 214-MDB condition which mainly relies on B-pillar components. Similarly, it did not significantly affect the performance in the 214-pole condition, where the vehicle impacts the pole at the front door overlapping with the sill.

2015 Toyota Camry sedan - effect of FMVSS No. 214-MDB non-compliance
The validated Toyota Camry FE baseline model was modified in such a way that it showed non-compliance for the FMVSS No. 214-MDB configuration. Figure 20 (a) shows the parts with reduced strength in red. The structural B-pillar components play an important role for the MDB condition. This is especially true for the sedan vehicle with no significant overlap of the vehicle sill and the barrier bumper, as shown in the cross-section view in Figure 20 (b).
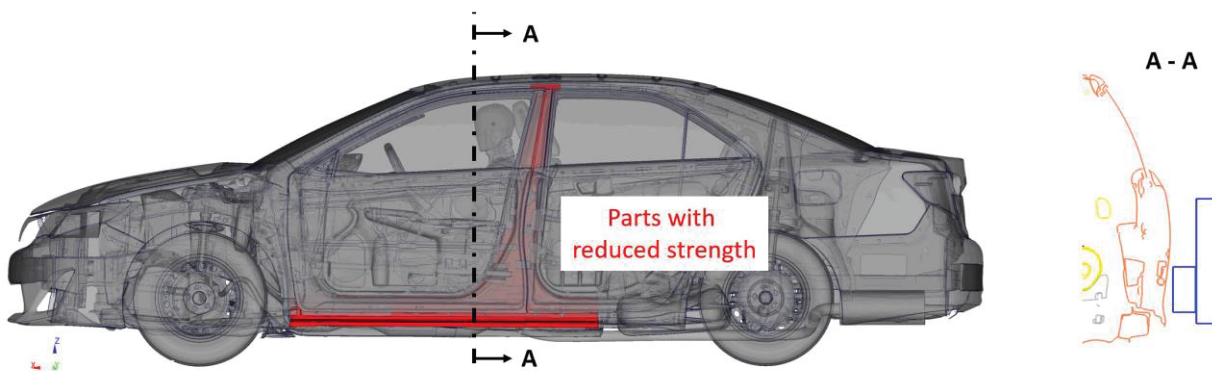
Figure 20. Sedan – FMVSS No. 214-MDB (a) modifications and (b) crosssection view.

A detailed comparison of modified parts in this and following simulation studies is documented in the corresponding NHTSA research report. [8] The model that showed non-compliance for the FMVSS No. 214-MDB configuration, shown in Figure 21 (a) was then exercised in the FMVSS No. 214-static door crush condition, as shown in Figure 21

[8] Reichert, R., Kan, C.-D., & Park, C.-K. (2022, September). Crash simulation of FMVSS No. 214 safety performance (Report No. DOT HS 813 276). National Highway Traffic Safety Administration.

(b). Structural modifications that resulted in FMVSS No. 214-MDB non-compliance resulted in marginally lower initial and intermediate force levels in the quasi-static configuration. Values were marginally lower than for the baseline FE model, but above the minimum required resistance force, defined for FMVSS No. 214 compliance. The conducted simulations indicated FMVSS No. 214-static door crush resistance force compliance despite dynamic 214-MDB non-compliance.

Figure 21. Sedan – effect of FMVSS No. 214-MDB non-compliance for FMVSS No. 214-static.

The model that showed non-compliance for the FMVSS No. 214-MDB configuration, shown in Figure 22 on the left was then exercised in the FMVSS No. 214-pole condition, as shown in Figure 22 on the right. Structural modifications that resulted in FMVSS No. 214-MDB non-compliance resulted in similar structural deformation in the FMVSS No. 214-pole configuration as the baseline. The maximum exterior crush was marginally higher. Similarly, simulations with a 5th percentile ATD in the driver seat indicated that the maximum combined pelvis force was marginally higher than in the baseline simulation, while clearly below the defined reference criteria.
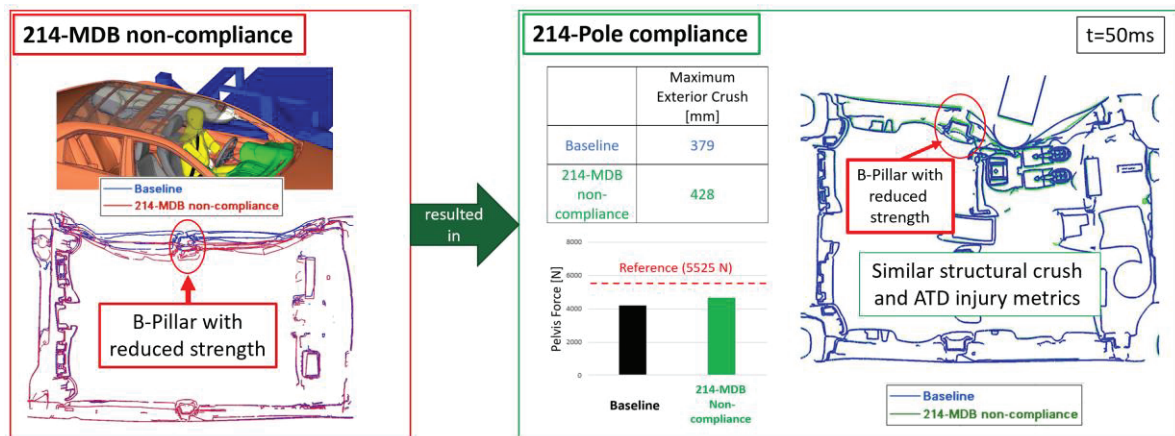
Figure 22. Sedan – effect of FMVSS No. 214-MDB non-compliance forFMVSS No. 214-pole.

The conducted simulations indicated FMVSS No. 214-pole compliance despite 214-MDB non-compliance. The reduced strength for B-pillar components, that resulted in 214-MDB non-compliance did not significantly affect the performance in the 214-static condition, which mainly relies on the door components. Similarly, it did not significantly affect the performance in the 214-pole condition, where the vehicle impacts the pole at the front door overlapping with the sill and vehicle floor.

2015 Toyota Camry sedan - effect of FMVSS No. 214-pole non-compliance
The validated Toyota Camry FE baseline model was then modified in such a way that it showed non-compliance for the FMVSS No. 214-pole configuration. Figure 23 shows the parts with reduced strength in red and yellow,

compared to the baseline model. The sill components and the driver seat cross member play an important role for the oblique side pole impact condition. The Toyota Camry and some other vehicles also use an additional reinforcement component, which is specifically designed and positioned for the pole impact configuration, shown in yellow in Figure 23.
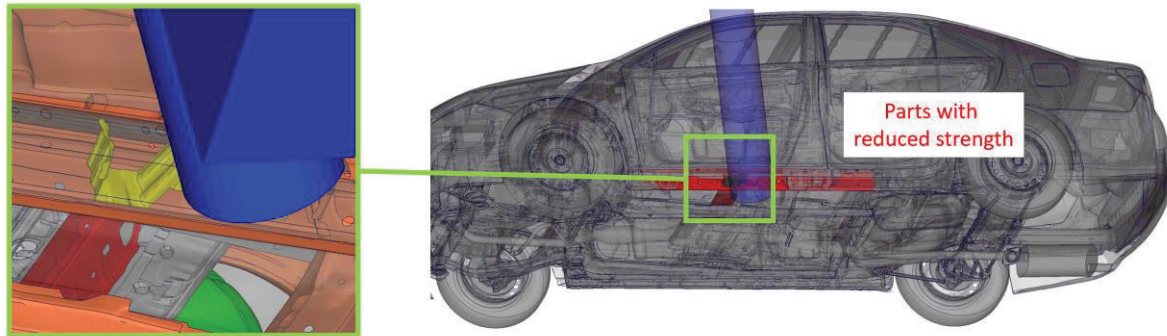
Figure 23. Sedan – parts with reduced strength resulting in FMVSS No. 214-pole non-compliance.

The applied modifications, resulted in higher maximum exterior crush and higher occupant pelvis force in the FMVSS No. 214-pole impact, as shown in Figure 24 on the left. The model that showed non-compliance for the FMVSS No. 214-pole configuration was then exercised in the FMVSS No. 214-static door crush condition, as shown in Figure 24 on the right. Structural modifications that resulted in FMVSS No. 214-pole non-compliance resulted in marginally lower initial and intermediate door crush resistance force levels in the 214-static test configuration. Values were above the minimum required resistance force. The conducted simulations indicated FMVSS No. 214-static door crush compliance despite dynamic FMVSS No. 214-pole non-compliance.
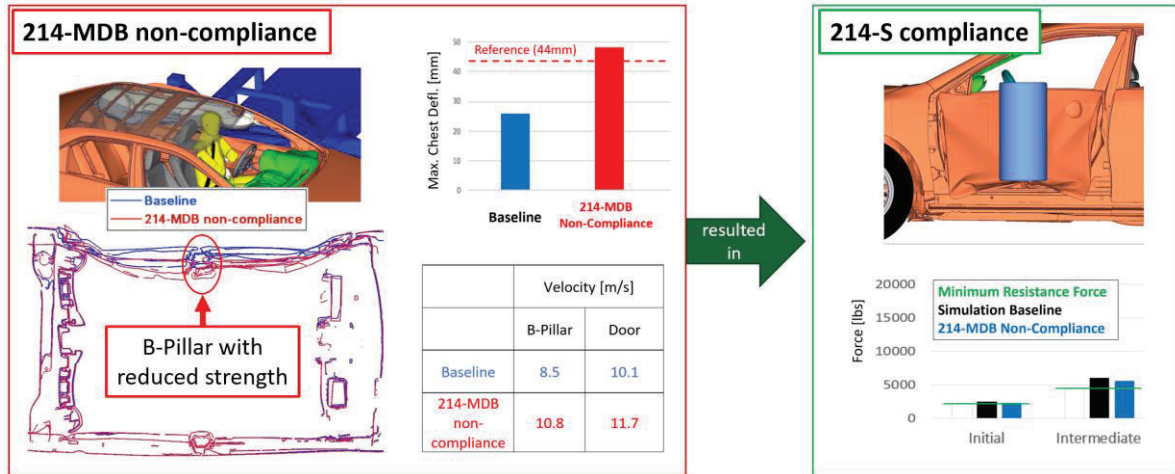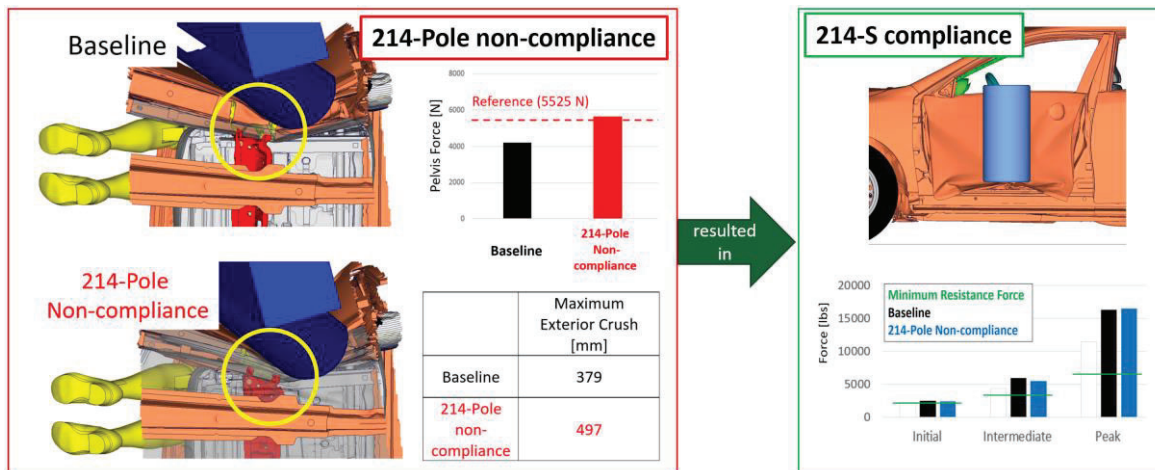

Figure 24. Sedan – effect of FMVSS No. 214-pole non-compliance for FMVSS No. 214-static.

The model that showed non-compliance for the FMVSS No. 214-pole configuration, depicted in Figure 25 on the left was then exercised in the FMVSS No. 214-MDB condition, as shown in Figure 25 on the right.
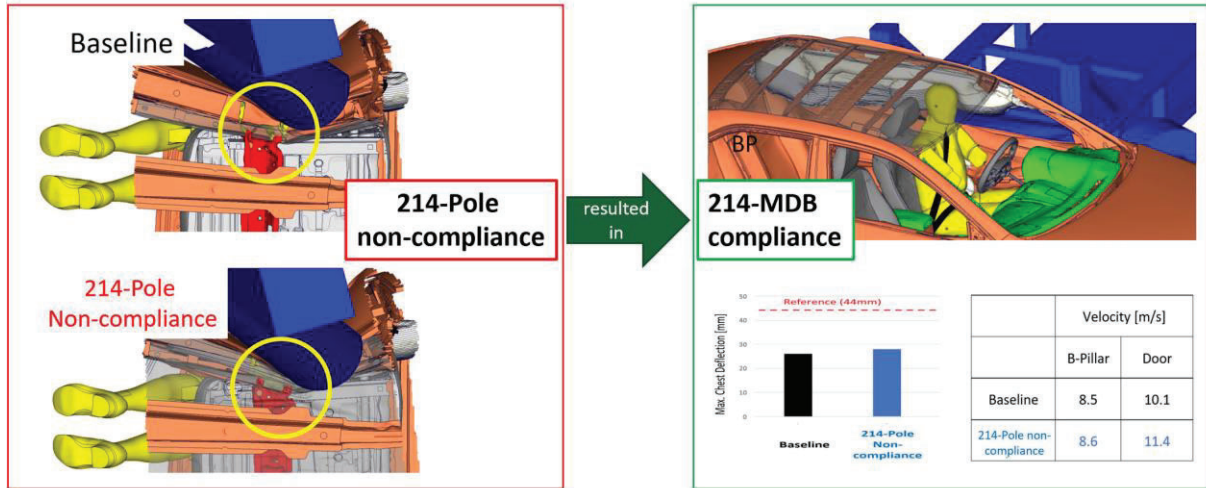
Figure 25. Sedan – effect of FMVSS No. 214-pole non-compliance for FMVSS No. 214-MDB.

Structural modifications that resulted in FMVSS No. 214-pole non-compliance resulted in similar maximum B-pillar and higher door velocity in the MDB configuration when compared to the baseline simulation. The simulations with a 50th percentile dummy in the driver seat indicated that the maximum chest deflection was marginally higher compared to the baseline simulation, while clearly below the defined reference criteria. The conducted simulations indicated FMVSS No. 214-MDB compliance despite pole non-compliance.

The reduced strength for sill and seat cross member components, that resulted in FMVSS No, 214-pole non-compliance did not significantly affect the performance in the 214-static condition which mainly relies on the door components. Similarly, the 214-MDB condition, which mainly relies on the B-pillar strength, was only affected to an extent that did not result in 214-MDB non-compliance.

2020 Nissan Rogue SUV - Effect of Mutual FMVSS No. 214 Non-Compliance

2020 Nissan Rogue SUV - effect of FMVSS No. 214-static non-compliance
The validated 2020 Nissan Rogue FE baseline model, representing the SUV vehicle category, was first modified in such a way that it showed non-compliance for the FMVSS No. 214-static static door crush resistance requirement. According to the defined test procedure, the cylindric impactor does not overlap with the sill of the vehicle. The two door beams, two door outer cross members, and the integrity of the door to B-pillar lock connections were found to have a significant effect on the FMVSS No. 214-static performance. Consequently, non-compliance was achieved by reducing the strength of the door beams and door cross members, as show in Figure 26 (a). The resulting initial resistance force for the first 6 inches of deformation and the intermediate door resistance force between 6 and 12 inches of intrusion using the modified FE model was below the required minimum force criteria, as shown by the red bar in Figure 26 (a). The peak resistance force was also significantly lower than in the baseline simulation, but above the required minimum peak force requirement. The model that showed non-compliance for the FMVSS No. 214-static test configuration was then exercised in the FMVSS No. 214-MDB condition, as shown in Figure 26 (b).

Figure 26. SUV – (a) FMVSS No. 214-static non-compliance; (b) effect for FMVSS No. 214-MDB.

Structural modifications that resulted in FMVSS No. 214-static non-compliance resulted in marginally higher maximum velocity at the B-pillar. Similarly, simulations with a 50th percentile ATD in the driver seat indicated that the maximum chest deflection and pelvis loads were marginally higher, while clearly below defined reference criteria. The conducted simulations indicated FMVSS No. 214-MDB compliance despite 214-static non-compliance for the SUV-type vehicle.

The model that showed non-compliance for the FMVSS No. 214-static test configuration, depicted in Figure 27 (a) was then exercised in the FMVSS No. 214-pole condition, as shown in Figure 27 (b). Structural modifications that resulted in FMVSS No. 214-static non-compliance resulted in similar structural deformation in the FMVSS No. 214-pole test configuration. The maximum exterior crush was marginally higher. Similarly, simulations with a 50th percentile ATD in the driver seat indicated that the maximum combined pelvis force was similar to the baseline simulation, clearly below the defined reference criteria. Rocker and floor cross members were found to be the main load path in the pole impact configuration, and roof components also contributed to mitigate deformation. The structural design changes, which were limited to door components, had therefore only a limited effect for the FMVSS No. 214-pole configuration. The conducted simulations indicated FMVSS No. 214-pole compliance despite 214-static non-compliance.
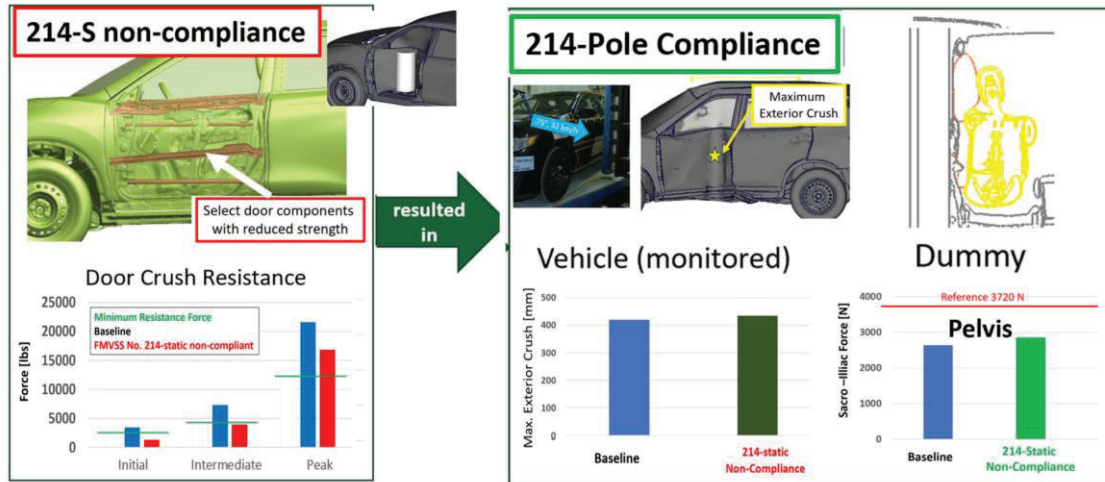
Figure 27. SUV – (a) FMVSS No. 214-static non-compliance; (b) effect for FMVSS No. 214-pole impact.

The reduced strength for door components, that resulted in 214-static non-compliance did not significantly affect the performance in the 214-MDB condition, which mainly relies on B-pillar and sill components. Similarly, it did not significantly affect the performance in the FMVSS No. 214-pole impact.

2020 Nissan Rogue SUV - effect of FMVSS No. 214-MDB non-compliance
The validate Nissan Rogue baseline model was then modified in such a way that it showed non-compliance for the FMVSS No. 214-MDB configuration. Figure 28 (a) shows the parts with reduced strength in red. The structural B-pillar components play an important role for the MDB condition like the sedan vehicle class. In addition, due to a significant overlap of the vehicle sill and the barrier bumper, as illustrated in the cross-section view shown Figure 28 (a), the lower door beam and rocker components affected performance in the MDB configuration. Some of the rocker parts extended to the A-pillar. Reducing the material strength and thickness for the components shown in red, resulted in higher structural deformation and consequently higher occupant loads. The pelvis load for the modified SUV simulation model impacted by the MDB at 53 km/h, represented by the red bar, significantly increased compared to the baseline model, represented by the blue bar. When impacting the modified FE model at the rating speed of 62 km/h, even higher pelvis forces were recorded, as expected, and represented by the dark red bar. The model with significantly increased pelvis forces was considered non-compliant with respect to the FMVSS No. 214-MDB configuration.
The model that showed non-compliance for the FMVSS No. 214-MDB impact was then exercised in the FMVSS No. 214-static door crush condition, as shown in Figure 28 (b).
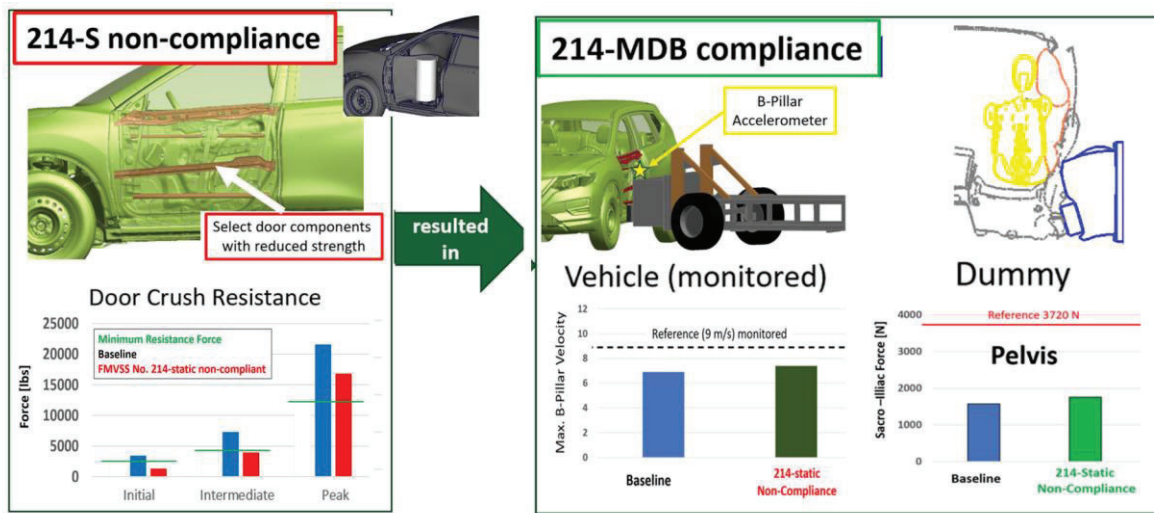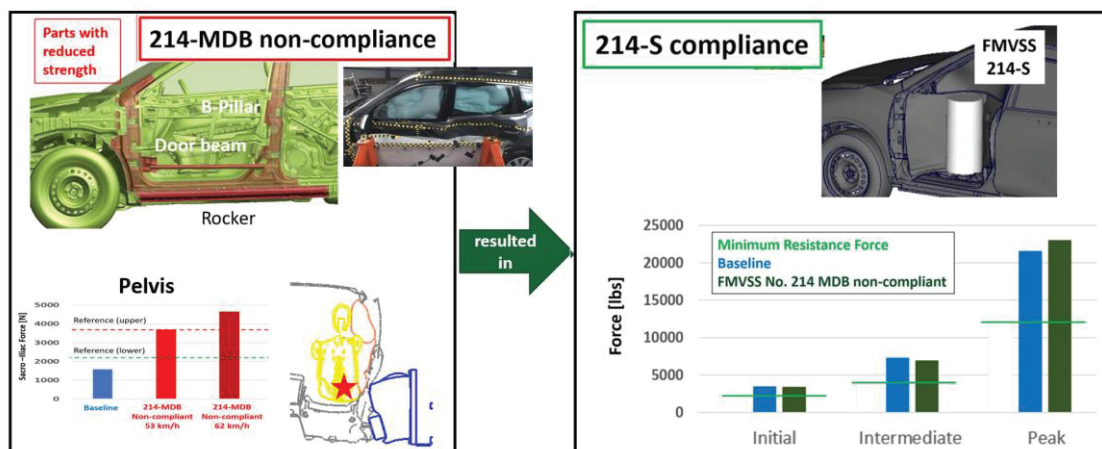

Figure 28. SUV – (a) FMVSS No. 214-MDB non-compliance; (b) effect for FMVSS No. 214-static.

Structural modifications that resulted in FMVSS No. 214-MDB non-compliance resulted in marginally lower initial and intermediate force levels in the quasi-static configuration. Values were marginally lower than for the baseline FE model, but clearly above the minimum required resistance force, defined for FMVSS No. 214 compliance. The peak resistance force was clearly above the required force level for the baseline and modified model. The conducted simulations indicated FMVSS No. 214-static door crush resistance force compliance despite dynamic 214-MDB non-compliance.

The model that showed non-compliance for the FMVSS No. 214-MDB configuration, depicted in Figure 29 (a) was then exercised in the FMVSS No. 214-pole condition, as shown in Figure 29 (b). Structural modifications that resulted in FMVSS No. 214-MDB non-compliance resulted in higher structural deformation and pelvis loads in the FMVSS No. 214-pole configuration. Simulations with a 50th percentile ATD in the driver seat indicated that the maximum combined pelvis force for the modified model, represented by the brown bar, was significantly higher than in the baseline simulation, represented by the blue bar. It exceeded the reference value, represented by the horizontal, red dashed line.
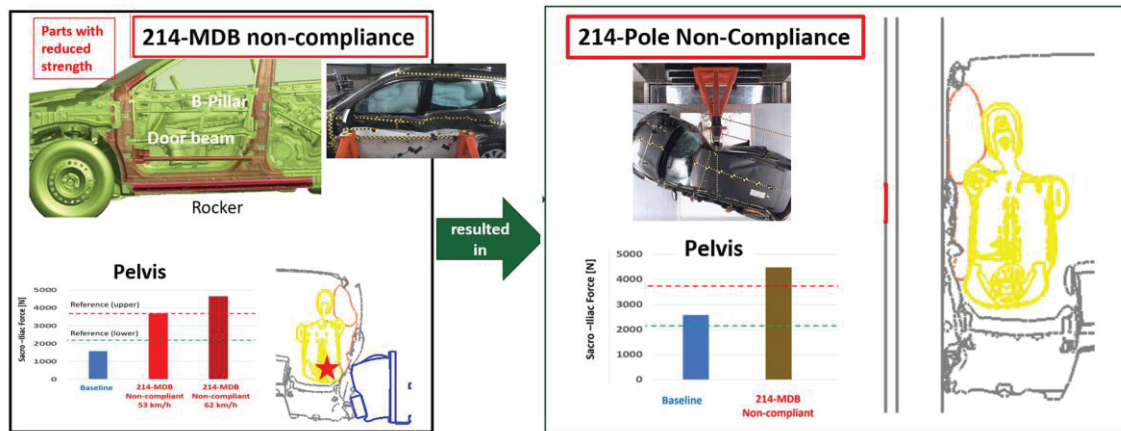
Figure 29. SUV – (a) FMVSS No. 214-MDB non-compliance; (b) effect for FMVSS No. 214-pole.

The conducted simulations indicated FMVSS No. 214-pole non-compliance for a model that showed 214-MDB non-compliance. The reduced strength for rocker and lower door beam parts in addition to the reduced strength of the B-pillar components, that resulted in 214-MDB non-compliance did not significantly affect the performance in the 214-static condition which mainly relies on the door components. However, it did significantly affect the performance in the FMVSS No. 214-pole condition, where the vehicle impacts the pole at the front door overlapping with the sill and vehicle floor. Occupant loads are typically higher in the pole impact configuration than in the MDB configuration for SUV vehicles with higher occupant seating positions, which contributed to the observed effects. While the MDB only marginally overlaps with the occupant, the rigid pole that extends from the floor to above the roof, can generally cause higher occupant loads for the SUV-type vehicle.

2020 Nissan Rogue SUV - effect of FMVSS No. 214-pole non-compliance
The validate 2020 Nissan Rogue SUV FE baseline model was then modified in such a way that it showed non-compliance for the FMVSS No. 214-pole configuration. Figure 30 (a) shows the parts with reduced strength in red, compared to the baseline model. The sill components and the driver seat cross member play an important role for the oblique side pole impact condition. A combination of weakening these components together with the upper door cross member and lower door bar, select roof parts, and rocker parts that extend to the B-pillar, resulted in non-compliance in the side pole impact configuration. This is illustrated by the increased pelvis loads for the modified SUV model, represented by the brown bar in Figure 30 (a), compared to the baseline FE model, represented by the blue bar. The applied modifications resulted in higher maximum exterior crush and higher occupant pelvis force in the FMVSS No. 214-pole impact, as shown in Figure 30 (a).

The model that showed non-compliance for the FMVSS No. 214-pole configuration was then exercised in the FMVSS No. 214-static door crush condition, as shown in Figure 30 (b).
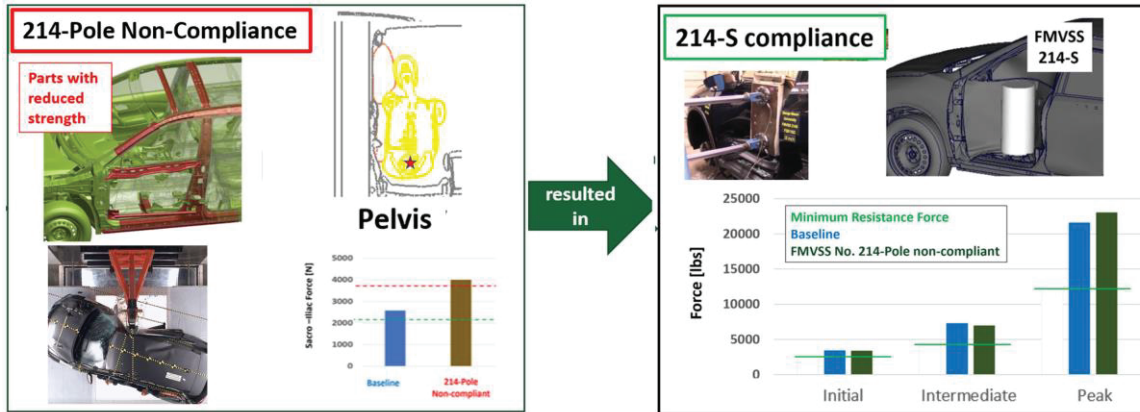
Figure 30. SUV – (a) FMVSS No. 214-pole non-compliance; (b) effect for FMVSS No. 214-static.

Structural modifications that resulted in FMVSS No. 214-pole non-compliance resulted in marginally lower initial and intermediate door crush resistance force levels in the 214-static test configuration. The peak resistance force was clearly above the required force level for the baseline and modified model. All values were above the minimum required resistance force. The conducted simulations indicated FMVSS No. 214-static door crush compliance despite dynamic FMVSS No. 214-pole non-compliance.

The model that showed non-compliance for the SUV FMVSS No. 214-pole configuration, depicted in Figure 31 (a) was then exercised in the FMVSS No. 214-MDB condition, as shown in Figure 31 (b).
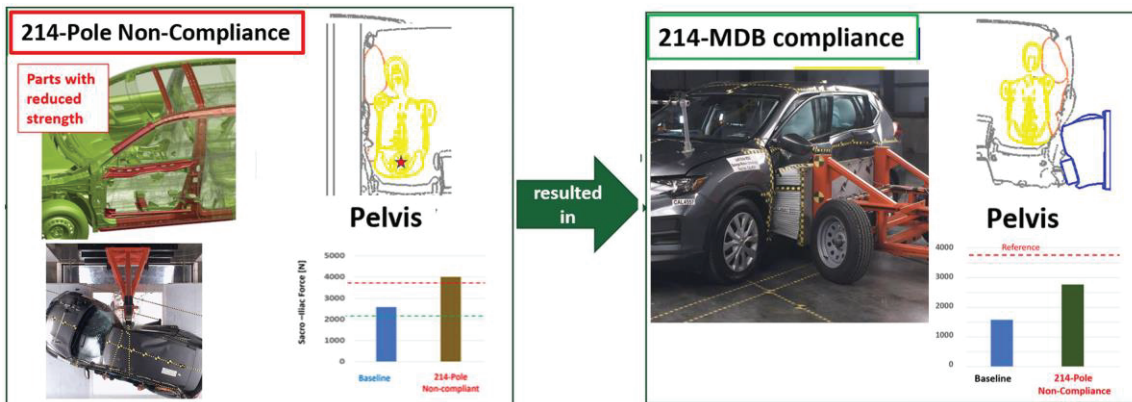
Figure 31. SUV – (a) FMVSS No. 214-pole non-compliance; (b) effect for FMVSS No. 214-MDB.

Structural modifications that resulted in FMVSS No. 214-pole non-compliance resulted in higher structural deformation and velocities also in the MDB configuration when compared to the baseline simulation. B-pillar velocity increased marginally from 8.5 m/s to 8.6 m/s, while the door velocity increased significantly from 10.1 m/s for the baseline model to 11.4 m/s for the model that did not comply with FMVSS No. 214-pole requirements. The simulations with a 50th percentile dummy in the driver seat indicated that the maximum combined sacroiliac pelvis force was significantly higher compared to the baseline simulation. Since the baseline simulation showed a relatively moderate value, which is often the case for SUV-type vehicles in the MDB configuration and even more so for chest load, the pelvic load for the modified model was still clearly below the defined reference criteria. The conducted simulations indicated FMVSS No. 214-MDB compliance despite pole non-compliance.

The reduced strength of relevant sill, roof, door, and B-pillar components, that resulted in FMVSS No, 214-pole non-compliance did not significantly affect the performance in the 214-static condition which mainly relies on the door components. However, it significantly affected the performance in the 214-MDB condition, resulting in higher structural and occupant loads. Due to the relatively low MDB baseline loads, values were below reference criteria resulting in 214-MDB compliance for the model that did not comply with FMVSS No. 214-pole.

DISCUSSION

Mutual Effect of FMVSS No. 214 non-compliance

The three FMVSS No. 214 configurations mainly rely on different vehicle structural areas, as shown in Figure 32.
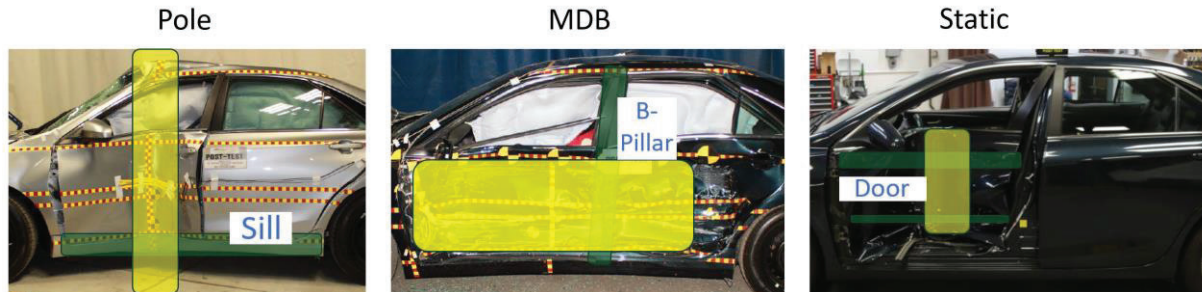
Figure 32. Main load paths during FMVSS No 214 (a) pole; (b) MDB; and (c) static door crush.

(1) FVMSS No. 214-static door crush, where a cylindric impactor does not overlap with the sill or the B-pillar, is mainly affected by door strength characteristics.
(2) FVMSS No. 214-MDB, where the moving barrier only marginally overlaps with the sill of a sedan vehicle, is mainly affected by B-pillar strength and deformation characteristics; and
(3) FMVSS No. 214-pole, where the moving vehicle impacts the stationary rigid pole at the front door, is mainly affected by sill and adjacent reinforcement components.

Hence, non-compliance of one of the FMVSS No. 214 configurations did not result in non-compliance for the respective other two load cases for the sedan vehicle. Similarly, non-compliance of the FMVSS No. 214-static configuration did not significantly affect the MDB and VTP load cases. In contrast to the sedan vehicle class, MDB and VTP configurations use sill and floor components as relevant load paths, due to the higher sill of the SUV type vehicle relative to the ground and relative to the MDB. As a result, non-compliance of the FMVSS No. 214-MDB configuration resulted in non-compliance in the FMVSS No. 214-pole load case for the Nissan Rogue vehicle. While non-compliance of the SUV VTP scenario also resulted in higher loads for the SUV MDB configuration, it did not result in MDB non-compliance due to the relatively low MDB baseline vehicle and occupant loads. These differences for the Toyota Camry and Nissan Rogue vehicles are considered to be representative for the sedan and SUV vehicle classes. Note that the differences in vehicle sill and seating position height for the sedan and SUV vehicle classes, only resulted in differences with respect to mutual effects for the MDB and Pole modifications. The FMVSS No. 214-static configuration was not significantly affected by non-compliant MDB and pole configurations for either vehicle class. Similarly, FMVSS No. 214-static non-compliance did not significantly affect MDB and VTP configurations for sedan and SUV vehicle classes, due to the different load paths used.

In addition to metrics relevant for FMVSS No. 214 compliance, additional metrics were studied during this research to understand, if dynamic performance measurements from the MDB or pole impact could be used as surrogate for the FMVSS No. 214-static configuration, as discussed in the next section.

Dynamic Performance Measurements as a Surrogate for the Static Test

In addition to evaluating the effect of mutual non-compliance for each of the three FMVSS No. 214 impact scenarios, the results of this study were used to explore options for developing performance criteria so that the FMVSS No. 214 dynamic MDB and/or VTP tests could be used as replacements for the static door crush resistance requirements. Currently, neither of the dynamic 214 test procedures measure door crush resistance force.

Candidate dynamic performance metrics

Results from the sedan and SUV simulation studies were used to evaluate if it is feasible to use a dynamic performance measurement as a surrogate for the static test. Figure 33 depicts potential structural metrics from the FMVSS No. 214-MDB and FMVSS No.214-pole impact tests.
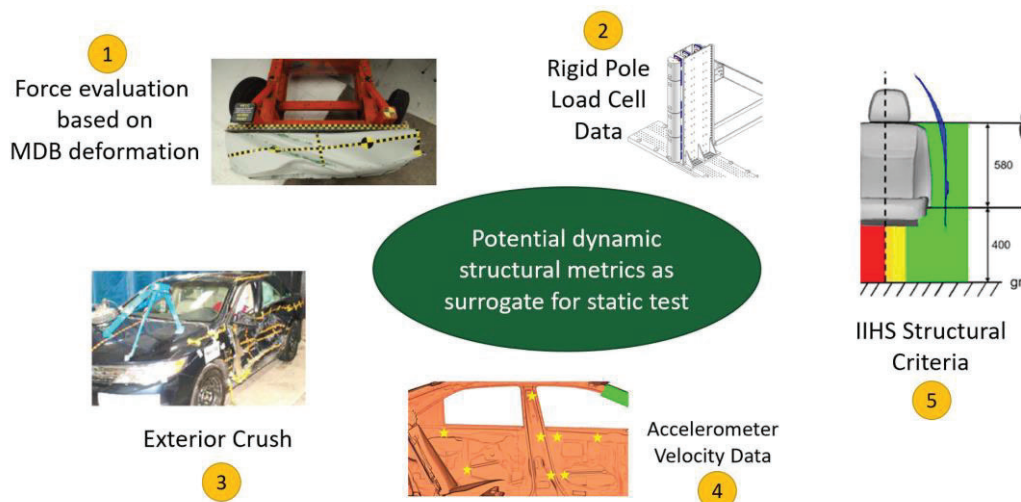
Figure 33. Candidate structural metrics from dynamic tests as surrogate for static test.

Deformation, load cell forces, and acceleration-based data can be recorded during the dynamic MDB and pole impact configurations. Five candidate structural metrics are outlined below and discussed in the following sections.

1) The MDB's honeycomb face has well-defined force-deformation characteristics. Digitizing the MDB barrier surface, pre- and post-crash, allows to calculate the deformation at relevant areas, for example where the door is being struck. From the residual deformation, the force can be calculated. A similar approach has been used for the Progressive Deformable Barrier in a frontal offset configurations.[9]

2) Rigid pole load cells at different heights are standard instrumentation during most FVMSS No. 214-pole impact tests. The force time history data combined with vehicle accelerometer data, which can be used to calculate the displacement and deformation of the vehicle exterior, permits generation of a force versus displacement graph, similar to the one used for the FMVSS No. 214-static door crush resistance tests.

3) Residual exterior crush is typically measured at five different heights of the vehicle, i.e. the sill, the height of the occupant hip point, the mid door location, close to window opening, and at the roof for dynamic FMVSS No. 214-MDB and pole full-scale tests. The largest exterior crush is observed at the front door in many cases. These residual exterior crush measurements can indicate the structural side impact performance and were considered as candidate metric to indicate door crush resistance.

4) Accelerometer data, specifically absolute velocity time history data recorded at the near-side B-pillar and doors, is a good structural indicator for side impact performance of a vehicle, used by many car manufacturers during the vehicle development process.

5) The Insurance Institute for Highway Safety has a well-defined structural criterion that measures the remaining occupant compartment space after a IIHS MDB side impact crash based on B-pillar deformation relative to the middle of the seat.

Metrics based on vehicle accelerometer data
Velocity time history data derived from accelerometers located at the impact-side B-pillar and doors during a barrier side impact configuration is used by many OEMs as a structural performance metric. In addition to interior design and air bag performance, absolute velocity measured at these locations are an important factor for occupant loads. Occupants positioned in the front and rear seats during a side impact typically do not benefit from the so-called "ride-down." During frontal impact scenarios, a distinct crash-energy absorption structure, also called frontal crumble zone, causes the vehicle to decelerate more slowly. Occupant loads are then significantly mitigated by the frontal air bags and seat belts before a potentially injurious contact with the vehicle interior occurs. In contrast, the

---

[9] Park, C.-K., Hong, S.-W., Mohan, P., Morgan, R. M., Kan, C.-D., Lee, K., Park, S., & Bae, H. (2016). Simulation of progressive deformable barrier (PDB) tests. 10th International LS-DYNA Users Conference, Detroit, MI.

occupants in side impact are more directly loaded by contacting the vehicle's structure, interiors, and side air bags. Seat and seatbelts can only generate a much smaller ride-down benefit due to the lateral motion and missing crumple zone.

To determine relevant vehicle metrics for side impact scenarios, it is important to note that vehicle motion relative to the occupant is typically a combination of intrusion and global vehicle kinematics. For example, a vehicle with a low mass can produce high structural velocity in the absence of significant intrusion. From the author's experience working in industry and with major car manufacturer's, it is known that quantitative criteria for the structural velocity exist at many OEMs to judge the side impact performance of a vehicle in U.S. NCAP, IIHS, and EuroNCAP side impact barrier configurations.

Accelerometer locations at the middle of the B-pillar and at the door are close to the occupant-to-vehicle contact areas. The B-pillar location can be considered the most reliable accelerometer location with respect to full-scale testing, while the accelerometers at the door, mounted to relatively thin structural components, can produce high oscillations and questionable data. Figure 34 (b) depicts the B-pillar and door accelerometer locations evaluated during the Nissan Rogue simulation study. The results from two simulations were used to evaluate the usability of accelerometer data from the FMVSS No. 214-MDB test as a surrogate for the static test. Maximum absolute velocity values are compared for the SUV baseline model and the model variation that did not comply with the FMVSS No. 214-static door crush resistance requirement. Note that the maximum velocity at the middle of the B-pillar was identical, as shown in Figure 34 (a), and only marginally higher at the door location, as shown in Figure 34 (c), with values of 6.9 m/s versus 6.7 m/s, for the baseline and 214-static non-compliant model, respectively.
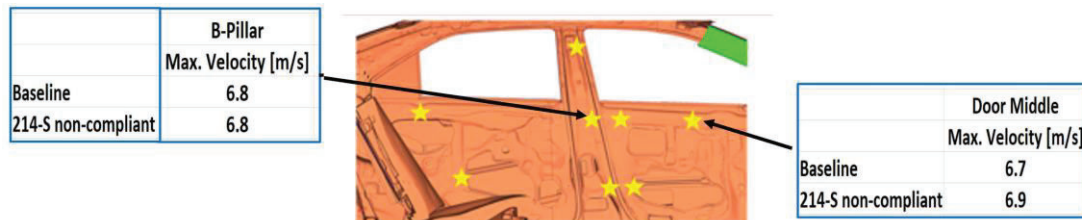
Figure 34. SUV accelerometer data - baseline versus 214-static non-compliant (a) B-pillar velocity; (b) relevant locations; (c) door velocity.

The analyses indicated that accelerometer data from the dynamic MDB configuration is not adequate to serve as a surrogate metric for the static test, due to the different load paths engaged during the FMVSS No. 214-MDB and static door crush tests. In addition, it was found that SUV-type vehicles with a relatively high rocker location and seating position, have a relatively low barrier to vehicle impact location. This geometric characteristic can produce higher deformations and velocities at the lower part of the vehicle for different structural designs, while deformation and velocities at the middle of the B-pillar and upper door, which are relevant for most occupant metrics, are the same or even lower for a baseline vehicle compared to a FMVSS No. 214 static non-compliant vehicle, as shown in Figure 34 (a) and Figure 34 (c).

It was concluded that accelerometer-based velocity time history data from the FMVSS No. 214-MDB dynamic test condition is not adequate to be used as a surrogate for the quasi-static minimum door crush resistance force requirements.

Metrics based on vehicle and barrier deformation

Vehicle and barrier deformation measurements, including residual MDB honeycomb crush, the IIHS side impact structural criteria, based on B-pillar intrusion and remaining occupant compartment space, and exterior crush measurements available from FMVSS No. 214-MDB and pole tests, as shown in Figure 35, have been evaluated. It was examined if they can indicate door crush resistance forces, as defined in the FMVSS No. 214-static requirement.

The MDB's honeycomb face has well-defined force-deformation characteristics. Digitizing the MDB barrier surface pre- and post-crash, allows to calculate the deformation at relevant areas, for example where the door is being impacted. From the residual deformation, the resulting force can be calculated.
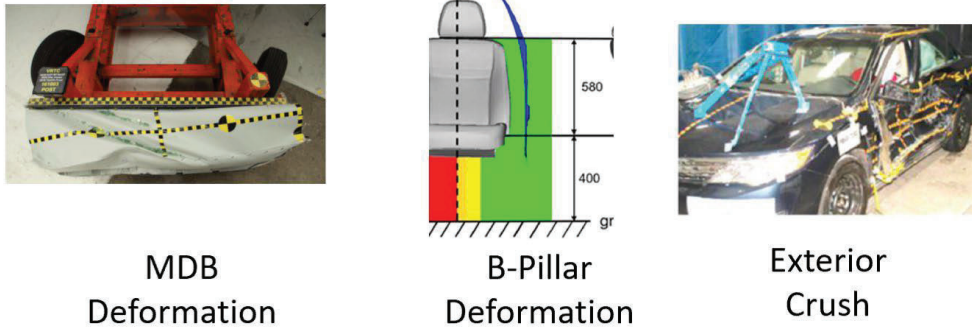
Figure 35. Deformation-based metrics (a) MDB deformation; (b) IIHS structural criteria; (c) exterior vehicle crush.

Due to the different load paths engaged for the respective FMVSS No. 214 configurations, no significant difference in honeycomb deformation was observed for the baseline model and the model that did not comply with FMVSS No. 214-static. The MDB configuration for the SUV vehicle category resulted in no significant barrier face deformation for the area impacting the door, since the main load was transferred through the barrier bumper and vehicle rocker area, as shown in Figure 1 (a).

The evaluation of test and simulation results indicated that deformation-based measurements from the FMVSS No. 214 dynamic MDB and pole test conditions have significant limitations to indicate minimum door crush resistance force metrics, as defined in the static test.

Metrics based on rigid pole load cell data

Locations and contact times between pole and vehicle, as well as between occupant and vehicle, were studied in detail, for the FMVSS No. 214-pole impact test, as shown in Figure 36. After initial contact of the moving vehicle with the stationary rigid pole at 0 ms, the outer door is deformed after about 10 ms and the sill area starts to be impacted and deformed. After 20 ms air bags are mostly inflated, depending on the sensors used; the door has been significantly crushed, and the sill area is partially deformed at this time. After 40 ms initial contact of the pole with the roof area can occur, depending on the design of a vehicle; air bags have used most of the available package space between occupant and interior to mitigate the impact, and maximum occupant loads start to develop. After 60 ms, the front door and rocker have been significantly deformed at the impact location and the roof area shows deformation to some extent.
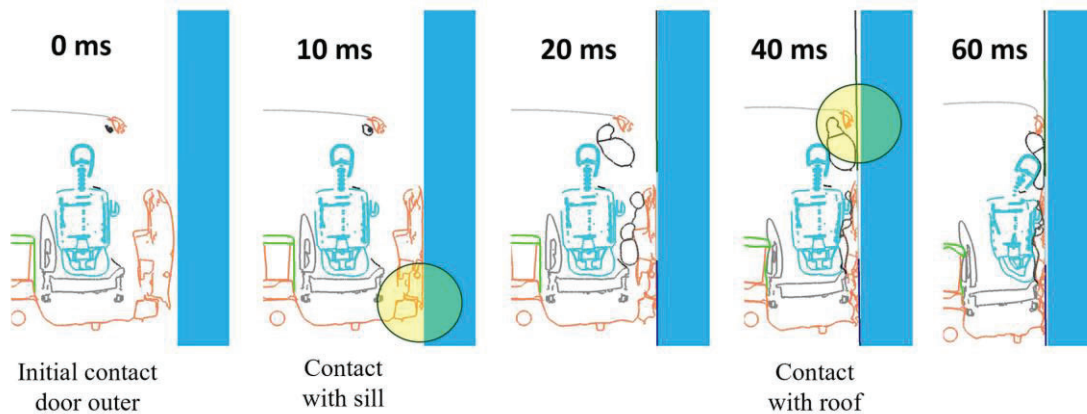
Figure 36. Sequence of FMVSS No. 214-pole characteristic crash events using a cross-section view.

These characteristic crash events can clearly be seen in respective load cell data, recorded at different heights of the rigid pole. Figure 37 shows an example of a sedan pole impact with force time-history data recorded at the sill, door, and roof impact areas. The earliest onset can be observed at the door, due to the geometry of the vehicle and the initial contact with the pole in this area. After about 10 ms, a sudden increase in force in the vehicle rocker area can be observed and engagement of the roof area load path can clearly be identified after about 35 ms.
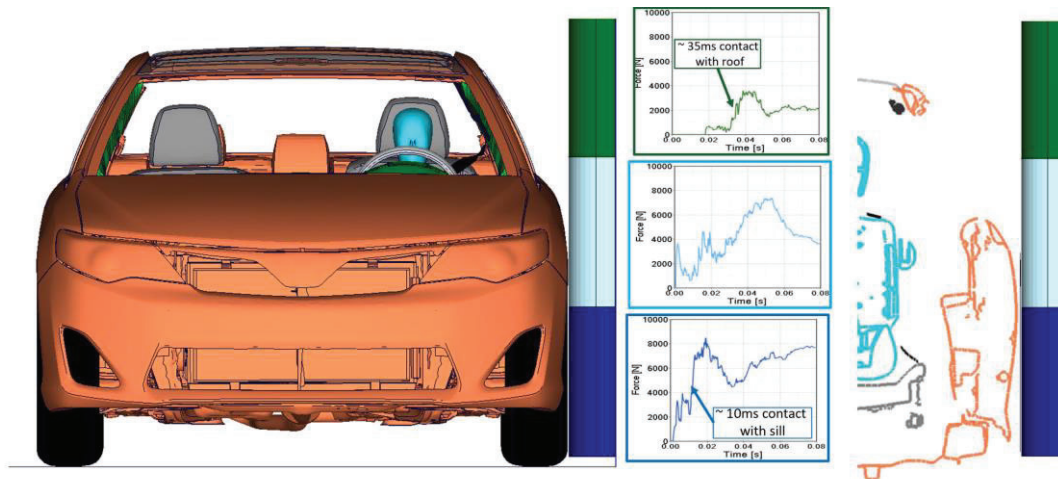
Figure 37. Pole impact force time history data for rocker, door, and roof area.

Existing and recorded pole load cell data from full-scale tests and conducted simulations were carefully studied to determine if the dynamic measurements can be used as surrogates for the static test. Figure 38 (a) shows the comparison of the force versus displacement characteristics in the static door crush resistance condition for the Nissan Rogue baseline model and the model that did not comply with the FMVSS No. 214-static requirement. The distinct difference of the resistance force levels for the baseline model, shown in blue, and the model that did not comply with the static requirement, shown in red, can clearly be noticed. Load cell data from the rigid pole instrumentation located next to the front door, as illustrated in Figure 38 (b), was used in combination with vehicle displacement data, to generate a force versus displacement graph, similar to the one used for the static requirement. Figure 38 (c) shows the force versus displacement characteristics for the SUV baseline model and the model that did not comply with the static requirement in the pole impact in blue and red, respectively.
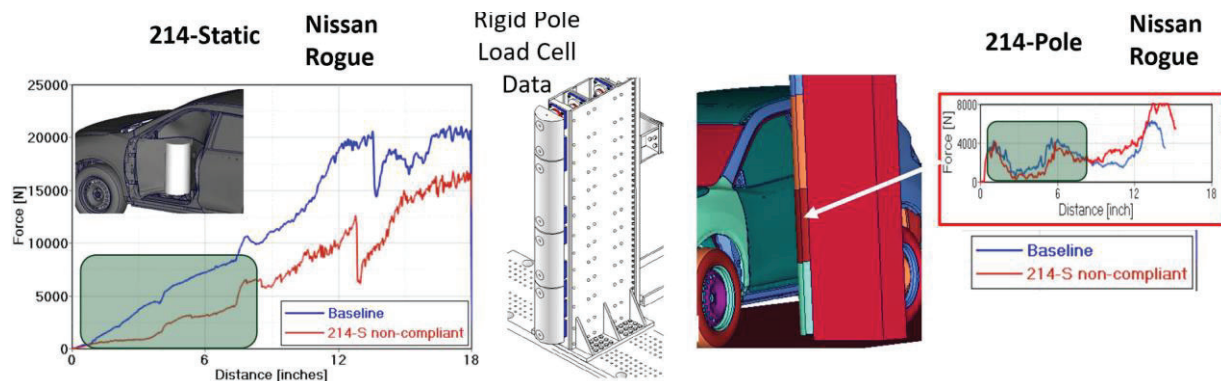
Figure 38. Nissan Rogue baseline versus FMVSS No. 214-static non-compliant model (a) comparison of static door crush resistance force; (b) load cell locations; (c) comparison of force versus deformation at the door location.

From Figure 38 (c), higher maximum exterior crush for the 214-static non-compliant model can be observed. Higher forces can be seen for the baseline model for the first 8 inches of vehicle displacement. This is in qualitative agreement with the force versus displacement characteristics observed in the static door crush condition. Vehicle deformation at the sill and roof affect the loads induced into the door in the pole configuration, in contrast to the static door crush test, where the rigid cylinder intrudes into the door exclusively. Therefore, force versus displacement characteristics for static cylinder and dynamic pole tests, did not show the same qualitative trend after about 8 inches of crush for the baseline model and the FMVSS No. 214-static non-compliant model.

In conclusion, the evaluation of rigid pole load cell data measurements showed that they can qualitatively indicate front door crush resistance to some extent, similar to the FMVSS No. 214-static test condition, in the initial deformation phase, but has limitations for higher intrusions.

Surrogate metrics limitations

As outlined in the previous paragraphs, there are significant limitations of using performance measurements from the dynamic FMVSS No. 214-MDB and pole configurations as a surrogate for the static door crush requirement:

- The most obvious limitation is the lower maximum exterior crush, which was about 8.7 inches and 13.7 inches for recent MDB and pole impact full-scale tests, respectively. In contrast, the static door crush test requires front and rear door crush resistance force to be evaluated up to 18 inches of deformation.
- Accelerometer based velocity time history data, which can be a good indicator for MDB side impact performance of a vehicle with respect to occupant metrics, has significant limitations. Different load paths, relevant for the static and dynamic tests, especially for sedan-type vehicles, and characteristic deformation patterns with higher seating positions for SUV-type vehicles, make this dynamic measure not adequate to be used as a surrogate for the quasistatic test.
- Smaller maximum exterior crush was observed for the dynamic FMVSS No. 214-MDB and pole conditions compared to the static requirement. Limited engagement and deformation of upper honeycomb face, especially for "higher" SUV-type vehicles where the MDB bumper engages with the rocker also presented significant limitations. The exterior crush, MDB deformation, and IIHS structural criteria were therefore found not adequate to serve as surrogate measurements for the static test.
- The evaluation of rigid pole load cell data measurements showed that they can qualitatively indicate front door crush resistance to some extent, similar to the FMVSS No. 214-static test condition, in the initial deformation phase, but has limitations for higher intrusions.

Additional limitations, to the ones outlined for the front door, exist for defining a performance metric based on results from the dynamic FMVSS No. 214-MDB and pole configurations, that can be used as surrogate for the static door crush test at the rear door. Pole impacts are only performed at the front door and, therefore, do not provide any data that could indicate the door crush resistance of the rear doors. Similarly, the MDB is positioned relative to the front axis of a vehicle and typically impacts the B-pillar, the entire front door, but only part of the rear door, depending on the wheelbase and length of a vehicle.

CONCLUSION

A validated FE model representing the sedan vehicle category and a validated FE model representing the SUV vehicle type were used to conduct simulation studies that investigated the mutual effect of non-compliance for each of the three FMVSS No. 214 side impact configurations, the quasi-static door crush test, the MDB barrier impact, and the pole configuration.

A validated FE model of a 2015 Toyota Camry was used to conduct the sedan FMVSS No. 214 simulation study. The baseline FE model was modified in such a way, that it resulted in non-compliance with respect to the FMVSS No. 214-static test configuration, based on minimum door crush resistance force requirements. Similarly, FE models were generated, that resulted in non-compliance for the dynamic FMVSS No. 214-MDB and FMVSS No. 214-pole impact configurations, which are based on ATD metrics.

It was found that structural modifications that resulted in non-compliance for one of the FMVSS No. 214 impact configurations did not result in non-compliance for the other two configurations, due to different relevant load paths.

A FE model of a 2020 Nissan Rogue SUV was developed applying an established reverse engineering process and used to conduct a similar simulation study, as for the Toyota Camry sedan. It was found that structural modifications that resulted in non-compliance for one of the load cases did not result in non-compliance for the other two configurations, except for 214-MDB non-compliance, which also resulted in 214-pole non-compliance.

Different metrics from the FMVSS No. 214-MDB and pole side impact configurations were evaluated to determine the feasibility of using dynamic performance measurements as a surrogate for the FMVSS No. 214 static door crush test. It was found that there are significant limitations, because of the different main load paths relevant for the dynamic and static side impact tests. Dynamic rigid pole load cell data showed the highest potential of indicating initial front door crush resistance.

ACKNOWLEDGEMENT

PEER REVIEW PAPER

This paper has been peer‑reviewed and published in a special edition of Traffic Injury Prevention 24(S1), by Taylor & Francis Group. The complete paper will be available on the Traffic Injury Prevention website soon. To access ESV Peer-reviewed papers click the link below
https://www.tandfonline.com/toc/gcpi20/24/sup1?nav=tocList

FACTORS OF SEVERE INJURIES ASSOCIATED WITH SIDE POLE COLLISIONS BASED ON FIELD VEHICLE COLLISION INVESTIGATION

Yeon IL Choo
Oh Hyun Kim
Kang Hyun Lee
Joon Seok Kong
Center for Automotive Medicine Science Institute, Yonsei University, Wonju College of Medicine
Republic of Korea

Gil Won Kang
Graduate School of Biomedical Convergence, Chungbuk National University, College of Medicine
Republic of Korea

Sang Chul Kim
Department of Emergency Medicine, Chungbuk National University, College of Medicine
Republic of Korea

Kwang Soo Shin
Graduate School of Healthcare Management, The Catholic University of Korea
Republic of Korea

Paper Number 23-0130

ABSTRACT

Side pole collision is the most devastating road traffic injury (RTI) that causes death or severe injuries among side collisions. Since pole-type materials have a relatively narrow width and fixed rigidity, side pole collisions cause severe deformation and consequent intrusion resulting in direct contact with the occupants. This study aimed to investigate the risk factors that contributes to a severe injury of motor vehicle occupants (MVOs) in side pole collisions.

This study used the Korea In-Depth Accident Study (KIDAS) database collected from 2011 to April 2020. Among the total data, we analyzed 392 patients who were engaged in side collisions by excluding multiple collisions and rollovers. The collision type was classified into pole and non-pole (i.e., vehicle-to-rigid wall) collisions within a single collision. Moreover, we classified the collision severity according to the amount of crush extent (CE) zones.

In this study, the incidence of non-pole collisions (n=362, 92.35%) was nearly 12 times higher than pole-related collisions (n=30, 7.65%). Factors affecting severe injuries showed statistical significance in the collision object (p<0.001), seat location (p=0.001), and CE zone (p<0.001). However, passive safety devices, such as seatbelts and airbags, showed no significance. In the case of side collision objects, there were statistical differences between the chest (p=0.004), pelvis, and extremities (p=0.016) between pole and non-pole side collisions. Particularly, The highest risk of severe injury had dramatically increased since the amount of CE zones was higher (odds ratio OR, 9.604; confidence interval, 3.739–24.672). MVOs colliding with pole structural materials had the risk of severe injury (ISS16+) in side collisions (OR, 5.285; 95% CI, 1.358–20.571). Compared with the far-side occupant, the near-side occupant had increased risk of severe injury (OR, 3.123; 95% CI, 1.438–6.783).

In this study, factors affecting severe injuries in side collisions were identified as the collision object, seat location, and crush extent. In frontal and rear-end collisions, it is necessary to seek weakness of crashworthiness caused by the lack of structural performance (e.g., bumpers, engine room, truck leads) to protect occupants from collision capacity in side pole collisions.

In conclusion, an increase in vehicular extent also leads to a risk of intrusion, resulting in a severe injury to near side occupants. In contrast with frontal collisions, both side parts of the vehicle have a relatively low range of capacity to absorb the collision. It is difficult to evaluate severe injury of occupants after a collision at the scene. Proper evaluation on scene can improve the occupant's prognosis.

INTRODUCTION

According to the Fatality Analysis Reporting System (FARS) of the National Highway Traffic Safety Administration (NHTSA), 121,844 vehicle occupant deaths occurred in collisions over the past five years. There were 23,647 vehicle occupant deaths in 2019. Among them, 11,048 deaths were caused by in single collisions, and 5,890 by collisions with fixed objects. Side pole collisions caused 1,070 deaths, accounting for 18.17% of the total deaths. Moreover, 868 occupants died from side pole collisions. The fatality rate was the highest at 81.12% in fixed object collisions. These statistics suggest that side pole collisions can result in severe injury to the occupant [1].

Figure 1. Side pole collision and pole-type object.

Side collision has a lower rate than frontal collision but causes severe injury to occupants [2,3]. In most side collisions, near-side occupants had highest rate (53.3%) and more MAIS3+ compared to far-side occupants [4,5,6,7,8,9,10]. As such, in side pole collisions, occupants at the side parts of the vehicle had a high risk of severe injury.

Recognizing that the side parts of the vehicle can cause severe injury to occupant unlike front parts, analysis and research on the safety standards for side collisions in the United States and Europe have been conducted since the 1980s [11]. However, the Insurance Institute for Highway Safety (IIHS) conducted vehicle safety evaluations through side collision tests every year. Even though vehicles have secured five-star safety rating in evaluation results, severe side collisions continue to be reported [12].

Therefore, it is necessary for side pole collisions to be reduced and vehicle stiffness to be increased for occupant safety. This study aimed to analyze the factors affecting severe injury between side pole collisions.

METHODS

Data collection

This study used the Korean In-Depth Accident Study (KIDAS) database, which was constructed for patients who visited five emergency medical trauma centers. Data of a total of 3,899 patients between January 2011 and April 2020 were analyzed. Figure 2 presents a flowchart of the selection of patients who had side pole collision (n=30) and non-pole collision (n=362).

Data selection criteria

Figure 3 shows the Collision Deformation Classification (CDC) code with seven columns (text and number) of vehicle collision deformation by the Society of Automotive Engineers (SAE International). In this study, side collisions were defined using the codes in Table 1.
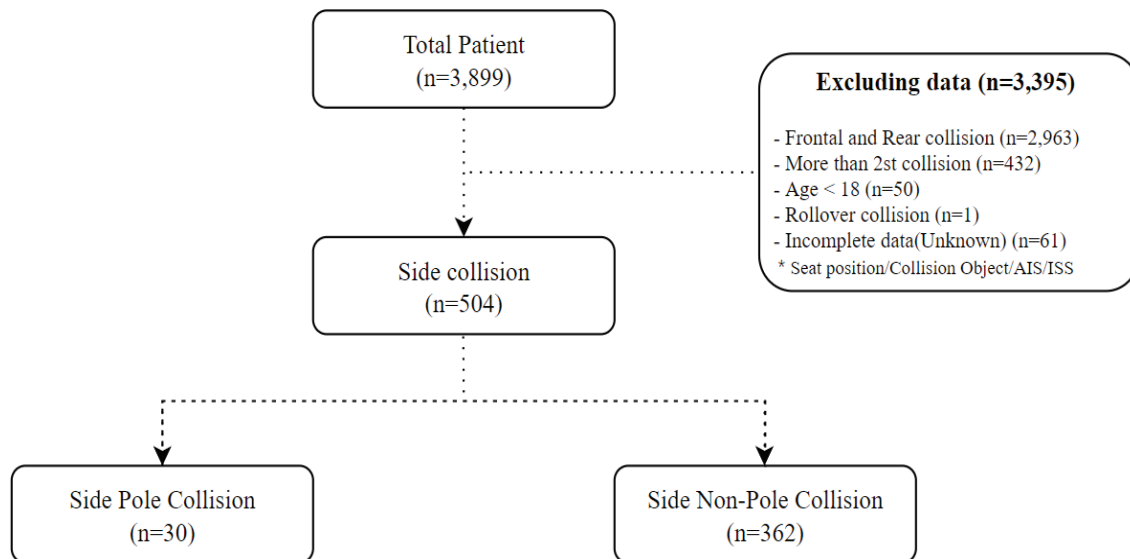
Figure 2. Data selection flowchart.
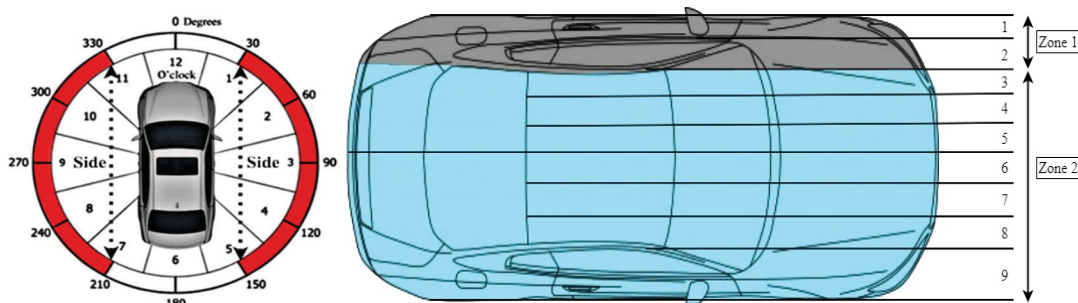
Figure 3. Collision Deformation Classification code.

Table 1.
Selection Collision Deformation Classification Code for Data Analysis

Column	Contents	Used code
1, 2	Principal direction of force	1–5, 7–11
3	Vehicle deformation location	L, R
4	Specific longitudinal or lateral area	F, P, B, Y, Z, D
5	Specific vertical or lateral area	L, M, G, E, H, A
6	Type of damage distribution	W, E, N, S
7	Vehicle crush extents	1–9

1) The direction of collision (principal direction of force [PDOF]) was at 1–5 o'clock and 7–11 o'clock of the CDC code in columns 1 and 2, and vehicle collision deformation location in column 3 was Left (L), Right (R). Data other than the codes were excluded.

2) The single side collision was classified as primary, excluding more than multiple collisions. This study analyzed the severe injuries of adult patients. Age < 18 years and rollover code (O) of the CDC code column 6 were excluded.

3) For the severity of collision, the crush extent of the CDC code in column 7 was used. Side collision severity was indicated by vehicle collision deformation Zone 1 for scores ranging from 1 to 2 and Zone 2 for scores ranging from 3 to 9.

Table 2.
Pole vs Non-pole

Pole	Non-pole
Light pole	Motorcycle
	Sedan
	SUV*
	Light truck
Telegraph pole	Van
	Bus
	Middle truck
	Heavy truck
	Tractor with trailer
Tree	Guardrail
	Train
	Median strip
	Wall
	Others

SUV, sports utility vehicle

Table 2 presents the definitions of collision objects. Collision objects in the KIDAS database coding book version 3.0 defined light poles, telephone poles, and trees as pole objects and all other collision objects as non-pole objects.

Table 3.
Selection Variables for Data Analysis

Variable	Details	Type
Age	≥18 years	Numerical
Sex	Male, female	Categorical
Vehicle type	Passenger car, sports utility vehicle, light truck, van	Categorical
Collision object	Pole, non-pole	Categorical
Collision direction	Left, right	Categorical
Seat location	Near side, far side	Categorical
Crush extent	Zone 1 (extent, 1–2), zone 2 (extent, 3–9)	Categorical
Seatbelt fastened	Fastened, unfastened	Categorical
Airbag deployment (Front, side, curtain, knee)	Deployed, undeployed	Categorical
ISS	>16, ≤16	Categorical
AIS	>3, ≤3	Categorical

Risk factors affecting severe injuries of the patient were analyzed using the variables presented in Table 3. In Figure 4, occupants close to the collision object were defined as near side occupants and occupants far from the collision object were defined far side occupants.

The Abbreviated Injury Scale (AIS) code devised by the Association for the Advancement of Automotive Medicine was used in the classification of injury severity. Scores were recorded in eight body regions from 1 to 6 according to the injury severity, and the highest score was defined using the Maximum Abbreviated Injury Scale (MAIS). The Injury Severity Score (ISS) was the sum of squares of more than three AIS scores by the range of 1–75. In this study, severe injury was defined as AIS3+ and ISS16+.
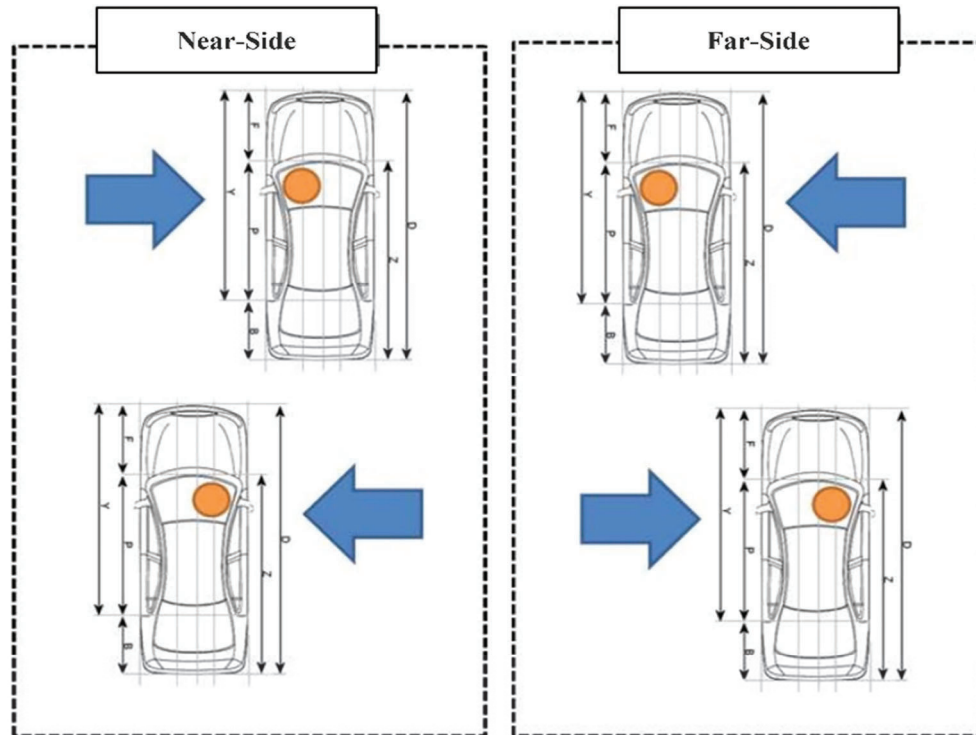
Figure 4. Near side and far side.

Statistics analysis

Dependent and independent variables in each group were analyzed by frequencies and percentages using the chi-square test and Fisher's exact test. The t-test analyzed average and standard deviation values for continuous variables. For AIS and ISS scores that did not follow a normal distribution, the median and quartile were obtained using the Mann–Whitney U test or Kruskal–Wallis H test. Airbag deployment variables in < 30 patients were analyzed using the nonparametric test. This study evaluated injury severity risk factors of patients with pole collisions using the logistic regression analysis. Statistical significance was defined as a P-value <0.05. SPSS (version 26.0, IBM Inc, Chicago, USA) was used in the analysis.

RESULTS

Table 4 presents the general characteristics of side collisions according to occupant severity. There are compared between two groups. The incidence of severe injury (17.5%) was higher in pole collisions (p<0.001). Based on vehicle seat location, near side occupants accounted for 72.1% of the severe group, which was higher than that in far side occupants (p=0.001). Based on vehicle collision deformation, the rate of Zone 2 in the severe group was 83.8%, which was higher than that of Zone 1 (p<0.001).

Table 4.

General Characteristics of Severe Injury Occupant in Side Collision

	ISS<16		ISS≥16		Total		P-value
	N=324	%	N=68	%	N=392	%	
Sex							
Male	193	59.6	48	70.6	241	61.5	0.090
Female	131	40.4	20	29.4	151	38.5	
Age (mean±S.D.)*	46.73±16.33		47.71±17.69		46.9±16.56		0.907
Vehicle type							
Sedan	206	63.6	40	58.8	246	62.8	
SUV**	62	19.1	11	16.2	73	18.6	0.325
Van	37	11.4	9	13.2	46	11.7	
Light truck	19	5.9	8	11.8	27	6.9	
Collision direction							
Left	168	51.9	43	63.2	211	53.8	0.087
Right	156	48.1	25	26.8	181	46.2	
Collision object							
Pole	15	4.6	15	22.1	30	7.7	0.000
Non-pole	309	95.4	53	77.9	362	92.3	
Seat location							
Near side	164	50.6	49	72.1	213	54.3	0.001
Far side	160	49.4	19	27.9	179	45.7	
Crush extent							
Zone 1	191	59.0	11	16.2	202	51.5	0.000
Zone 2	133	41.0	57	83.8	190	48.5	
Seatbelt							
Fastened	223	71.7	40	60.6	263	69.8	0.075
Unfastened	88	28.3	26	39.4	114	30.2	
Airbag							
Deployment	45	18.7	5	10.4	50	17.3	0.167
Undeployment	196	81.3	43	89.6	239	82.7	

*Mean±standard deviation (S.D.), **SUV, sport utility vehicle*

Table 5 shows a comparison of the severity of each body part according to the impact object. The incidence of chest injury AIS3+ was higher in the pole group (40%) compared to that in the non-pole group (18.2%) (p=0.004). Moreover, the incidence of pelvis and extremities AIS3+ was higher in the pole group (13.3%) than that in the non-pole group (2.8%) (p=0.016). Between the two groups, the median and quartile of MAIS and ISS in the pole group were higher than those in the non-pole group (p=0.001)..

Table 5.

Injury Severity for Body Regions According to Collision Object

	Pole		Non-pole		Total		P-value
	N=30	%	N=362	%	N=392	%	
Head and neck							
AIS < 3*	23	76.7	316	87.3	339	86.5	0.158
AIS ≥ 3	7	23.3	46	12.7	53	13.5	
Face							
AIS < 3	30	100.0	359	99.2	389	99.2	1.000
AIS ≥ 3	0	0.0	3	0.8	3	0.8	
Thorax							
AIS < 3	18	60.0	296	81.8	314	80.1	0.004
AIS ≥ 3	12	40.0	66	18.2	78	19.9	
Abdomen							
AIS < 3	27	90.0	351	97.0	378	96.4	0.083
AIS ≥ 3	3	10.0	11	3.0	14	3.6	
Pelvis and extremities							
AIS < 3	26	86.7	352	97.2	378	96.4	0.016
AIS ≥ 3	4	13.3	10	2.8	14	3.6	
MAIS**, median [IQR]***	3 (2-4)		2 (1-3)		2 (1-3)		0.001
ISS, median [IQR]	15 (5-34.25)		4.5 (2-10)		5 (2-11)		0.001

*AIS, Abbreviated Injury Scale; **MAIS, Maximum Abbreviated Injury Scale; ***IQR, interquartile range

Table 6 presents a logistic regression analysis for risk factors of severe injury in side collision. There was a statistical significance in the collision object, seat location, and vehicle damage severity. In crush extents, Zone 2 risk was 9.545 times higher (95% CI, 3.739–24.672; p=0.001) than Zone 1 risk. In the collision object, pole collision showed a 5.285 times (95% CI, 1.358–20.571; p=0.016) higher risk than non-pole collision. Near side occupants had a higher risk (95% CI, 1.438–6.783; p=0.004) than far side occupants by 3.123 times.

Table 6.

Logistic Regression Analysis for Risk Factors of Severe Injury in Side Collision

Variables	OR	95% CI	P-Value
Crush extent			
Zone 1	Reference		
Zone 2	9.604	3.739–24.672	0.001
Collision object			
Non-pole	Reference		
Pole	5.285	1.358–20.571	0.016
Seat location			
Far side	Reference		
Near side	3.123	1.438–6.783	0.004

*Adjusted for sex, seatbelt use, airbag deployment, and vehicle type. CI, confidence interval; OR, odds ratio.

DISCUSSION

This study aimed to identify the factors affecting severe injury of occupants in side pole collisions. It is difficult to evaluate severe injury of ccupants after a collision at the scene. Proper evaluation on scene can improve the occupant's prognosis. This study suggests that side ollision, near side location, pole object, increased vehicle collision deformation increases the risk of severe injury.

As vehicle deformation increases, occupant injury increases. In the results of this study, as the vehicle deformation increased in a side pole collision, the rate of injury increased ($p<0.001$), and the risk increased 9.6 times in vehicle deformation intrusion ($p<0.005$). In a previous study, there was no difference in occupant injuries in extent 1–2 in a side collision, but injuries increased in extent 3+ [13]. In another study in which a vehicle was equipped with a dummy, vehicle deformation intrusion was shown by direct collision with the dummy in the side pole collision test [3]. The more the vehicle collision deformation increase, the more interior and direct the collision with the occupants.

In a previous study, the risk of severe damage was 2.26 times higher in a side collision with a pole object than in a vehicle-to-vehicle collision [3]. In this study, the risk of side pole collision was 5.29 times higher than that of side non-pole collision. Matthew et. al. reported that 59% of chest injuries and 33% of pelvic injuries occurred in side collisions with narrow objects around the road [12]. In this study, the comparison of severe injuries by body regions according to the collision object (40% of the chest and 13.3% of the pelvis and extremities in the severe group) showed statistical significance ($p<0.005$). Therefore, a side collision with a pole object increases the risk of severe injury to the occupant.

Therefore, there is a high risk of severe injury to patients after a side pole collision. Even in vehicles with fivestar safety ratings, since the effectiveness of the safety device for preventing occupant injury is insufficient, structural design improvement for vehicular intrusion should be considered for side pole collisions. Moreover, paramedics dispatched to on scene must check on the patient's status and improve the rognosis of the patient by speedy transport.

CONCLUSIONS

In this study, we analyzed the factors affecting severe injuries of occupants in side collisions based on real-world data. It has been confirmed that side collisions caused by pole objects have a higher rate of severe injury to the occupant than a collision with a non-pole object. Near side occupants had an increased risk of severe injury than far-side occupants. The intrusion distance of vehicle collision deformation increases during a side collision with a pole object, a major factor affecting severe injuries. Unlike front collision, side collisions seems to cause direct collision to the vehicle with the occupants as the vehicle collision deformation is intruded because the collision is concentrated when colliding with the pole object. Therefore, it is necessary to supplement the vehicle design to respond to side pole collision by reflecting these characteristics. This study is expected to be used as basic research to predict risk factors of severe injury on scene.

ACKNOWLEDGEMENT

REFERENCES

[1] Fatality Analysis Reporting System (FARS) Encyclopedia, 2019. https://www-fars.nhtsa.dot.gov/Main/index.aspx

[2] Varat, M.S. and S.E. Husher. 1999. "Vehicle Crash Severity Assessment in Lateral Pole Impacts." SAE Transactions, 302-324.

[3] Pintar, F.A., Maiman, D.J., and N. Yoganandan. 2007. "Injury Patterns in Side Pole Crashes." In Annual Proceedings/Association for the Advancement of Automotive Medicine (vol. 51, p. 419). Association for the Advancement of Automotive Medicine.

[4] Rouhana, S.W. and M.E. Foster. 1985. "Lateral Impact – An Analysis of the Statistics in the NCSS." SAE

Transactions, 220-239.

[5] Håland, Y., Lövsund, P., and A. Nygren. 1993. "Life-Threatening and Disabling Injuries in Car-to-Car Side Impacts – Implications for Development of Protective Systems." Accident Analysis & Prevention, 25(2), 199-205.

[6] Farmer, C.M., Braver, E.R., and E.L. Mitter. 1997. "Two-Vehicle Side Impact Crashes: The Relationship of Vehicle and Crash Characteristics to Injury Severity." Accident Analysis & Prevention, 29(3), 399-406.

[7] Zaouk, A.K., Eigen, A.M., and K.H. Digges. 2001. "Occupant Injury Patterns in Side Crashes" (No. 2001-01-0723). SAE Technical Paper.

[8] Bedard, M., Guyatt, G.H., Stones, M.J., and J.P. Hirdes. 2002. "The Independent Contribution of Driver, Crash, and Vehicle Characteristics to Driver Fatalities." Accident Analysis & Prevention, 34(6), 717-727.

[9] Howard, A., Rothman, L., McKeag, A.M., Pazmino-Canizares, J., Monk, B., Comeau, J. L., and German. 2004. "Children in Side-Impact Motor Vehicle Crashes: Seating Positions and Injury Mechanisms." Journal of Trauma and Acute Care Surgery, 56(6), 1276-1285.

[10] Viano, D.C. and C.S. Parenteau. 2010. "Severe Injury to Near- and Far-Seated Occupants in Side Impacts by Crash Severity and Belt Use." Traffic injury prevention, 11(1), 69-78.

[11] Shin, J. and G.J. Yong. 2014. Safety Evaluation of Korean New Car Assessment Program – Side Impact. Journal of Auto-Vehicle Safety Association, 6(2), 12–17.

[12] Brumbelow, M.L., Mueller, B.C., and R.A. Arbelaez. 2015. "Occurrence of Serious Injury in Real-World Side Impacts of Vehicles with Good Side-Impact Protection Ratings." Traffic Injury Prevention, 16(sup1), S125-S132.

[13] Gabler, H.C., Digges, K., Fildes, B.N., and L. Sparke. 2005. "Side Impact Injury Risk for Belted Far Side Passenger Vehicle Occupants." SAE Transactions, 34-42.

LATERAL IMPACT CRASH TESTS FOR POWERED TWO-WHEELERS

Simona Roka, Genís Mensa, Victor Garcia
IDIADA Automotive Technology
Spain

Niccolò Baldanzini
UNIFI
Italy

Marco Pieve
PIAGGIO
Italy

Simone Di Piazza
DUCATI
Italy

Paper Number 23-0259

ABSTRACT

Protection of the Powered Two-Wheelers (PTW) is a major concern due to the increase of this mode of transportation in the accident statistics during the last years. In fact, nowadays, more than 12 riders die on European roads every day and more than 100 are severely injured. In that scenario, IDIADA has promoted and coordinated the European project PIONEERS within the H2020 EU funding programme. This project aimed to reduce the number of PTW fatalities and severely injured by increasing the safety performance, comfort, and usage rate of Personal Protective Equipment (PPE) and the development of new on-board vehicle safety devices. To be able to evaluate the effectiveness of the on-board vehicle safety devices, a lateral testing protocol has been developed considering specifications of the sensor mounting, fixing of the PTW into the test rig, etc. to ensure the repetitiveness of the tests. Four lateral barrier (AE-MDB Euro NCAP) impact tests with two different on-board systems have been performed within the scope of the PIONEERS project according to the impact protocol defined. A Motorcycle Anthropomorphic Test Device (MATD) has been attached to the upper part of a standard Hybrid III dummy from IDIADA to perform the crash tests. Simulations have been performed by UNIFI and compared with the physical tests performed in the laboratory. Results show significant differences between the use of lateral airbag and safety leg cover. The differences are observed not only in the biomechanical values of the MATD but also in the kinematics of the PTW and dummy and in the final relative position of both. By developing new test protocols, more realistic and robust test methodologies will provide better physical data for PTW manufacturers, as well as for on-board protective equipment OEMs (Original Equipment Manufacturers) and PPE suppliers. The data from the tests can be considered as a baseline for further development of the injury assessment for PTWs and it's believed that this data will help to develop more sophisticated testing devices. This paper covers the preparation of testing protocols and execution of PTW lateral safety testing activities performed in IDIADA.

INTRODUCTION

Today, Powered Two Wheelers (PTW) are regarded as one of the most dangerous modes of road transport. PTW accidents have suffered a very low reduction in fatalities in the recent years. In the EU, between 2006-2015, accidents decreased in general by 57%, while in the recent years, PTW accidents just decreased by 28%. PTW accidents made up 18% of road accident fatalities in 2015 in the EU.

This project aims to reduce the number of PTW fatalities and severely injured by increasing the safety performance, comfort and usage rate of Personal Protective Equipment (PPE) and the development of new on-board safety devices. As part of its role, IDIADA designed new full-scale crash test protocols for lateral motorcyclist safety.

Results from previous study done in PIONEERS project D1.1 revealed that the most common AS (Accident Scenario) in this context are AS3 and AS6. AS3 refers to accidents between an L3 (A two-wheeled vehicle with an engine cylinder capacity in the case of a thermic engine exceeding 50 cm3) vehicle and a passenger car/taxi, whilst AS6 refers to single L3 vehicle accidents. Moreover, the most frequently reported first collision contact point is the centre front for the PTW (28.9% of all cases), and the left side for the Opponent Vehicle (OV) (21.9% of all cases). In fact, urban two-participant crashes at intersections are a prevalent cause of serious injuries to PTW riders in all countries. Therefore, in this study a lateral left-side test between an L3 vehicle and a car has been considered to represent AS3.[1]

TEST DESCRIPTION

As outlined in D1.1, in AS3 cases, the PTW impact speed was often higher than the OV impact speed. L3 vehicles more frequently crashed with a speed ranging between 25-35 km/h and 45-60 km/h, while OVs more frequently crashed with a speed ranging between 10-25 km/h. In AS6 crashes, 60.2% of PTWs were between 40-80 km/h.

The most common demographics of PTW riders injured in crashes in Europe were young males (16-35 years old) with a height of 161-180 cm. Thus, a male dummy will be chosen to perform the two different crash tests in Task 3.5 of the PIONEERS project.

Regarding target injuries, the analysis from D1.1 highlighted four body regions: Thorax & Thoracic Spine (TTS), Head & Face (HF), Upper Extremities (UE), and Lower Extremities (LE). At least moderate injuries (AIS 2+) were most frequently found in the thorax (rib cage, lung, and haemothorax) and the brain. Also, abrasions of severity AIS 1 were most frequently found in the LE, followed by the UE.

Accident conditions were selected, including target accident scenarios and main injuries, with special attention to this accidentology data.

Two full-scale crash test protocols to validate the two different on-board systems developed have been defined. The selected test conditions were based on the most suitable impact configuration and have been validated with several simulations to ensure the desired dynamics and the requirements of repeatability and reproducibility.

Each of the tests consisted in two crashes (in total there were 4 crashes). Those were side impacts, trying to simulate as much as possible the most common AS3 accident scenario. The tests consisted in a side impact, using an AE-MDB barrier of 1400kg, crashing with an angle of 90º into the side of the motorcycles, a Ducati Multistrada and a Piaggio MP3. The barrier impacted at speeds of 30 km/h for the Ducati tests and at 15km/h for the Piaggio tests. Both motorcycles crashed at a speed of 30 km/h.[1]
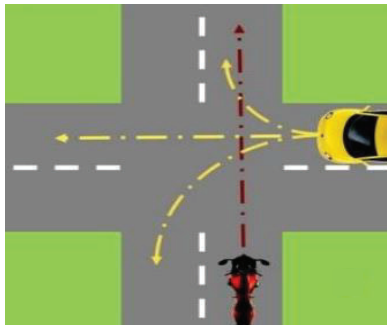

Figure 1. Representation of the AS3 that has been tested, from PIONEERS project D1.1

Test environment

These two crash modes were designed with the objective to validate two novel on-board safety systems that were developed in the PIONEERS project with the objective to reduce the severity of motorcycle rider leg injuries. These safety systems were, namely, a lateral airbag system from DUCATI and a safety leg cover designed by PIAGGIO. By developing new test protocols, the PIONEERS consortium hoped to achieve a more realistic and robust test methodology providing better physical data for PTW OEMs (Original Equipment Manufacturers), as well as for on-board protective equipment and PPE suppliers.

As a result of the work conducted in PIONEERS T3.3, the two side impact test protocols shown below in Figures 2 and 3, were defined. Figure 2 represents the crash configuration for the test to evaluate the effectiveness of the Lateral airbags, whilst Figure 3 shows the test protocol defined to assess the PIAGGIO safety leg cover. In both cases, the tests were designed to use a specialized Motorcyclist dummy (MATD) as motorcycle rider or, alternatively, a combination of a Hybrid III 50th percentile upper body and a MATD lower body.

This paper explains the details of the test protocol definition for the two studied lateral impact cases in the framework of PIONEERS. It is important to note that, the two crash configurations indicated above were also chosen considering the design parameters of each of the on-board safety systems and motorbikes.

The Piaggio's range of speed is considered to be more urban (lower speed) and therefore a suitable on-board safety system, lower leg cover, was chosen. On the contrary, DUCATI motorbike is considered to be used on highways or with elevated speed and so an adequate on-board safety system such as lateral airbag was used.
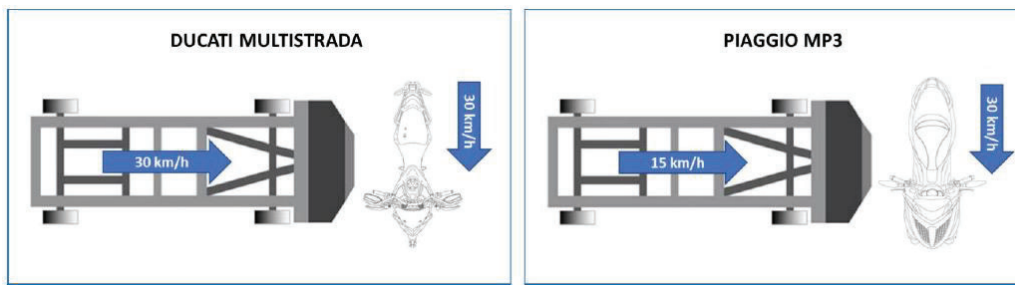
Figures 2 (left) and 3 (right); 1: Ducati test protocol; 2: Piaggio test protocol.

Four full-vehicle crash tests were conducted at IDIADA. Two tests were performed using a DUCATI Multistrada and the other two tests were performed using a PIAGGIO MP3 500.

For each vehicle model, one crash test was conducted where no countermeasure was included (baseline) and the other crash test did include an on-board safety system. The on-board safety systems considered for this project were, respectively, the DUCATI on-board side airbags and the PIAGGIO safety leg cover. The overall test matrix used in this test series is shown in Table 1.

| Test | Test number | | Vehicle | | Test date | Test type | Barrier | | |
	IDIADA	Customer	Brand	Set-up			Trolley	Def. element	Serial no.
1	A210409COEC	WP3.5_1	Ducati	W/ AIRBAG	1/28/2021		Lateral	Cellbond AE-MDB	208318
2	A210410COEC	WP3.5_2	Ducati	W/O AIRBAG	1/28/2021	Side barrier	Europe	Side impact barrier	208429
3	A210415COEC	WP3.5_3	Piaggio	W/O safety leg cover	1/29/2021	AE-MDB	1400 kg (+/-	Part.no.	208317
4	A210505COEC	WP3.5_4	Piaggio	W/safety leg cover	2/2/2021		20 kg)	70AEMDB05L	208427

Table 1. Test matrix showing the four side barrier tests performed

Test vehicle

The overall vehicle specifications, including the manufacturer, body type, Vehicle Identification Number (VIN) number and test weight (both by axles and in total) is shown in Table 2.

Test	Test number		Vehicle			Test weight (kg)		
	IDIADA	Customer	Manufacturer	Body type	VIN	Front	Rear	Total
1	A210409COEC	WP3.5_1	DUCATI	Multistrada	ZDM12BWW2GB000042	144	190	334
2	A210410COEC	WP3.5_2	DUCATI	Multistrada	ZDMAA07AAJB019225	142	188	330
3	A210415COEC	WP3.5_3	PIAGGIO	MP3	ZAPTA120200001007	168	196	364
4	A210505COEC	WP3.5_4	PIAGGIO	MP3	ZAPTA10W3K5000163	168	197	365

Table 2. Vehicle specifications for each of the four tests

The pre-crash pictures showing the vehicle configuration for all four crash tests may be found in Figure 4.

Test 1   Test 2

Test 3   Test 4
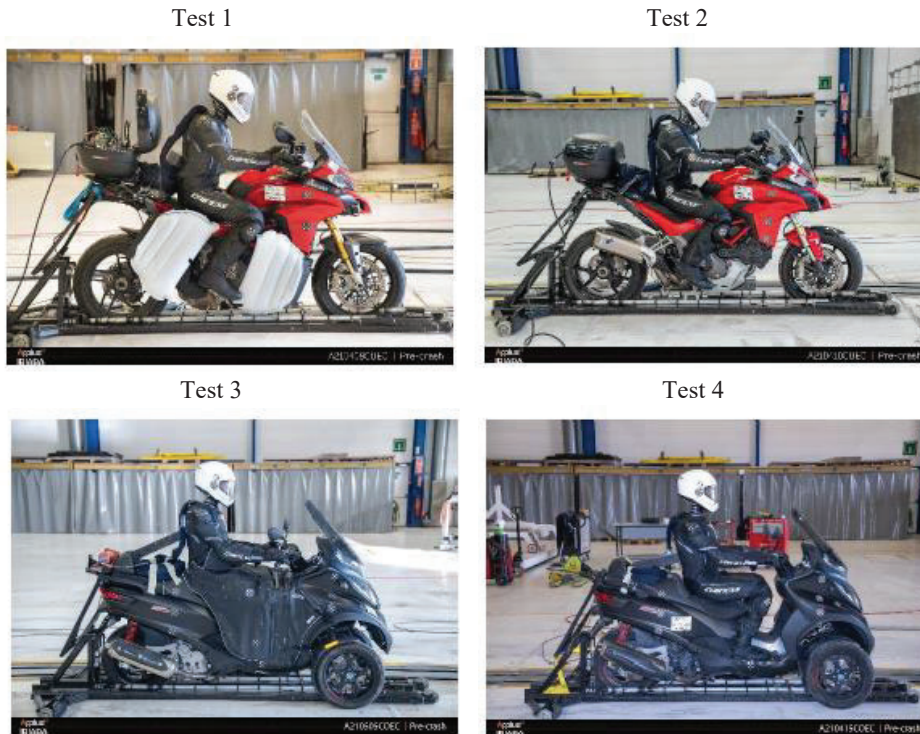
Figure 4. Images showing the vehicle configuration before each test

- Test 1: Without fuel and all other liquids, without chain, with dummy, with instrumentation, data acquisition system located in Top Case and with two lateral knee airbag modules mounted on the right side of the vehicle.
- Test 2: Without fuel and all other liquids, without chain, with dummy, with instrumentation and data acquisition system located in Top Case.
- Test 3: Without fuel and all other liquids, without chain, with dummy, with instrumentation, data acquisition system located in the Helmet box under the saddle and with safety leg cover mounted on the frontal part of the vehicle.
- Test 4: Without fuel and all other liquids, without chain, with dummy, with instrumentation and data acquisition system located in the Helmet box under the saddle.

Vehicle instrumentation

The tested motorcycles were instrumented with triaxial accelerometer sensors in order to obtain information for the post-crash in-depth analysis. Table 3 summarizes the vehicle instrumentation that was included in both tests.

		DUCATI		PIAGGIO	
	Magnitude	Direction	Channels	Direction	Channels
Frame attachment rear dumper	Acceleration	X, Y, Z	3	X, Y, Z	3
Frame under saddle	Acceleration	X, Y, Z	3	X, Y, Z	3
Frame left side of footrest	Acceleration	X, Y, Z	3	X, Y, Z	3
Steering head middle	Acceleration	X, Y, Z	3	X, Y, Z	3
Front right suspension up	Acceleration	-	-	X, Y, Z	3
	Total		12		15

Table 3. Vehicle instrumentation for both vehicles DUCATI and PIAGGIO

Dummy instrumentation

The dummy was composed of HIII 50th percentile male dummy head, neck, torso, and arms and Motorcycle Anthropomorphic Test Device (MATD) abdomen, pelvis and legs with the instrumentation found in Table 4:

Sensor location		Magnitude	Dir.	Channels
Head		Acceleration	X, Y, Z	3
		Angular Velocity	X, Y, Z	3
Neck Upper		Force	X, Y, Z	3
		Moment	X, Y, Z	3
Chest		Acceleration	X, Y, Z	3
		Deflection	X	1
		Angular Velocity	X, Y, Z	3
Lumbar Spine		Force	X, Y, Z	3
		Moment	X, Y, Z	3
Femur	Left Upper	Force	Z	1
		Moment	X, Y, Z	3
	Right Upper	Force	Z	1
		Moment	X, Y, Z	3
			Total	33

Table 4. Dummy instrumentation for all the tests executed

Dummy positioning

The dummy was positioned according to D3.1 (1) in order to reproduce as much as possible, the natural human riding position for 50% male rider's dummy. In addition, in order to stabilize the dummy torso, a foam block was used to support the dummy and avoid him leaning backwards when the motorcycle movement was initiated. An example of the position of this block in the PIAGGIO tests may be found below in Figure 5. This was also done in the DUCATI tests where the foam block rested against the top case.
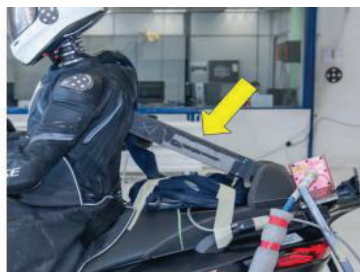

Figure 5. Foam block used to increase stability during the crash

Camera locations and views

At least 6 high-speed cameras that work at a sampling rate of 1000 fps must be used to record the test, filming from -15 ms to +1500 ms, including 1 real time film recorded with a normal or GoPro type camera.

Test tool, ATD
Vehicle sled

For vehicle propulsion and guidance, a special adaptable sled has been designed and manufactured by IDIADA. It is a modular tool that allows to fit different types and sizes of motorcycle to be impacted in a full-vehicle crash test. The vehicle sled can be adjusted to different motorcycle tyre widths and number of wheels.

The main goal is to control the forward movement of the motorcycle and ensuring the stability of the vehicle at every moment, especially at the crash moment.

The rear support of the sled is used to maintain the correct inclination of the motorcycle and to support the dummy to avoid the unwanted lateral movements. System of rollers has been developed in order to maintain the rolling of the wheels during the pre-crash acceleration.

The sled test setup designed within this project enables any type of motorbikes to be tested. As can be seen on Figure 6, the sled test can perform a test with a motorbike with one or two front wheels. The vehicle sled has two plates on the rear side that will impact to a couple of aluminium tubes installed in the crash area. This will allow the vehicle sled to gradually brake while releasing the motorbike at the desired speed to be impacted by the barrier.

Figure 6. Images of the vehicle sled fitting the two types of motorcycle before the test

Simulation environment

Virtual simulations of full-vehicle crash tests were performed for both on-board safety systems (DUCATI on-board side airbag and PIAGGIO safety leg cover).

First, a simulation environment was set up with FE models and impact conditions aimed to reproduce the test conditions. The complete simulation environment can be seen in Figure 7.
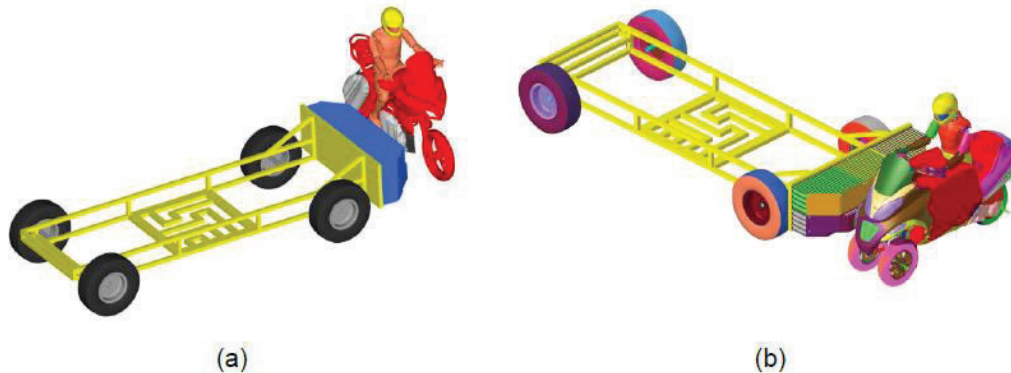

(a)   (b)

Figure 7. Full simulation environment for the airbags on Ducati Multistrada (a) and safety leg cover on Piaggio MP3 (B)

The simulation environment consist of finite element models of:
1. The main vehicle models used in the finite element simulation activities of Task 5.4 "Lateral Impact Mitigation" equipped with on-board safety systems
2. Test dummy (Figure 8).
3. Deformable barrier

Virtual sensors were created at the same locations, where IDIADA installed the sensors for the experimental tests, and the same orientation was implemented.

1. Main vehicle models

The motorcycle was modelled as a rigid body, as in the development phase of the airbags the primary concern was on leg protection and avoidance of its crushing between the car and the motorcycle. Since the motorcycle components that interact with the leg are much stiffer than the leg itself, the rigid body approximation was acceptable.

The simulation environment has two limitations which need consideration for a proper interpretation of the results: The rigid body approximation allows to have a correct representation of the inertia matrix of the vehicle, but the disadvantage is that front and rear suspensions are rigid (1st limitation) and the steering degree of freedom of the handlebar is suppressed (2nd limitation). The latter approximations may influence the kinematics of the motorcycle.

1a. Motorcycle with on-board side airbag

As shown in Figure 8, a Ducati Multistrada FE model was used, with a Hybrid III 50th percentile adult male dummy sitting on it.

Figure 8. FE model of the Ducati Multistrada, with sitting Hybrid III and airbags (grey boxes)

The environment was complemented by FE models developed by ZF, i.e., two airbags of the same type and model (Figure 9 and Figure 10) and the Advanced European Movable Deformable Barrier (AE-MDB), Version 1.0 specification, released on 26.02.2013.
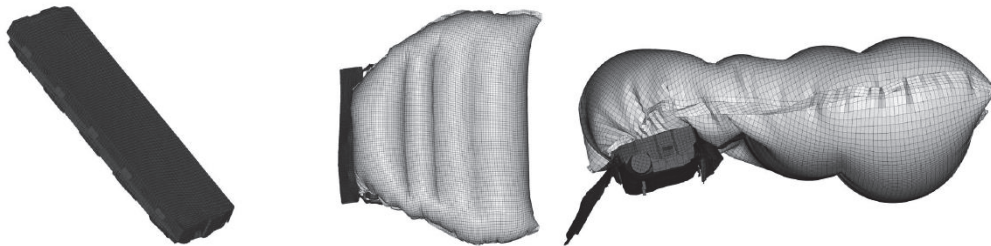
Figure 9 (left). FE model of the airbag in closed configuration; Figure 10 (right). FE model of airbag in open configuration (overhead view – left – and lateral view – right)

Since it was not possible to produce prototypes of the airbags developed in Task 5.4 the tests were performed using two knee airbags, designed for car applications. The airbags and their finite element models were provided by ZF to Ducati, and the models were integrated by UNIFI in the virtual environment on the basis of information provided by Ducati and IDIADA

1b. Scooter with safety leg cover

In Figure 10, the Piaggio MP3 500 FE model is shown, with Hybrid III dummy. Vehicle FE model is equipped with the final version of the safety leg cover which was designed and developed in Task 5.4 (Figure 11).
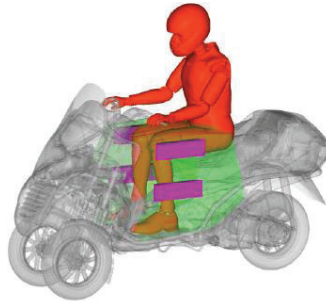
Figure 10. FE model of the MP3 scooter, with sitting Hybrid III and safety leg cover
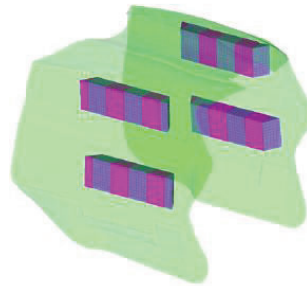
Figure 11. FE model of the safety leg cover: foam blocks of the protecting bars highlighted in alternated colours

2. Test dummy

Hybrid III dummy was selected for the simulations since there was no numerical finite element model of the MATD (7). As MATD has frangible bones (femur and tibia) and in literature (8) it is reported that different rider kinematics was observed after a bone fracture (bone fractures affect the rider's kinematics), the analysis of results has to factor these previous findings.

3. Deformable barrier

A model of the Advanced European Movable Deformable Barrier (AE-MDB) Version 1.0 specification, released on 26.02.2013 was used in the simulations.

TEST RESULTS

Actual vs. target test conditions

The four crash tests were successful from a testing point of view. The vehicle and barrier speeds were inside the target tolerance (specified based on IDIADA's testing experience) in all cases, as shown in Table 5.

	Test number		Vehicle speed (km/h)		Barrier speed (km/h)		Lab condition		
Test	IDIADA	Customer	Target	Actual	Target	Actual	Temperature (°C)	Humidity (%)	Pressure (mBar)
1	A210409COEC	WP3.5_1	30 (+/- 1)	29,68	30 (+/- 1)	29,68	21,3	48	1005
2	A210410COEC	WP3.5_2	30 (+/- 1)	29,8	30 (+/- 1)	29,8	19	70	1005
3	A210415COEC	WP3.5_3	30 (+/- 1)	30,63	15 (+/- 1)	15,31	21	47	1001
4	A210505COEC	WP3.5_4	30 (+/- 1)	30,4	15 (+/- 1)	15,18	20,3	42	1000

Table 5. Target and actual vehicle and barrier speeds and lab conditions during test

Main test findings

Overall, the crash tests were successful from a test execution point of view and were useful to confirm the behaviour predicted by means of virtual simulations. This made the tests themselves comparable and repeatable. The test results from the DUCATI crash tests conducted led to believe that the use of on-board motorcycle lateral airbags has a potential to improve rider safety in the event of a motorcycle being impacted laterally by a passenger vehicle.

It has been seen that the overall deformation of the AE-MDB deformable barrier (representing the passenger vehicle's front-end) is significantly reduced when the lateral airbags are used. Thus, the airbags have a cushioning effect, acting as energy absorbers between the passenger vehicle and the motorcycle, reducing the severity of the impact and delaying the barrier response. On the other hand, a slight reduction in injury measurements from the dummy sensors has also been found, together with a significant reduction in the dummy's excursion/free flight after the impact (Figure 12).

In the specific case of the PIAGGIO tests, the vehicle kinematic differences were significantly affected by the usual uncontrolled degrees of freedom of motorcycles (at least roll and steering). These kinematic differences are completely independent of the use (or lack thereof) of the safety leg cover. Therefore, no considerations about the post-crash motion of the rider and its related consequences from an injury perspective can be clearly drawn.
The Piaggio's range of speed is considered to be more urban (lower speed) and therefore a suitable on-board safety system, lower leg cover, was chosen (Figure 13).

The use of the safety leg cover did not show any significant changes (neither positive nor negative) of the leg extremity results (both from an injury metrics perspective and from a frangible bone fracture perspective); as the leg sensor response was similar between tests and the frangible tibias and femurs did not break in any of the two tests. [13]
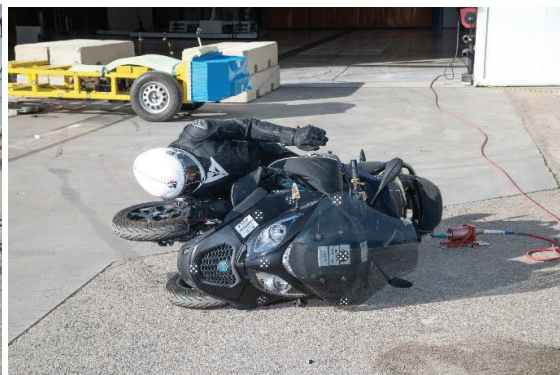

Figure 12. Post-crash, DUCATI with airbags   *Figure 13. Post-crash, PIAGGIO with leg cover*

Virtual simulations results
The airbag test renderings were performed at 32 / 74 / 112 / 152ms to align with the comparison of both tests. The limited size of the airbags doesn't influence massively the kinematic compared to the crash without the protection system. In the latter configuration, at 112 ms, the dummy is separating from the motorcycle and its movement is slightly anticipated compared to the configuration with the airbags.

The post-crash analysis of the barrier reveals that without airbags the leg of the dummy had a more direct impact with the barrier and the shape of the leg is visible in the deformed configuration. When the airbags were present, the barrier deformation was more uniform, and the load was partitioned between the airbags and the leg.

The leg cover test renderings were performed at 55 / 115 / 165 / 225ms to align with the comparison of both tests. The simulations without and with the safety leg cover were compared to assess a possible influence of the cover on the rider kinematics. The comparison shows only minor differences between the two series: only at 225ms in the simulation with the leg cover, the rider is closer to the scooter, as a result of an interaction of its movements with the leg cover. In the safety leg cover simulations the AE-MDB performed differently, and the speed reduction was higher in the configuration with the leg cover installed. The dummy response is very close in the two simulations until approximately 100 ms. Onwards there are differences in the load of the right leg (impact side) and the simulation with the leg cover shows lower load. The femur axial force of the left leg shows differences after 225 ms. Head and chest acceleration are similar, while higher rotation rate is reported in the configuration without leg cover after approximately 115 ms.

Conclusions on the experimental vs. virtual test comparison

The virtual environment has proved the capability to capture the main trends of the interaction of the barrier with the motorcycles (the curves of the COG acceleration and velocity are close). Also, the motorcycle acceleration at the footrest is on satisfying agreement between experimental and simulated data. The dummy sensor data at the legs show that there is agreement between simulations and experiments only in the initial part of the acquisitions. The main hypothesis is that differences amplify after the rupture of the tibia. The tilting movement during the experimental tests influenced the kinematics of the dummy and thus the comparison of the experimental and simulation activities. The dummy head and chest kinematics are in line with the respective video analysis, thus the hypothesis of a satisfactory agreement between experimental and simulated kinematics, in case of equal tilting, seems plausible but needs further verification. Such tests could further validate that Hybrid III dummy is appropriate to reproduce the rider kinematics if there are no bone fractures.

The results confirm the potential of the virtual environment as design tool for the lateral airbags, but the following improvements are necessary to have a better correlation with the experimental data:

1. Refinement of the motorcycle model, introducing at least the steering degree of freedom,
2. Development of a model of the lower limbs, reproducing the characteristics of the MATD.

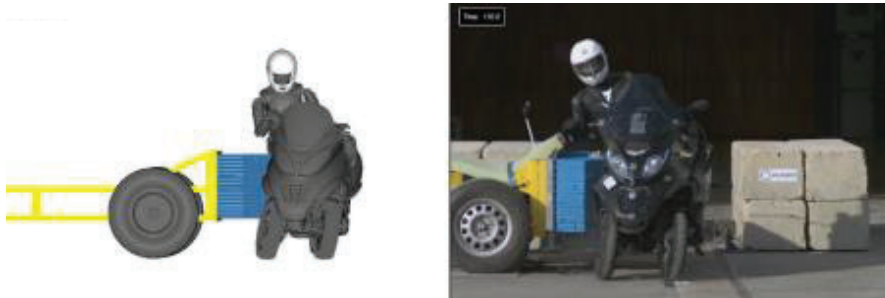*Figure 14. Impact with airbags: front view at 74ms*

Figure 15. Impact with leg protector: front view at 115 ms

LIMITATIONS

There were some limitations encountered when preparing and conducting the tests:

- There was no tracking of the dummies in the physical tests as it was not in the scope of the PIONEERS project.
- Only 4 tests were conducted. More motorcycles and barriers would have been needed to perform extra tests in order to obtain more precise results.
- Dummy combination of HIII and MATD: Unfortunately, due to the MATD's lower leg characteristics, it was not possible to assess the exact level of injury suffered in the tibias as the tibia load cells were not compatible with the use of the frangible bones. Because, of this, further research would be required in order to be able to quantify this injury and fully evaluate the potential of the on-board side airbag implementation in the DUCATI Multistrada.
- No instrumentation of the tibias: For the same reason as before, the tibias on the Ducati tests had no instrumentation.
- As explained earlier, the airbags were already inflated due to the problems / delays due to COVID. The used airbags were knee airbags, adapted to the tests.

CONCLUSIONS

This document describes the procedures and environment for the tests carried out within the PIONEERS project. The goal of the tests was validation and evaluation of two protective innovations of new equipment for enhanced rider safety. Those systems consisted of a leg cover and a lateral airbag, as countermeasures proposed in case of lateral impact.

In order to execute those tests a new test method was developed using an AE-MDB deformable barrier used for lateral impact passenger car evaluation. Indeed, motorcycles do not have a safety regulation that covers crash tests and are not as extensively tested as other types of motorized vehicles under those conditions. Therefore, this new test method consists of a series of physical full-vehicle crash tests that were conducted and also reproduced in simulation environment by means of detailed FE models of the vehicles.

The full-vehicle crash test results were used to validate virtual simulations and to confirm them as a reliable design tool; moreover, they served to study the feasibility of passive safety devices for lateral impact mitigation. While there were certain limitations due to the context, those tests were executed, and the results proved the validity of the test method proposed.

ACKNOWLEDGEMENTS

REFERENCES

1. **Soriano, Enric, et al.** *Test procedures for PPE, helmet and full vehicle.* s.l.: PIONEERS D3.1, 2020.

2. *Characterizing the performance of a single-layer fabric system through a heat and mass transfer model – Part II: Thermal and evaporative resistances.* **Ding, Din, et al.** 2011, Vol. Textile Research Journal.

3. *Glass Transition Temperature of Nylon 6.* **Forster, Michael. 38-5,** 1968, Vol. Textile Research Journal.

4. *The Glass Transition of Nylon 6.* **Greco, L. et al.** 1976, Vols. Macromolecules 9-4.

5. *Effect of Splitting on the Tensile Strength of Leather.* **Wilson, John Arthur et al.** 1926, Vol. Ind. Eng. Chem.

6. *Behavior of leather as a protective heat barrier and fire-resistant material.* **Bacardit, Anna et al.** 105-2, 2010, Vol. Journal of the American Leather Chemists Association.

7. **Maffè, Francesco, et al.** *Demonstrators of lateral impact mitigation system. D5.3 PIONEERS. 2020.*

8. *A Standardized Motorcyclist Impact Dummy for Protective Device Research.* **J.W. Zellner, K.D. Wiley, N.L. Broen, J.A. Newman.** 1996. 15th International Technical Conference on the Enhanced Safety of Vehicle. Paper Number 96-S10-W-21.

9. **SAE International.** *Surface Vehicle Recommended Practice. (R) Instrumentation for Impact Test - Part 1 - Electronic Instrumentation.* 2014. SAE J211-1 /1_2014-03.

10. *Application of crash pulse on the car crashworthiness design.* **Tso-Liang Teng, Peng-Hsiang Chang, Cho-Chung Liang and Da-AnFung. s.l.: Journals Sage,** 2017, Vols. Advances in Mechanical Engineering. Vol. 9 (9) 1-8. DOI 10.1177/168781 4017700096.

11. **EuroNCAP.** *AE-MDB Specification, Technical Bulletin TB014. 2013.*

12. *Powered Two-Wheelers – Road Traffic Accident Scenarios and Common Injuries.* **Wisch, Marcus. Breunig, Sandra. et al.** *PIONEERS PROJECT D1.1,* 2019.

13. *Test results.* **Di Piazza, Simone. et al.** *PIONEERS PROJECT D3.3,* 2021.

A COMPARISON OF THE SID-IIS ATD TO THE GLOBAL HUMAN BODY MODEL CONSORTIUM FIFTH PERCENTILE FEMALE MODEL IN THE INSURANCE INSTITUTE FOR HIGHWAY SAFETY (IIHS) UPDATED SIDE IMPACT CRASH TEST (SIDE 2.0).

Anthony Dellicolli
Jeff Dix
Nissan Technical Center North America
United States of America

Russ Morris
Benjamin K. Shurtz
Autoliv
United States of America

Paper Number 23-0282

ABSTRACT

This paper will present a study comparing the response of the SID-IIs Anthropomorphic Test Device (ATD) to the Global Human Body Model Consortium fifth percentile female model (GHBMC F05 v5.1) in the Insurance Institute for Highway Safety (IIHS) updated side impact crash test (Side 2.0). The study was conducted using a CAE model correlated to a barrier crash test with a small SUV. The occupant kinematics as well as injury response of the SID-IIs was compared to that of the Human Body Model (HBM). The SID-IIs response generally agreed well with the human body model except for clockwise pelvis Z-axis rotation resulting from the 'M-shaped' door deformation pattern characteristic of the IIHS Side Impact 2.0 test; additionally, the femur moment measured on the SID-IIs was significantly higher than that measured in the HBM. A CAE model of a simplified bending test was created to study the loading mechanism driving the femur moment responses and clarify the reasons for the differences observed for the HBM and SID-IIs. Through this study it was found that the SID-IIs hip allows for only 10-12 degrees plan view articulation before mechanical joint lockout occurs. In the barrier test the clockwise pelvis rotation of the SID-IIs resulted in the lockout of the hip joint on the SID-IIs. As a result, the femur moment unrealistically increased exponentially compared to that of the HBM after hip joint lockout occurred. As such the SID-IIs as currently designed does not provide a biofidelic response for femur moments and pelvis rotation in the IIHS Side Impact 2.0 test.

BACKGROUND

Introduced and implemented in 2003, the Insurance Institute for Highway Safety (IIHS) Side Impact Crashworthiness Evaluation Program started rating vehicles based upon three areas of performance in a single-moving, 90-degree, deformable barrier impact [1]. The three areas of performance were evaluating Anthropomorphic Test Device (ATD) injury metrics using a Side Impact Dummy (SID-IIs) representing a 5th percentile female in the front and rear seating positions, head protection, and vehicle structural performance. The SID-IIs was positioned in both the driver's position as well as the 2nd row left seating position during the test, and the 1,500kg (3,300lbf) moving deformable barrier (MDB) impacted the left side of the tested vehicle at 50kph (31mph). From this point forward in this paper, this original testing procedure will be referred to as IIHS Side Impact 1.0.

IIHS continued its side impact research, which included analysis of data from the National Automotive Sampling System (NASS), the Fatality Analysis Reporting System (FARS), and the Crash Injury Research and Engineering Network (CIREN), as well as full-scale vehicle-to-vehicle side impact tests and simulations [2, 3]. Through this research IIHS observed that despite vehicle performance improvements driven by their current side impact evaluations, serious injuries and fatalities were still occurring in currently "Good" rated vehicles. IIHS further identified that side impacts occurring in the field were resulting in greater intrusion, as well as more specific intrusion patterns, in the struck vehicle, and more specific occupant injuries.

IIHS desired to better represent the high severity side impact crashes observed through their field research [4, 5]. Analysis of internal vehicle-to-vehicle side impact testing showed a more specific type of deformation to the impacted vehicle, a deformation pattern that IIHS referred to as an 'M-shaped' deformation pattern [6, 7]. This deformation pattern, IIHS observed, had specific relationships to lower body loading. This led to the introduction of what is now commonly referred to as IIHS Side Impact 2.0, and changes to the program include an MDB redesign, increased impact speed, modifications to the ATD injury criteria, and changes to the overall rating scoring methodology [7]. To achieve the deformation pattern, the MDB honeycomb structure was redesigned, both in sub-component geometry and overall size, with the intent to better represent modern SUVs and Pickup Trucks. Further, the MDB cart also increased in mass to 1,900kg (4,189lbf), and the impact speed was increased to 60kph (37mph). Raising both the mass and speed resulted in an over 80% increase to the initial kinetic energy of the test between IIHS Side Impact 1.0 and 2.0 tests.

IIHS made modifications to the way they analyze ATD injury metrics, which included eliminating some of the measured injury parameters [8]. The eliminated parameters related to the pelvis and femur and included the individual iliac and acetabulum pelvic forces as well as the anterior-posterior and lateral-medial forces and moments at the femur. A summary of the common injury parameters between IIHS Side Impact 1.0 and 2.0 test, and their associated injury protection ratings, can be found in Table A within the Appendix.

While ATD's have been shown to demonstrate good correlation to human injury metrics for specific crash modes, environments, and locations on the human body, they are not without limitations [9, 10, 11]. Despite ongoing and well-researched improvements to ATD's in the last several decades, there are still areas of the human body where the use of man-made components as surrogates for biological tissues falls short of ideal representation [12, 13]. Human joints, specifically those with complex and multiple degrees of freedom, are challenging to re-create with mechanical components. The femur-pelvis interface is one of these complex joints.

An integral part of the worldwide effort to develop better tools for analyzing injury mechanisms and tolerances of human joints, as well as the entire human body, has been the Global Human Body Models Consortium (GHBMC). Created in 2006, the GHBMC strives to consolidate worldwide research and development activities to develop and maintain high-fidelity finite element human body models for automotive crash simulations. The consortium has established specific Centers of Expertise (COE) and Body Region Model (BRM) responsibilities within the overall global effort, including the body region comprising the pelvis and lower extremities. The research and development activities of the GHBMC include the purposeful collection of full-body 3D scanning data from live subjects, as well as the analysis of data collected during full-scale impact testing using human cadavers. An ongoing result of this work has been the development of continuously refined and improved models of a variety of sized and aged humans, including a fifth-percentile female model.

The objective of this paper is to compare the response of the SID-IIs and HBM in the IIHS Side Impact 2.0 test. To study this, injury response and kinematic comparisons are presented first between the SID-IIs in a IIHS Side Impact 2.0 physical vehicle test versus a representative CAE model and then later between the SID-IIs and the HBM in the same CAE model. In cases where the occupant behavior was not similar, further investigation was done to understand the reason for the difference.

METHODS

This study compared the occupant kinematics and injury response of the SID-IIs versus the HBM in the IIHS Side Impact 2.0 test using CAE modeling. The baseline physical data to correlate the model was a crash test of a small SUV in the IIHS Side Impact 2.0 test conducted according to the IIHS Crash Test Protocol (DRAFT - Version I, April 2020). Vehicle and driver ATD response data were collected and used as a reference for CAE model correlation.

ATD and HBM Information
All CAE simulations were conducted using LsDyna version mpp971_s_R9.3.1_140922. The SID-IIs model used in the simulations was version 4.3.2 from Humanetics, which was the latest version at the beginning of the study. This model represents the physical ATD used in the IIHS Side Impact 2.0 test. The HBM used in the study was the GHBMC 5th percentile female detailed model (GHBM F05-O v5.1). The 5th percentile HBM was selected as it represents the same size of occupant the SID-IIs was designed to represent.

Vehicle Test CAE Model
A vehicle test CAE model, including vehicle parts relevant to the driver interaction in the IIHS Side Impact 2.0 test, was created and designed to replicate the dynamic door deformation and seat pulse as input to the driver. The pulse inputs, as well as door trim and seat material characteristics and frictions were tuned until the SID-IIs kinematics and injury responses correlated to those of the SID-IIs in the physical vehicle test. The SID-IIs was then replaced in the CAE model with the HBM, and occupant kinematics and injury responses were compared. The simulation matrix is shown visually in Figure 1.
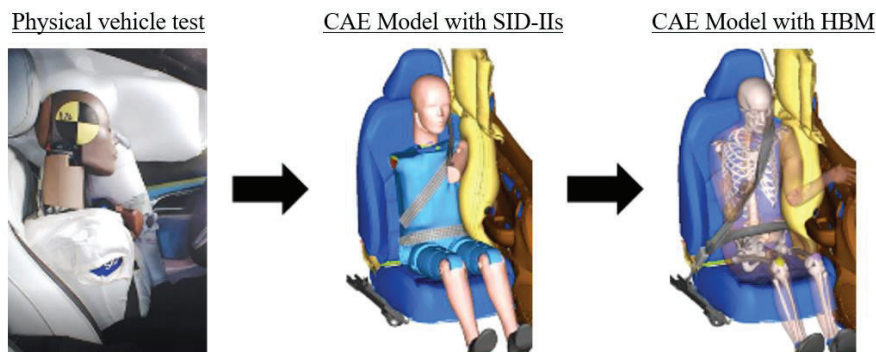

Figure 1. Simulation matrix: A CAE model with SID-IIs, correlated to a physical vehicle test, and then a CAE model that replaces the SID-IIs with the HBM.

The plan view of the post-test measurement laser scan section cut at the occupant H-point height of the physical test vehicle to which the CAE model is correlated exhibited the 'M-shaped' deformation pattern along the doors and B-pillar (See Figure 2). As previously mentioned, this deformation pattern is created by the design changes to the MDB honeycomb structure for the IIHS Side Impact 2.0 test.
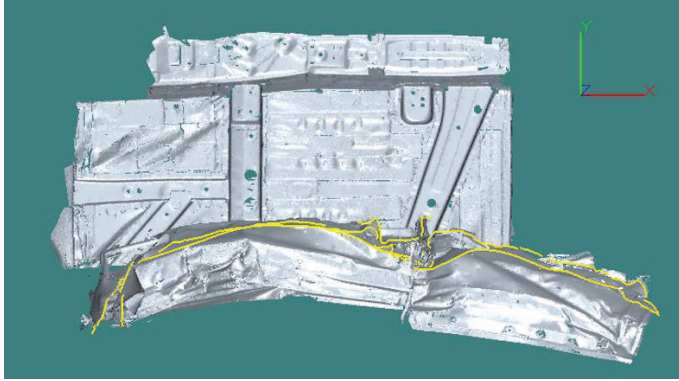
Figure 2. Plan view of the post-test measurement laser scan section cut at the occupant H-point height of the physical test vehicle.

Vehicle Test CAE Model Correlation

The CAE model with the SID-IIs dummy was developed to match the kinematics and injury responses of the physical IIHS Side Impact 2.0 vehicle test. The correlation of injury responses in the CAE model compared to the physical vehicle test can be seen in Figure 3.
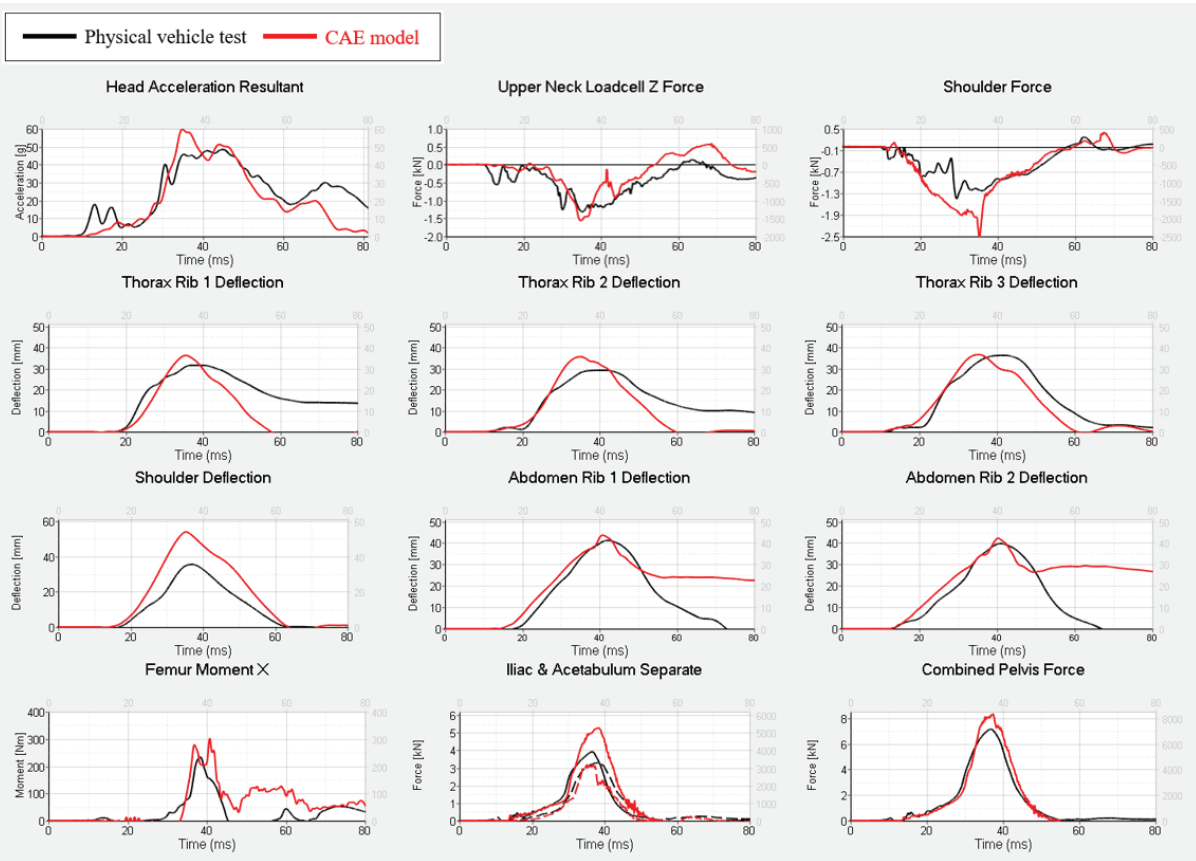

Figure 3. Injury response comparison between physical vehicle test and CAE model.

HBM Positioning

The positioning of the HBM (See Figure 4) was done in Primer v17.0. It was started by matching the H-point to that of the SID-IIs. The heel points were aligned to set the thigh and leg. The torso angle was matched. Then, the elbows were aligned to set the arm. Finally, the head center-of-gravity was matched.
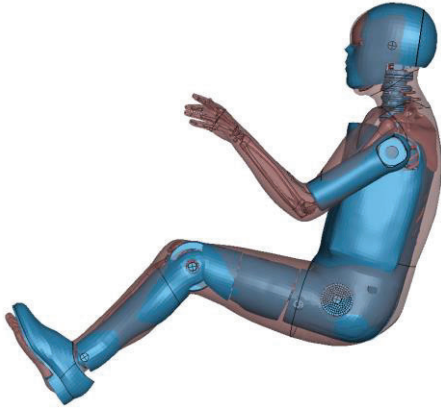
Figure 4. Overlay of the SID-IIs (blue) and HBM (brown) in their seated position for the CAE simulation.

Response Outputs
The CAE model of the SID-IIs comes from the supplier with instrumentation defined to measure accelerations, internal forces and moments, and local deflections of ribs at the same locations and using the same local coordinate systems as the physical dummy. For CAE correlation to the physical vehicle test, the responses of concern were those of the head, neck, shoulder, thorax, pelvis, and femur.

The F05-O HBM CAE model also comes from the supplier with pre-defined instrumentation to measure local accelerations of various body regions, internal forces and moments, and local deflections. In addition, the HBM can be used to predict bone fracture and internal organ injury based on the stresses and strains that develop during crash-induced loading. Because there is no rigid structure at the head CG, the head acceleration was output from a node located at the head CG that is constrained to a rigid skull plate using Ls-Dyna's constrained interpolation. The neck forces and moments were extracted from a cross-section through the C2 vertebra. For shoulder force, the HBM acromio-clavicle force measurement was selected as the nearest representation of the shoulder force an ATD would measure. For rib deflection measurement, the HBM model comes equipped with three virtual chestbands (See Figure 5).
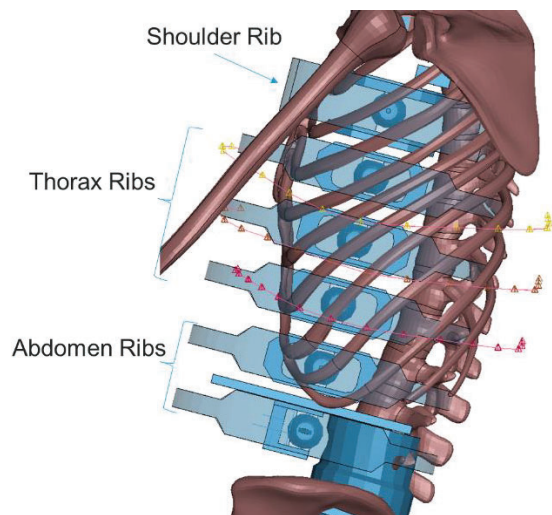
Figure 5. Chestbands on the HBM, located to align with the SID-IIs thorax ribs.

Thorax deflection was calculated from these chestbands using the half thorax deflection method, as is commonly done in physical side impact testing of post-mortem human surrogates [15, 16]. The left iliac and acetabulum forces along with the left femur X-axis moment were also output for comparison to the SID-IIs. The femur loadcell location in the F05-O v5.1 HBM pre-defined instrumentation was positioned more distal on the femur than the

loadcell in the SID-IIs. To ensure a fair comparison of HBM and ATD femur moments, an alternate femur loadcell was defined corresponding to the SID-IIs instrumentation (See Figure 6).
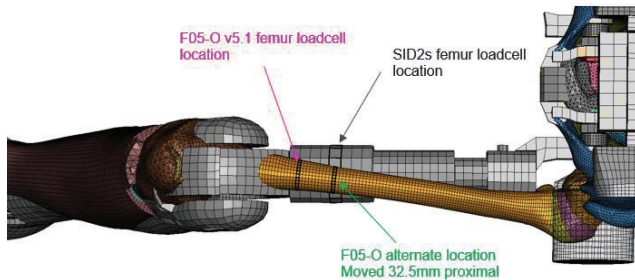

Figure 6. SID-IIs and GHBMC F05-O v5.1 femur loadcell definitions.

Simplified Femur Bending Test CAE Model
When the simulated SID-IIs and HBM results were compared, a large difference was seen in the measured femur x-moments of the two occupants. To better understand the femur moment and its relationship with thigh-pelvis Z-axis rotation, a CAE model of a simplified femur bending test was created and used to further compare response of the SID-IIs and HBM. The simplified model is shown in Figure 7 for the SID-IIs load case. A force was applied to the medial aspect of the knee to push the knee laterally. A constraint was also placed on the lateral aspect of the upper thigh to prevent lateral motion at that point. The locations of the forces correspond to one knee contacting the other while the thigh is constrained against the intruding door. The force couple in the bending simulation induced Z-axis rotation of the thigh (counterclockwise) relative to the pelvis, which was fixed, and as a result induced a bending moment about the local x-axis measured by the femur load cell.

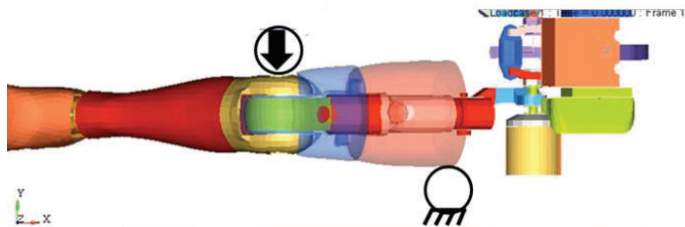***Figure 7. Bending simulation setup with a force acting laterally on the medial aspect of the knee and a constraint on the lateral thigh.***

RESULTS AND DISCUSSION

Vehicle Test CAE Model
The occupant kinematics in the CAE model were compared visually in an oblique view from 0 to 60ms at 20ms increments (See Figure 8). The SID-IIs and HBM showed similar kinematic behavior throughout the event.
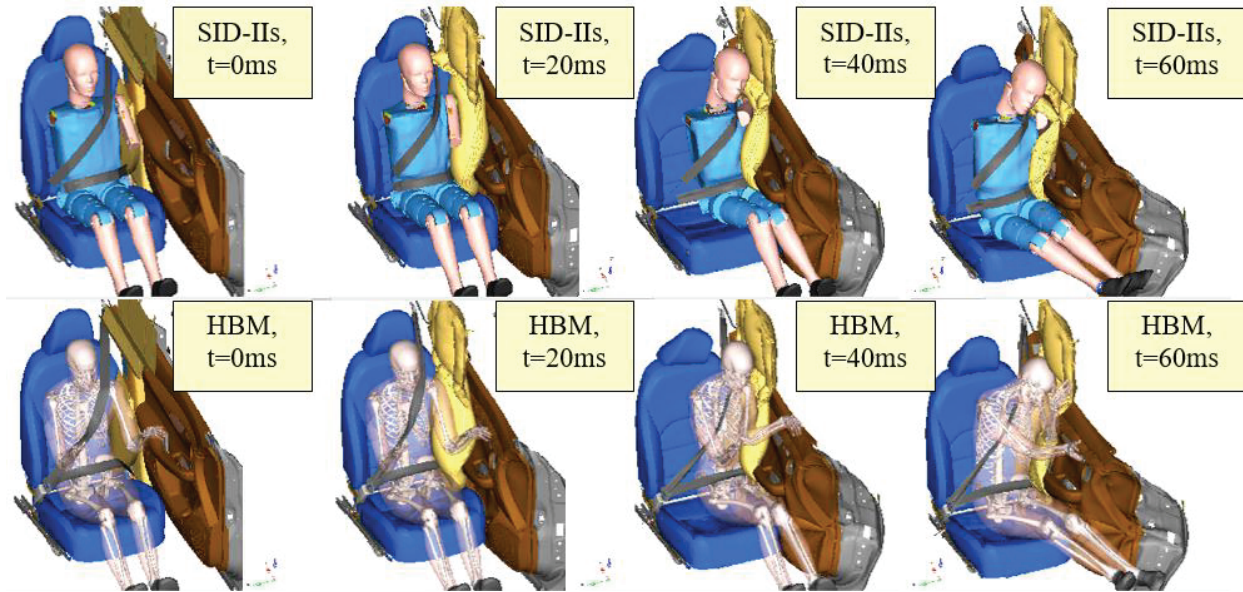
Figure 8. CAE model front view and profile view of SID-IIs and HBM from 0 to 60ms at 20ms increments.

Based on a plan view section of the SID-IIs and HBM at 0ms and 40ms, the SID-IIs exhibits clockwise pelvis Z-axis rotation due to the 'M-shaped' door deformation pattern characteristic of the IIHS Side Impact 2.0 test whereas the HBM pelvis is compressed and pushed laterally inboard rather than rotating (See Figure 9).
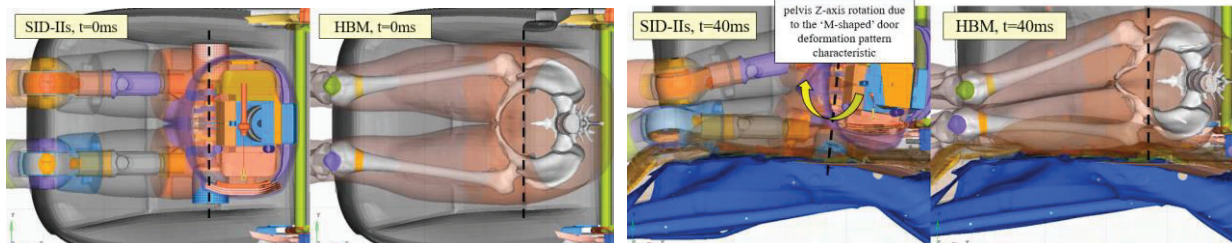
Figure 9. CAE model plan view section of SID-IIs and HBM at 0ms (left) and 40ms (right) showing SID-IIs clockwise pelvis Z-axis rotation.

The HBM injury responses in the CAE model were compared to the SID-IIs and only showed slight variations in loading characteristics and peak values for all body regions except for the HBM's peak femur moment which was seven times less than that of the SID-IIs (See Table 1).

Table 1.
Peak Injury Value Comparison Between SID-IIs and HBM

Injury parameter	SID-IIs	HBM	Percent difference
Head resultant acceleration (g)	50	60	20%
Neck force, Z-axis (N)	1300	1200	8%
Shoulder force, Y-axis (N)	1700	1000	41%
Upper rib deflection (mm)	26	33	27%
Middle rib deflection (mm)	28	27	4%
Lower rib deflection (mm)	32	31	3%
Combined iliac and acetabulum force (N)	6000	5700	5%
Femur moment, X-axis (Nm)	325	44	86%

The loading characteristic of the resultant head acceleration and upper neck force (Z-axis) for the SID-IIs and HBM were similar (see Figures 10 and 11). The peak head resultant acceleration for the SID-IIs was 10g's less compared to the HBM. The peak upper neck force for the SID-IIs was 100N more compared to the HBM. The 10ms earlier ramp up timing observed in the SID-IIs head resultant acceleration and upper neck force (Z-axis) around 20-25ms was attributed to shoulder geometry and stiffness differences between occupants that produce different shoulder loading characteristics (See Figure 12). The SID-IIs shoulder force exhibits the same earlier loading time compared to the HBM, albeit at an earlier event time around 10ms and therefore indicative that the shoulder loading time difference causes the earlier head and neck loading in the SID-IIs. The peak shoulder force for the SID-IIs was 700N more compared to the HBM.
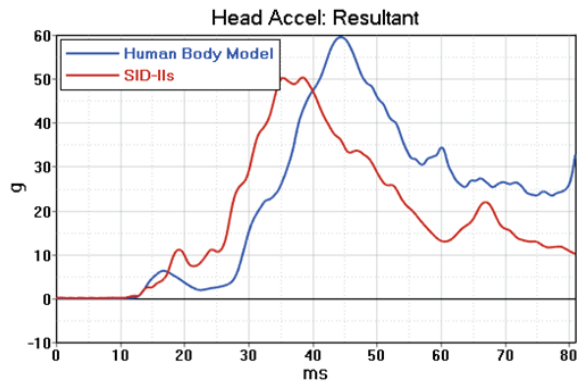

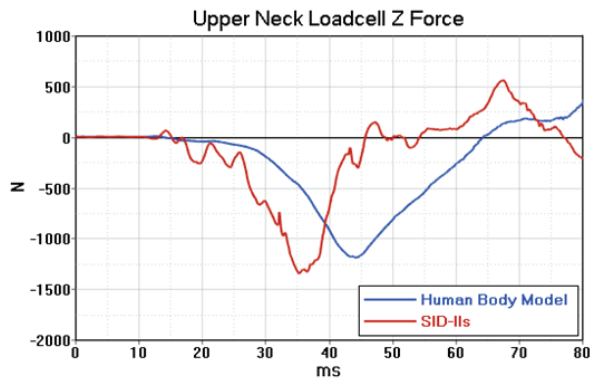Figure 10. Head resultant acceleration vs. time.

Figure 11. Upper neck force (Z-axis) vs. time.
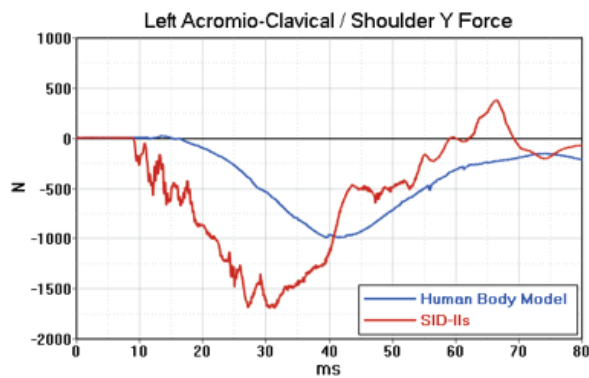
Figure 12. Shoulder force (Y-axis) vs. time.

The loading characteristics and peak values of the upper, middle, and lower thorax rib deflections for the SID-IIs and HBM were similar (See Figures 13, 14, and 15). The peak upper thorax rib deflection was 7mm less in the SID-

IIs compared to the HBM. The SID-IIs middle and lower thorax rib deflections had a longer load duration compared to the HBM but the peak values were approximately the same. The load timing for all thorax rib deflections was well aligned between occupants.
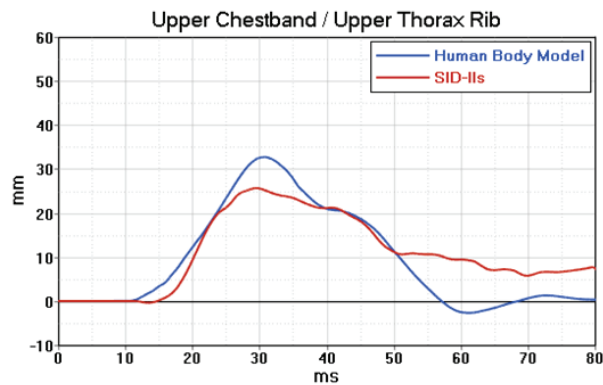
Figure 13. Upper thorax rib deflection vs. time.
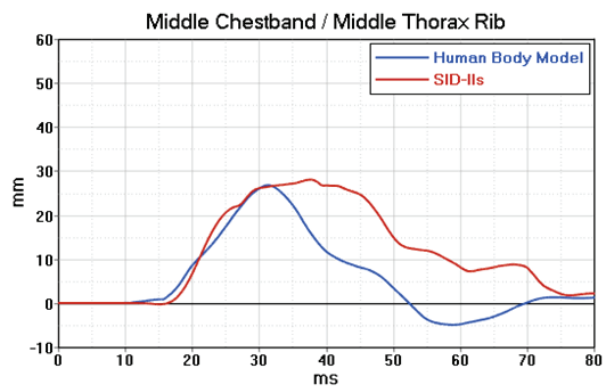
Figure 14. Middle thorax rib deflection vs. time.
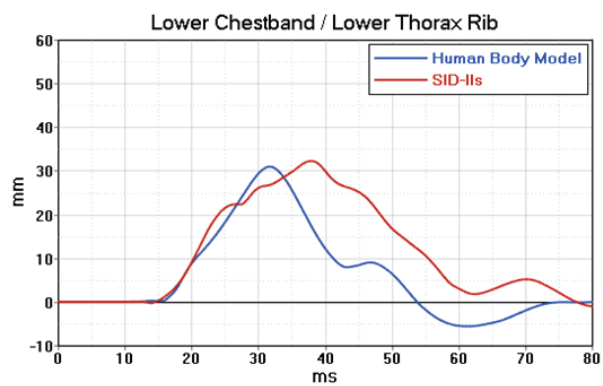
Figure 15. Lower thorax rib deflection vs. time.

The iliac force and acetabulum peak force distribution for the SID-IIs and HBM were not aligned due to differences in occupant geometry (See Figures 16 and 17). However, the loading characteristic and peak value of the combined iliac and acetabulum force (Y-axis) were similar (See Figure 18). The similarity in the combined iliac and acetabulum force indicates that the SID-IIs clockwise pelvis Z-axis rotation caused by the 'M-shaped' door deformation pattern characteristic does not influence pelvis injury performance when compared to the HBM.
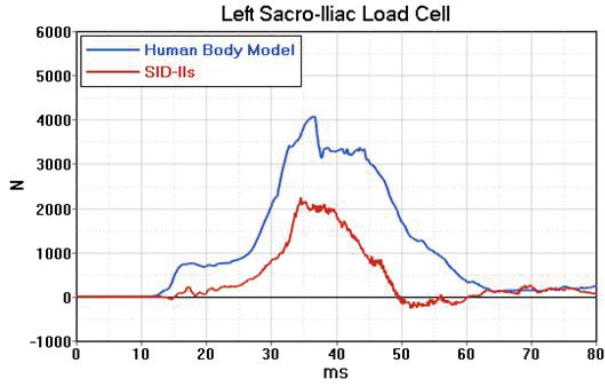
Figure 16. Iliac force (Y-axis) vs. time.
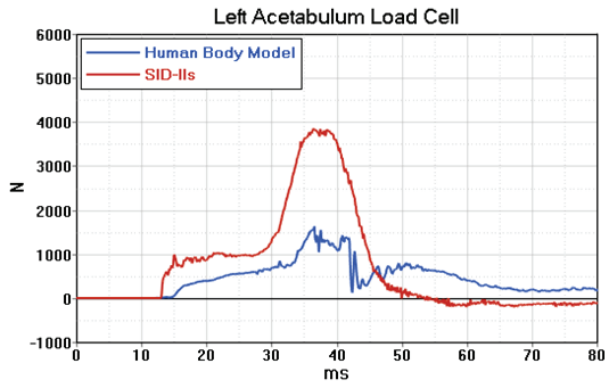
Figure 17. Acetabulum force (Y-axis) vs. time.
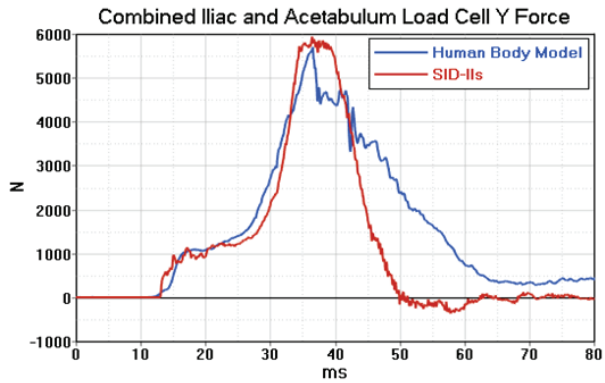
Figure 18. Combined iliac and acetabulum force (Y-axis) vs. time.

The measured SID-IIs femur moment was significantly higher compared to the HBM (See Figure 19). Whereas the HBM experiences minimal femur moment, the peak femur moment in the SID-IIs is nearly seven times higher than the HBM.
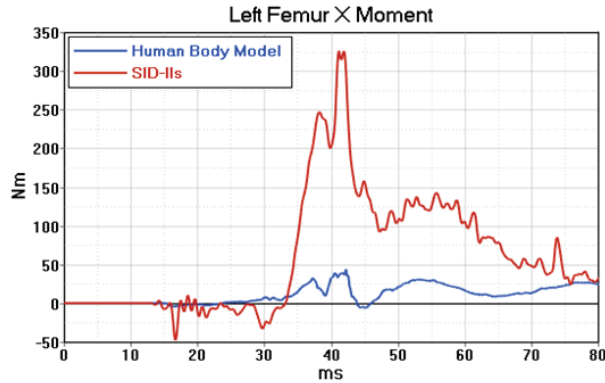
Figure 19. Femur moment (X-axis) vs. time.

There was a femoral neck fracture seen in the HBM simulation results. However, the model was rerun with bone fracture turned off and it was confirmed that the potential loss of load resulting from the femoral neck fracture did not explain the lower femur moment.

Out of all the injury parameters compared between the SID-IIs and the HBM, the femur moment was by far the biggest difference. To further investigate the mechanism causing the difference in peak femur moment, a simplified femur bending test CAE model was created, as discussed previously.

Simplified Femur Bending Test CAE Model
The simplified bending test CAE model was run for both the SID-IIs and HBM occupants. The femur moment was measured as knee displacement was increased from 0 to 100mm (See Figure 20). At approximately 80mm of knee displacement, the SID-IIs femur moment suddenly transitioned from increasing linearly to increasing exponentially between 80 to 100mm of knee displacement. By comparison, the HBM femur moment increases linearly throughout the entire range of knee displacement. During the linear phase of loading, it was observed that the SID-IIs femur moment is almost exactly double the HBM femur moment throughout thigh rotation up until approximately 80mm of knee displacement due to differences in flesh stiffness between the SID-IIs and HBM. This is further indication that a similar loading generates nearly twice the moment in the SID-IIs as compared to the HBM, even at relatively small angles between the femur and pelvis. At larger angles, the difference becomes more extreme due to the biofidelic limitations of the SID-IIs hip ball-joint.
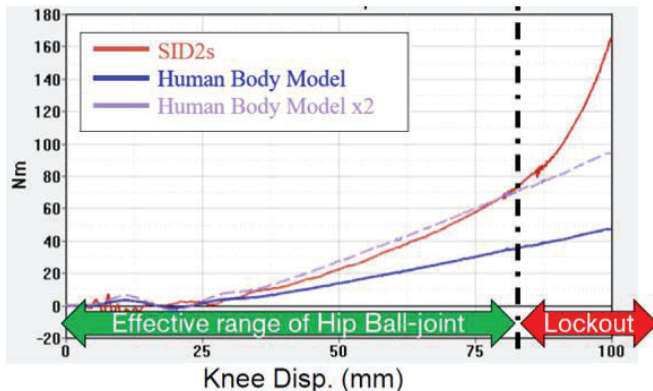
Figure 20. Left femur moment (X-axis) vs. knee displacement for SID-IIs and HBM in bending test CAE model.

After further inspection of a physical SID-IIs dummy, it was found that this CAE model identified the difference in effective range of hip ball-joint between the SID-IIs and HBM. By design, the SID-IIs hip allows for 10-12 degrees of articulation before mechanical joint lockout occurs (See Figure 21). The HBM does not share this design limitation. The limited articulation range for the SID-IIs hip corresponds to a fixed amount of outboard knee displacement in the simplified bending test CAE model, after which the SID-IIs femur moment unrealistically increases exponentially compared to the HBM due to joint lockout.
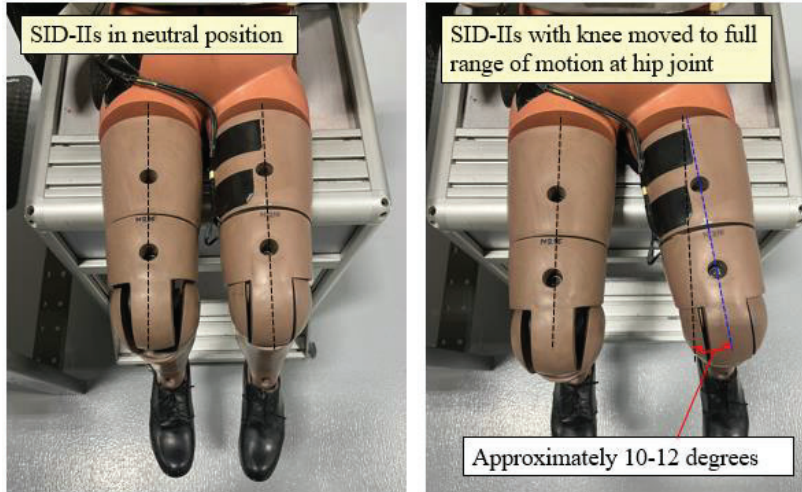
Figure 21. SID-IIs with legs in neutral position compared to SID-IIs with left knee moved to full range of motion at hip joint.

This component test is representative of the SID-IIs clockwise pelvis rotation that occurs in the IIHS Side Impact 2.0 test due to the 'M-shaped' door deformation pattern characteristic. Based on this result, it can be concluded that the limitation of SID-IIs femur biofidelity as currently designed is the root cause for the increased SID-IIs femur moment compared to that of the HBM in the IIHS Side Impact 2.0 test.

CONCLUSIONS

This study analyzed the differences in kinematics and injury responses between the SID-IIs and HBM in the IIHS Side Impact 2.0 test. The occupants had similar kinematics except for the SID-IIs demonstrating clockwise pelvis Z-axis rotation due to the vehicle's M-shaped body deformation pattern characteristic. While the combined iliac and acetabulum force injury response was similar between the occupants, the SID-IIs predicted a significantly higher femur moment due to biofidelic limitations of the hip joint that caused the femur moment to increase exponentially after joint lockout. Therefore, the SID-IIs as currently designed does not provide a biofidelic response for femur moment and pelvis rotation in the IIHS Side Impact 2.0 test when compared to the HBM.

ACKNOWLEDGMENTS

REFERENCES

[1] Dakin, G. J., Arbelaez, R. A., Nolan, J. M., Zuby, D. S., & Lund, A. K. (2003, May). Insurance institute for highway safety side impact crashworthiness evaluation program: impact configuration and rationale. In *18th ESV Conference, Nagoya*.

[2] Arbelaez, R.A., Baker, B.C., and Nolan, J.M., "Delta Vs for IIHS Side Impact Crash Tests and Their Relationship to Real-World Crash Severity", 2005, Proceedings of the 19th International Technical Conference on the Enhanced Safety of Vehicles, Paper Number 05-0049

[3] Brumbelow, M.L., Mueller, B.C., and Arbelaez, R.A., "Occurrence of Serious Injury in Real-World Side Impacts of Vehicles with Good Side-Impact Protection Ratings", 2015, Traffic Injury Prevention, DOI:10.1080/15389588.2015.1020112

[4] Brumbelow, M.L., Mueller, B., Arbelaez, R.A., and Kuehn, M., "Investigating Potential Changes to the IIHS Side Impact Crashworthiness Evaluation Program", 2017, Proceedings of the 25th International Technical Conference on the Enhanced Safety of Vehicles, Paper Number 17-0083

[5] Arbelaez, R.A., Mueller, B.C., Brumbelow, M.L., and Teoh, E.R., "Next Steps for the IIHS Side Crashworthiness Evaluation Program", 2018, 62nd Stapp Car Crash Conference, SC18-02

[6] Mueller, B.C., Arbelaez, R.A., Brumbelow, M.L., Nolan, J.M., "Comparison of Higher Severity Side Impact Tests of IIHS-Good-Rated Vehicles Struck by LTVs and a Modified IIHS Barrier with the Current IIHS Side Test and Real-World Crashes", 2019, Proceedings of the 26th International Technical Conference on the Enhanced Safety of Vehicles, Paper Number 19-0193

[7] Mueller, B., "IIHS Side Impact 2.0 Barrier Development", April 2020, iihs.org

[8] Side Impact Crashworthiness Evaluation 2.0 Ratings Guidelines, September 2021, iihs.org

[9] Irwin, A. L., Mertz, H. J., Elhagediab, A. M., & Moss, S. (2002). Guidelines for assessing the biofidelity of side impact dummies of various sizes and ages. *Stapp Car Crash Journal*, *46*, 297-319.

[10] Rhule, H. H., Maltese, M. R., Donnelly, B. R., Eppinger, R. H., Brunner, J. K., & Bolte, J. H. (2002). *Development of a new biofidelity ranking system for anthropomorphic test devices* (No. 2002-22-0024). SAE Technical Paper.

[11] Yoganandan, N., Pintar, F., Maltese, M., Eppinger, R., Rhule, H., & Donnelly, B. (2002). Biofidelity evaluation of recent side impact dummies. *Proceedings of the IRCOBI, Munich, Germany*, 57-69.

[12] Kemper, A., Stitzel, J., Duma, S., Matsuoka, F., & Masuda, M. (2005, June). Biofidelity of the SID-IIs and a modified SID-IIs upper extremity: biomechanical properties of the human humerus. In *Proc. of the 19th Int. Tec. Conf. on the Enhanced Safety of Vehicles* (No. 05-0123).

[13] Wang, Z. J., Lee, E., Bolte IV, J., Below, J., Loeber, B., Ramachandra, R., ... & Guck, D. (2018). Biofidelity Evaluation of THOR 5th Percentile Female ATD. In *Ircobi Conference, Athens/Greece*.

[14] Kuppa, S., Eppinger, R. H., Mckoy, F., Nguyen, T., Pintar, F. A., and Yoganandan, N. 2003. "Development of side impact thoracic injury criteria and their application to the modified ES-2 dummy with rib extensions (ES-2re)." SAE Technical Paper, No. 2003-22-0010

[15] Perez-Rapela, D., Donlon, J.P., Forman, J.L., Crandall, J.R., Pipkorn, B., Shurtz, B.K., and Markusic, C. 2019. "PMHS and WorldSID Kinematic and Injury Response in Far-Side Events in a Vehicle-Based Test Environment." Stapp Car Crash Journal, No. 63, 83-126

APPENDIX

Table A.
A Summary of the Common Injury Parameters Between IIHS Side Impact 1.0 and 2.0 Test and their Associated Injury Protection Ratings

Body Region	Parameter	IARV	IIHS Side Impact 1.0			IIHS Side Impact 2.0		
			Good/Acceptable	Acceptable/Marginal	Marginal/Poor	Good/Acceptable	Acceptable/Marginal	Marginal/Poor
Head and Neck	Head Injury Criterion (HIC) 15	779	623	779	935	623	779	935
	Neck Axial Tension (kN)	2.1	2.1	2.5	2.9	2.1	2.5	2.9
	Neck Compression (kN)	2.5	2.5	3.0	3.5	2.5	3.0	3.5
Torso	Average Rib Deflection (mm)	34	34	42	50	28	38	48
	Worst Rib Deflection (mm)	N/A	*	*	*	*	*	*
	Rib Deflection Rate (m/s)	8.20	8.20	9.84	11.48	8.2	9.8	11.5
	Viscous Criterion (m/s)	1.00	1.00	1.20	1.40	1.0	1.2	1.4
Pelvis	Combined Acetabulum and Ilium Force (kN)	5.1	5.1	6.1	7.1	4.0	5.0	6.0

EVALUATION OF THOR-50M, WORLDSID-50M AND GHBMC M50-O v6.0 MODLES IN FAR-SIDE CRASHES

Jay Zhao
Deepak Vasant Sabannavar
Mutaz Shkoukani
Joyson Safety Systems
United States

Paper Number 23-0283

ABSTRACT

This study is conducted to assess biofidelity of three occupant models (GHBMC human 50th%ile male occupant model M50-O v6.0, Humanetics male THOR dummy model v1.8.1 and WorldSid-50M model v7.6) in far-side crash test conditions and to better understand the kinematics and response of a far-side mid-sized driver in a compact size vehicle crashed to a 285° oblique right-side rigid pole at 31.01 km/h (NHTSA FMVSS 214 Test # 210915).

Far-side occupant simulations for various sled and vehicle crash tests have been conducted. Firstly, the GHBMC human body model (HBM) is correlated with the three post-mortem human subjects (PMHS) far-side sled tests performed by University of Virginia (UVA) [1] at two crash severities and two impact directions. Secondly, a series of the far-side sled test simulations with paired HBM and anthropomorphic test device (ATD) cases are conducted, varying with severities and impact directions, seats, and central console presence. Lastly, occupant simulations are performed for a belted far-side mid-size male driver, represented by the HBM and the WorldSid-50M model respectively, in the subject compact passenger car in the FMVSS 214 pole test. Comparative analysis is made for the kinematics and responses of the HBM and the WorldSid-50M model at the vehicle crash.

The HBM correlation results show that the GHBMC M50-O v6.0 human model reasonably correlates well with the PMHS kinematics and response from the 60-degree oblique far-side UVA sled tests. The HBM estimated high injury risk for the thorax is in line with the post-test PMHS injury outcomes.

The comparative HBM-ATD studies at both the far-side sled tests and the vehicle pole crash test indicate that both ATD models have positive and negative biofidelity outcomes compared to the HBM. The THOR dummy has similar head/neck/torso kinematic and response measures compared to the HBM under the oblique sled test conditions, while its pelvis and lower leg respond poorly to the lateral inertia loads. The WorldSid-M50 dummy model has the whole-body kinematics similar to the HBM under the oblique sled test conditions, while it shows stiffer lateral bending of the torso and smaller chest deflections than the HBM especially under the lateral far-side loadings.

The subject vehicle side crash test occupant simulation with the HBM predicts that the mid-size male driver may suffer severe injuries on the chest and moderate injuries on the head and abdomen.

INTRODUCTION

According to 2020 European New Car Assessment Programme (Euro NCAP) statements, side impacts account for around a quarter of all crashes. In a lateral/side impact, the occupants on both the struck (near) side and on the opposite (far) side of the vehicle are at risk of injury. Earlier study by Digges et al. [2] on the NASS/CDS 1988-98 indicated that fatality risk in far-side oblique collisions was comparable to that in near-side collisions. The head accounted for 45% of the MAIS 4+ injuries in far-side collisions and the chest/abdomen accounted for 39%. Yoganandan et al. [3] found that the abdominal injuries especially to the liver and spleen also occurred often in far-side collisions. Gabler et al. [4] investigated over 100 cases of Australian far side struck occupants from the MIDS database, and over 4500 cases of U.S. far side struck occupants from NASS/CDS 1993-2002. They found that far side struck occupants have a significant risk of injury in both Australia and the United States. As a fraction of all occupants who experienced a side impact, far side struck occupants accounted for approximately 20% of the

seriously injured persons and 25-29% of the Harm. Bahouth et al [5] studied the NASS CDS 2004-2013 data. The results indicated that far-side oblique collisions were the most common impact direction caused serious injuries. The chest/abdominal injuries accounted for 43% and head injuries accounted for 23% of the AIS 3+ injuries. Drivers accounted for 79% of the MAIS 3+ injured belted front outboard occupants that were involved in far-side crashes. About 53% of front outboard occupant's chest injuries were caused by contacts with the vehicle center stack or seat back and 21% were associated with contacts with the far-side structure. More than 60% of the AIS 3+ head injuries were caused by the far side structure. Of the far-side crash involved occupants analyzed, they sustained AIS3+ head or chest injuries from the far side of the vehicle more than 4.4 times more often than were attributed to occupant to occupant contact. Hostetler et al. [6] recently queried NASS/CDS 2000–2015 dababase resulted in 4495 non-weighted far-side crashes. For AIS 2+ through 5+ injury, the injury risks increased 2.48-3.66% per delta-V increase of 11.9 kph. Multiple impacts were significant factors on increased AIS 3+ through 5+ injuries. For AIS 2+ body region injuries, lateral delta-V and maximum CDC extent were positively associated with increased head, thorax, and lower extremity injury risk while belt use was associated with lower risk.

Far-side crashes are expected to increase in near future as more new automated vehicles (AV) are in the field. The trends in AV interior seating configurations bring more innovative and versatile design options than the conventional vehicles. Other than the traditional forward-facing seats, AV seating designs may have seating positions of oblique-facing, rear-facing, and side facing or the other angle-oriented. The oblique and side-facing seat positions will become far-side like collision environment in the frontal or side collisions observed often from the field.

Better protection of far-side occupants in crashes requires better test protocol and injury evaluation tools. Extensive reaserch and development have been conducted in the past decades. Recently, Euro NCAP [7] regulates a new far side occupant test & assessment procedure that details the assessments to be performed in far side occupant protection that contribute to the side impact part of the adult occupant protection rating. Far side protection is assessed using two sled tests that are representative of AE-MDB and Oblique Pole test configurations. One WorldSID 50th male dummy will be seated on the far side of the vehicle. In addition, data from full-scale testing is required to demonstrate head protection countermeasures for occupant-to-occupant interaction.

The advanced anthropomorphic test devices like WorldSID-50M dummy and THOR male dummy have been developed. Biofidelity of these ATDs are evaluated from various studies. Particularly for the far-side applications, Pintar et al. [8] performed far-side sled tests at both low (11 km/h) and high (30 km/h) velocities for six PMHS and the THOR and the WorldSID dummies. Their matched-pair comparisons for the kinematics and responses among post-mortem human subjects (PMHS), WorldSID, and THOR-NT indicated both positive and negative biofidelity outcomes for both the THOR and the WorldSID dummies in the far-side crash mode. Forman et al. [1] performed a series of far-side lateral and oblique sled tests with seven PMHS. With this set of test data biofidelity of GHBMC M50-O v4.4 model was assessed [11]. Biofidelity of the THOR 50th percentile male dummy was evaluated by Parent et al. [9] for the frontal impacts. However, its biofidelity particularly for the far-side applications are not yet fully understood. Rhule et al. [10] evaluated biofidelity of WorldSid-50M dummy using an updated biofidelity ranking system. The data showed that the WorldSID dummy demonstrated Internal Biofidelity values of 1.4 and External Biofidelity values of 2.2 (with Abdomen). For the body regions of thorax and pelvis, the WorldSID dummy received an overall external BioRank score of 3.2 and 2.7 respectively, indicative of improvement required for the pendulum force response measurement of the oblique pendulum impact test.

With the most recent advances in development of more biofidelic human occupant surrogates, new generation of human body models and FE models of advanced ATDs have been under development. The Global Human Body Model Consortium (GHBMC) has developed recently the 50th percentile male occupant model (named as GHBMC AM50-O v6.0). The Humanetics male THOR dummy model v1.8.1 and WorldSid-50M v7.6, validated with multiple component and system impact tests, have been used in the industry as the digital "twins" of the dummy hardware. Nevertheless, research questions as follows still remain:
1) Is biofidelity of the GHBMC AM50-O v6.0 HBM good for applications in far-side crashes?
2) How are the kinematics, responses and injury measures of Humanetics male THOR dummy model v1.8.1 comparable to the HBM at oblique far-side sled test conditions?
3) How are the kinematics, responses and injury measures of WorldSid-50M dummy model v7.6 comparable to the HBM at various far-side sled and vehicle crash test conditions?

This study is aimed to address those questions to assess and identify appropriate occupant model(s) for evaluation of restraint performance and far-side occupant's kinematics, responses, and injury risks.

METHODS

This study is conducted in three phases.

Phase 1: **HBM validation** to assess biofidelity of the HBM (GHBMC M50-O v6.0 model) via the model correlation with the far-side sled tests data provided by University of Virginia (UVA) [1].

Phase 2: **Far-side sled test occupant simulations** for parametric comparative analysis for a far-side mid-size male occupant at various sled test conditions. The two ATD models — Humanetics male THOR dummy model v1.8.1 and WorldSid-50M model v7.6 are compared respectively with the validated HBM from the results of ATD-HBM paired cases.

Phase 3: **Vehicle crash far-side occupant simulations** for the kinematics and responses of a far-side mid-size occupant in the subject compact passenger car right side pole crash, in which the kinematics and responses of WorldSid-50M model v7.6 are compared to the HBM.

HBM Correlation with PMHS Tests

To compare the GHBMC AM50-O v6.0 HBM to the PMHS in the far-side collisions, three UVA PMHS far-side sled tests [1] with variation of impact severity and angle are simulated. Table 1 lists the simulation matrix I for the HBM correlation with the UVA sled tests, in which the PMHS 602 was tested at 60-degree oblique loadings with the 14g and 6.6g pulses respectively, and the PMHS 559 was tested at the 90-degree loading with the 14g pulse.

Table 1.
Simulation matrix I: the UVA far-side sled tests for the HBM correlation

Case #	Case Name	Test Number	PMHS#	Delta V (km/h)	Impact Direction to Occupant	Pretensioner	Arm Position	D-ring Position
C1	HM134	S0134	602	15	60 Deg	Yes	Down	Intermediate
C2	HM135	S0135	602	32	60 Deg	Yes	Down	Intermediate
C3	HM091	S0091	559	32	90 Deg	Yes	Down	Intermediate

Table 2 summarizes information of the PMHS in the tests and the HBM in the simulations. The GHBMC AM50-O v6.0 model represents a male occupant of 77 kg weight, 175 cm tall and BMI of 25.1.

Table 2.
PMHS and GHBMC AM50-O v6.0 model information

Occupant	Mass (kg)	Stature (cm)	BMI	Age
PMHS-602 (oblique)	79	178	24.9	61
PMHS-559 (lateral)	73	175	23.8	60
GHBMC AM50-O	77	175	25.1	-

Figure 1 shows the HBM simulation model per the UVA PMHS far-side sled tests setup.
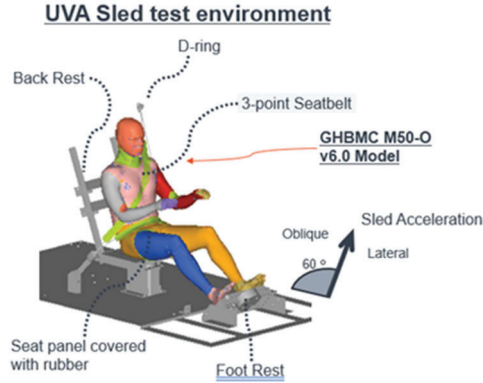
Figure 1. UVA PMHS far-side sled test model.

The base sled test model is from the validated one used in our previous study [11] for GHBMC M50-O v4.4 model. It consists of the FE models of the base sled, the base seat and the seatbelt that were built based on the physical geometries and properties of the UVA far-side sled test fixture [1]. The D-Ring position and the shoulder belt routing for the positioned HBM are set up per each the PMHS test.

In the update PMHS far-side sled test model, the GHBMC AM50-O v6.0 model is swapped in the base sled test model. The newly replaced HBM is individually positioned to match the initial locations of head, torso, pelvis, knee, and ankle targets of each PMHS in each test after performing a series of positioning pre-simulations that followed same procedure as the previous study [11]. Table 3 compares the initial positions between the HBM and the PMHS in terms of six position measurements in the sagittal plane: distance between H-point and the seat front edge; distance between D-ring to the seat front edge; angle between D-ring and left shoulder; angle between T3 and L1 (Torso Angle); angle between H-point and knee (Femur Angle); and angle between knee and ankle (Tibia Angle). All the measurements are matched well between the HBM and the PMHS except for the H-point to seat distance, for which matching H-point position is given a lower priority over matching the pelvis CG and head CG locations.

Table 3.
PMHS/HBM position measurements

Case #	Case Name	Subject	H-pt. to Seat (mm)	D-ring to Seat (mm)	Belt Angle (deg)	Torso Angle (deg)	Femur Angle (deg)	Tibia Angle deg)
C1	HM134	PMHS-602	119	525	44	80	14	43
		HBM 134	81	525	45	76	13	45
C2	HM135	PMHS-602	118	521	48	81	12	47
		HBM 135	81	521	45	76	13	45
C3	HM091	PMHS-559	118	521	48	81	12	47
		HBM 091	81	521	45	76	13	45

Far-side Sled Test Occupant Simulations
Specific purposes of this phase of study are defined as
- (i) to assess biofidelity of each ATD (the THOR-M50 and WorldSid-M50) by comparing the kinematics and responses to the HBM from each ATD-HBM paired case, and
- (ii) to evaluate trends of the kinematics and injury measures variation with various far-side sled test conditions.

Table 4 defines simulation matrix II for the ATD-HBM parametric comparative study. Twelve simulation cases in total are defined, among which Cases C2 and C3 belonging to the simulation matrix I (Table I) are included for completeness. There are seven paired ATD-HBM simulation cases defined below:
- (i) Cases C2-HM135 vs. C6-TR138 — paired HBM-THOR at the oblique sled with the UVA steel seat,
- (ii) Cases C4-HM136 vs. C7-TR139 — paired HBM-THOR at the oblique sled with the production seat,
- (iii) Cases C5-HM137 vs. C8-TR140 — paired HBM-THOR at the oblique sled with the production seat and a right-side console,
- (iv) Cases C2-HM135 vs. C9-WS141 —paired HBM-WORLDSID at the oblique sled with the UVA steel seat,

(v) Cases C4-HM136 vs. C10-WS142 — paired HBM-WORLDSID at the oblique sled with the production seat,

(vi) Cases C5-HM137 vs. C11-WS143 — paired HBM-WORLDSID at the oblique sled with the production seat and a right-side console, and

(vii) Cases C3-HM091 vs. C12-WS144 — paired HBM-WORLDSID at the 90 deg side sled with the UVA steel seat.

The simulation case setup with the UVA steel seat without seat console is per the UVA PMHS sled tests [1], for which Cases C2, C3, C6, C9, and C12 are included. For the other cases in the matrix II, the simulated sled test configurations for the seating environment are different from the UVA sled tests, where the steel seat is replaced a validated generic FE production seat model and presence of a generic console is considered.

Table 4.
Simulation matrix II: Far-side sled test simulation cases for ATD-HBM comparative analysis

Case #	Case Name	Crash Pulse or Condition	O-Model	Seat	Seat Console
C2	HM135	UVA Far side Oblique,14g	M50-O v6.0	UVA Steel Seat	No
C3	HM091	UVA Far side 90Deg,14g	M50-O v6.0	UVA Steel Seat	No
C4	HM136	UVA Far side Oblique,14g	M50-O v6.0	Production Seat	No
C5	HM137	UVA Far side Oblique,14g	M50-O v6.0	Production Seat	Yes
C6	TR138	UVA Far side Oblique,14g	THOR v1.8.1	UVA Steel Seat	No
C7	TR139	UVA Far side Oblique,14g	THOR v1.8.1	Production Seat	No
C8	TR140	UVA Far side Oblique,14g	THOR v1.8.1	Production Seat	Yes
C9	WS141	UVA Far side Oblique,14g	WSID v7.6	UVA Steel Seat	No
C10	WS142	UVA Far side Oblique,14g	WSID v7.6	Production Seat	No
C11	WS143	UVA Far side Oblique,14g	WSID v7.6	Production Seat	Yes
C12	WS144	UVA Far side 90Deg,14g	WSID v7.6	UVA Steel Seat	No
C13	WS145	UVA Far side 90Deg,14g	WSID v7.6	Production Seat	No

The HBM positioning at Cases C4 and C5 is same as C2, for which the position measurements are summarized in Table 3. The THOR dummy model positioned at Cases C6-C8 is set to match the HBM case C2 for the initial locations of head, torso, pelvis, knee, and ankle targets. The WorldSID dummy model positioned at Cases C9-C11 is per the HBM position C2 and positioned at C12-C13 is per the HBM position C3. Table 5 summarizes the (X, Y, Z) coordinates of the head CG, left and right shoulder, pelvis CG, left and right knee and ankle targets of the HBM, THOR, and WorldSID dummy models for all the cases listed in Table 4.

Table 5.
Coordinates (X, Y, Z) of the positioning targets of the occupant models in Cases C2-C13

O-Model	Case Name	Head CG (X,Y,Z)	Left Shoulder Target (X,Y,Z)	Right Shoulder Target (X,Y,Z)	Pelvis CG (X,Y,Z)	Left Knee Target (X,Y,Z)	Right Knee Target (X,Y,Z)
M50-O v6.0	HM135, HM136, HM137	(-103, 0, -761.8)	(-103, -234, -492)	(-103, 234, -492)	(-1, 0, -95)	458, -205, -146)	(458, 205, -146)
THOR v1.8.1	TR138, TR139, TR140	(-101, 0, -782)	(-104, -235, -538)	(-104, 235, -538)	(-48, 0, -92)	(456, -200, -149)	(456, 200, -149)
WSID v7.6	WS141, WS142, WS143	(-87, 0, -759)	(-126, -245, -507)	(-126, 245, -507)	(-81, 0, -92)	(460, -217, -194)	460, 217, -194)
M50-O v6.0	HM091	(-88, 0, -769)	(-109, -237, -492)	(-109, 237, -492)	(-132, 0, -91)	(413, -190, -147)	(413, 190, -147)
WSID v7.6	WS144, WS145	(-86, 0, -761)	(-138, -245, -511)	(-138, 245, -511)	(-98, 0, -108)	(435, -203, -167)	(435, 203, -167)

Figure 2 shows three sled test simulation models variants with each of the occupant models – the HBM, the THOR model v1.8.1 and the WorldSid model v7.6.
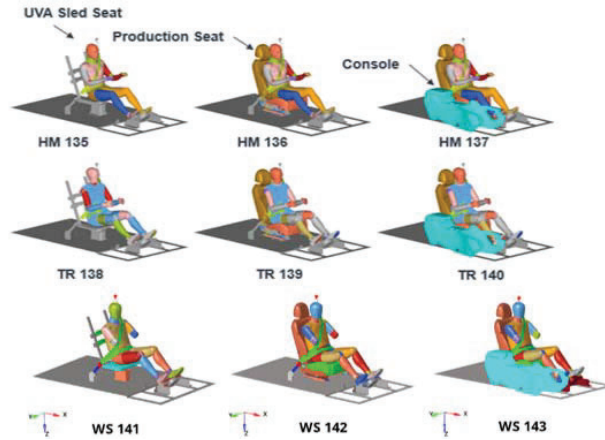
Figure 2. HBM/ATD far-side sled test simulation models setup.

Vehicle Crash Far-side Occupant Simulations

The simulated subject vehicle was a compact passenger car crashed in the FMVSS 214 rigid pole right side impact test conducted by the Transportation Research Center Inc. in East Liberty, Ohio, USA on September 15, 2021 (NHTSA test# 210915). In the test the vehicle was towed into the rigid pole at an angle of 285° with a velocity of 31.01 km/h.

A 2010 Toyota Yaris FE model is downloaded from crash simulation vehicle models database managed by National Crash Analysis Center (NCAC). This FE vehicle model is then updated to represent the subject vehicle. Modifications are made for the exterior and interior body parts (such as body, door and door trims etc.), morphed based on the reported pre-test dimension measurement data from the test for the case vehicle. The maximum deformation of right-side door and door-trims are profiled per the post-test measured right-side door intrusion data. The 1st row seatbelt/pretensioner and anchorage attachments and the driver and passenger seats are represented by the same FE component models used in the sled test simulations in the matrix II, while the 2nd row seat is not included. The driver and passenger seats are repositioned per the reported seat measurement data from the test. The subject vehicle CG location and value are adjusted to match the measurement data from the test. The measured vehicle CG three-dimensional accelerations and vehicle pitch, yaw and roll velocities from the test are imposed by prescribed motion to the subject vehicle model.

The other interior parts surround the 1st row occupants, specifically the full facia assembly consisting of the facia, steering column, and steering wheel as well as the knee bolsters and floors, remain same as the original vehicle model. The full tunnel/central console components consisting of the full tunnel trim, hand brake assembly, gear lever assembly and storage compartments from the original vehicle model are labeled as the "Center Console 1" option for the evaluation.

The simulated far-side occupant is a mid-sized male occupant seating on the driver side, represented by the GHBMC M50-O v6.0 HBM and the Humanetics WorldSid-50M dummy model v7.6 respectively. Each occupant model is positioned same in the vehicle per the reported dummy's longitudinal and lateral clearance dimensions measurement from the test.

Table 6 defines simulation matrix III including two far-side occupant simulation cases for the subject vehicle pole crash.

Table 6.
Simulation matrix III: Cases for the far-side occupant in the subject compact car from NHTSA FMVSS214 pole crash test

Case #	Case Name	LHS Occupant	Seat	Center Console	Far-side AB
C14	HM146	HBM v6.0	Production Seat	Center Console 1	None

| C15 | WS147 | WSID v7.6 | Production Seat | Center Console 1 | None |

Figure 3 shows the far-side occupant simulation model with the subject vehicle for the two cases.

Whole vehicle model view
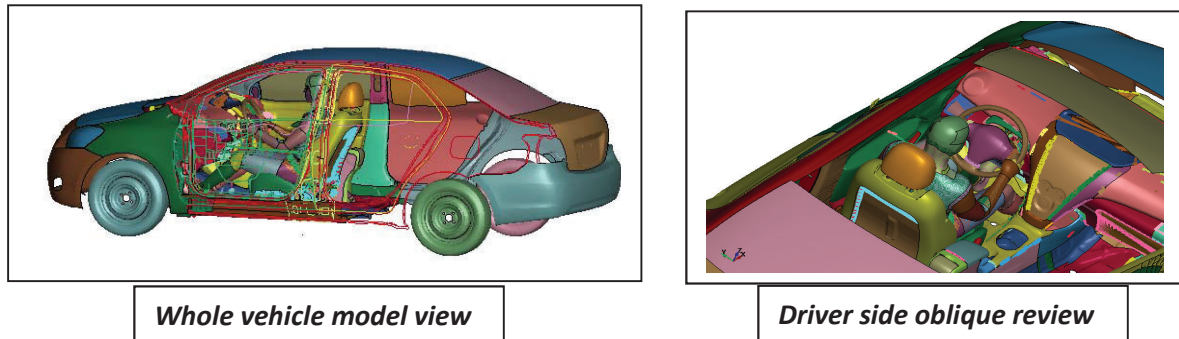

Driver side oblique review

Figure 3. The far-side occupant simulation models for the two cases of the subject vehicle right side pole crash.

Data Analysis and Processing

The data processing and analysis are performed for all the simulation cases for the three occupant models of GHBMC M50-O model v6.0, Humanetics THOR model v1.8.1, and Humanetics WorldSid-50M model v7.6.

The following outputs and measurements are processed for both the HBM and the ATD models:
- the head CG accelerations and rotational velocities,
- the forces and moments of the upper neck, lower neck and spine (T12),
- the shoulder forces and shoulder rib deflections (for WorldSID and HBM),
- the accelerations of T1, T4, T12 and pelvis CG,
- the chest and abdomen deflections at all the measurement locations of each ATD (THOR or WorldSID and comparable outputs from the HBM),
- the forces and moments of the pubic, acetabulum, and the left & right femur,
- the relative displacements (to the seat) of the kinematics targets or Vicon targets of the head, left and right shoulder (acromion), T1, T4, T12, pelvis, left and right knees.

The response and injury measures are normalized with the normalization values in Table 7 that are defined for the HBM and the ATDs separately based on the criterion that each pair of the HBM-ATD have about same estimated injury risk for same body region.

Table 7.
Normalization Values for HBM/THOR/WorldSID Injury Measures

Body Region	Measure	HBM Normalization Value	Risk	THOR Normalization Value	Risk	WSID Normalization Value	Risk
Head	HIC15	800	15%	800	15%	800	15%
	BrIC	1	56%	1	56%	1	56%
Neck	NIJ (Upper)	1	35%	1.3	34%	1	35%
	NIJ (Lower)	1	NA	1.5	NA	1.5	NA
	Tension (Upper) (kN)	4.17	25%	4.17	NA	4.17	NA
	Extension (Upper) (Nm)	25	NA	35	NA	35	NA
	Lateral Bend (Upper) (Nm)	100	NA	150	NA	150	NA
	Tension (Lower) (kN)	4.17	NA	4.17	NA	4.17	NA
	Extension (Lower) (Nm)	25	NA	35	NA	35	NA
	Lateral Bend (Lower) (Nm)	100	NA	150	NA	150	NA
Thorax	T4 G 3ms (G)	60	NA	60	NA	60	NA
	L Shoulder Joint Force (kN)	2	NA	2.25	NA	2.25	48%
	R Shoulder Joint Force (kN)	2	NA	2.25	NA	2.25	48%
	L Shoulder Rib Def (mm)	68	51%	--	NA	40	51%
	R Shoulder Rib Def (mm)	68	51%	--	NA	40	51%
	L. Upper Chest Def (mm)	68	51%	52	51%	40	51%

	R. Upper Chest Def (mm)	68	51%	52	51%	40	51%
	L. Mid Chest Def (mm)	68	51%	--	51%	40	51%
	L. Low Chest Def (mm)	68	51%	52	51%	40	51%
	R. Mid Chest Def (mm)	68	51%	--	51%	40	51%
	R Low Chest Def (mm)	68	51%	52	51%	40	51%
Abdomen	L Upper ABD Def (mm)	75	48%	95	46%	50	48%
	R Upper ABD Def (mm)	75	48%	95	46%	50	48%
	L Low ABD Def (mm)	75	48%	NA	46%	50	48%
	R Low ABD Def (mm)	75	48%	NA	46%	50	48%
Pelvis	Pubic Force (kN)	3.1	49%	--	NA	2.35	49%
	L. Accetab Force (kN)	3.45	NA	3.45	48%	6	NA
	R. Accetab Force (kN)	3.45	NA	3.45	48%	6	NA
Knee-Thigh	L. Femur Force (kN)	14	40%	10	43%	10	43%
	R. Femur Force (kN)	14	40%	10	43%	10	43%

The injury risks for the body regions of head, neck, thorax, abdomen, pelvis, and knee-thigh are calculated separately for the 50th%ile male HBM, WorldSID-50M, and THOR using the published injury risk functions [12-20] tabulated in Table A-1, A-2 & A-3 in Appendix A, respectively.

The Occupant Injury Measure (OIM_{AIS3+}^{ATD}) for the AIS 3+ injury risk estimated from the ATDs or HBM was calculated by (1)

$$OIM_{AIS3+}^{ATD} = 1 - (1 - P_{HIC}) * (1 - P_{BrIC}) * \left(1 - Max(P_{NIJ}, P_{NeckFz+}, P_{NeckFz-})\right) * (1 - P_{ChCD}) * \left(1 - P_{ABDef}\right) * \\ (1 - P_{PeivisF}) * (1 - P_{FemurF})$$

(Equation 1)

where P_{HIC}, P_{BrIC}, P_{NIJ}, $P_{NeckFz+}$, $P_{NeckFz-}$, P_{ChCD}, P_{ABDef}, $P_{PeivisF}$, P_{FemurF} are the AIS 3+ injury probabilities calculated with the measures of Head Injury Criterion (HIC15) and Brain Injury Criterion (BrIC), Neck Injury Criterion (NIJ) and Neck Tension Forces, Chest Deflections, Abdomen Deflections, Pelvic Forces, and Femur Force, respectively.

RESULTS

HBM Test Correlation Results

Case C1: HM134 with 6.6g pulse at 60-deg
Figure 5 shows snapshots of the GHBMC M50-O model v6.0 HBM kinematics compared to the PMHS -602 video from the UVA far-side sled test S0134 (6.6g pulse in 60deg). The kinematics of the HBM is similar to the PMHS.
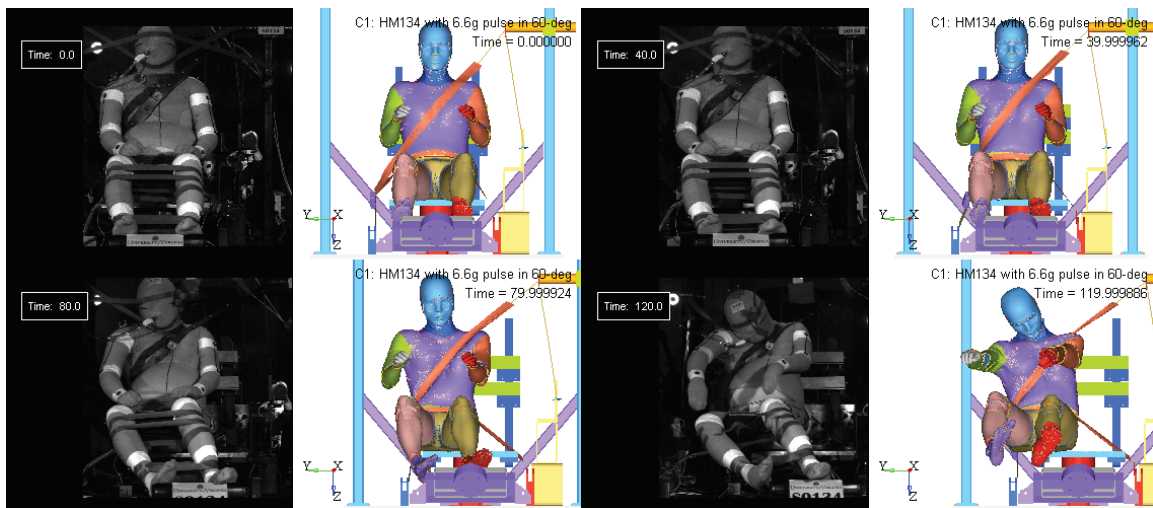

Figure 5. Snapshots of the GHBMC M50-O model v6.0 kinematics compared to the PMHS -602 video from the UVA sled test S0134 (6.6g pulse at 60deg) at 0msec, 40msec, 80 msec, and 120msec (Courtesy: The PMHS test data provided by UVA).

Figure 6 shows correlations of the time-histories of the responses and kinematics target displacements (relative to the seat) of the GHBMC M50-O model v6.0 against the measured censor signals and Vicon data of PMHS -602 from the UVA oblique far-side sled test S0134 (6.6g pulse at 60deg). Good correlations are seen for this sled test condition.
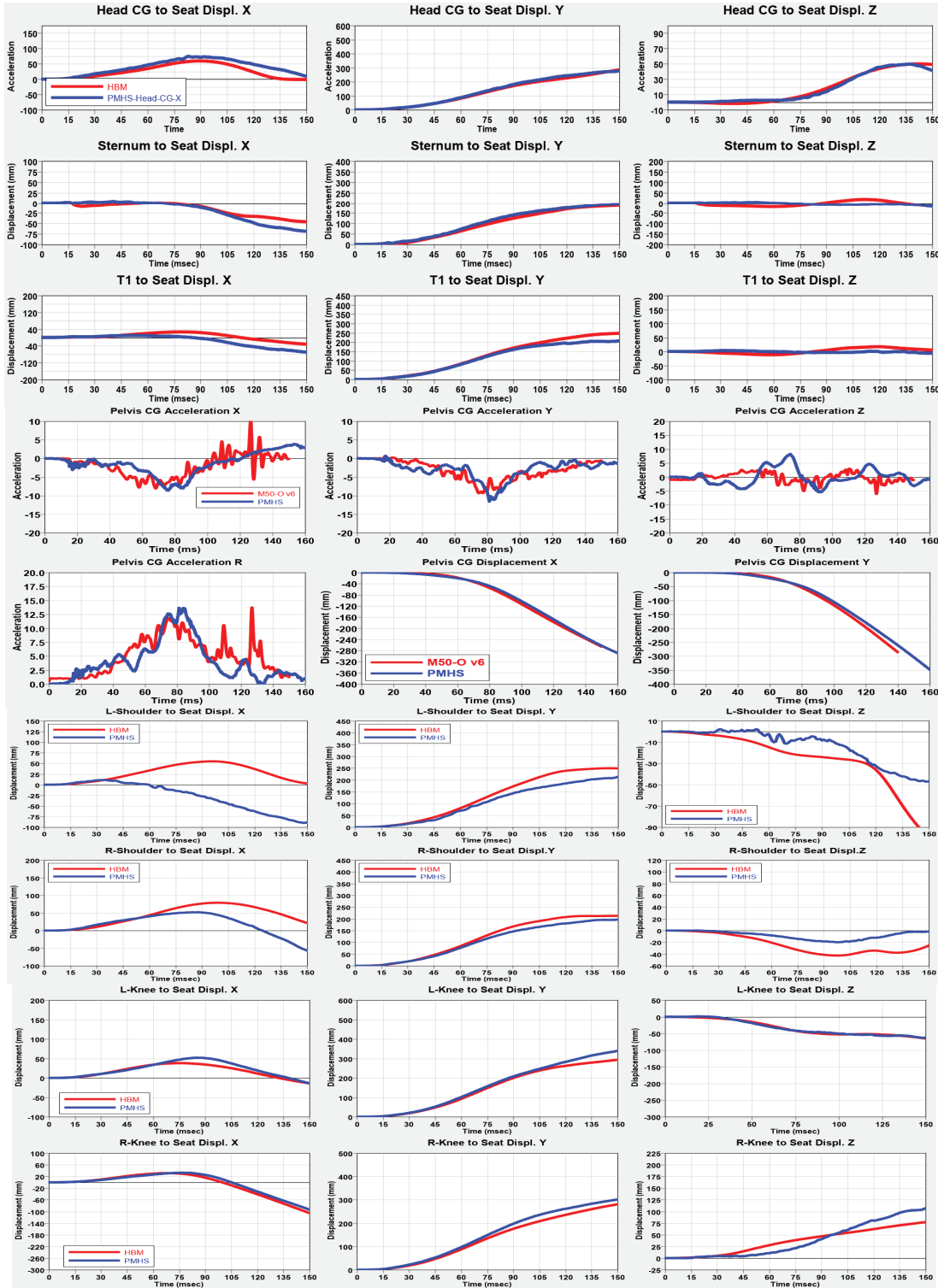
Figure 6. The time-histories of responses and kinematics target displacements of the GHBMC M50-O model v6.0 (red curve) compared to the test data of PMHS -602 (blue curve) from the UVA oblique far-side sled test S0134 (6.6g pulse at 60deg). (Courtesy: The PMHS test data provided by UVA).

Case C2: HM135 with 14g pulse at 60-deg

Figure 7 compares snapshots of the HBM kinematics to the PMHS -602 video from the UVA far-side sled test S0135 (14g pulse in 60deg) at 0msec, 40msec, 80msec and 120msec. The HBM kinematics looks like the PMHS for this test condition as well.
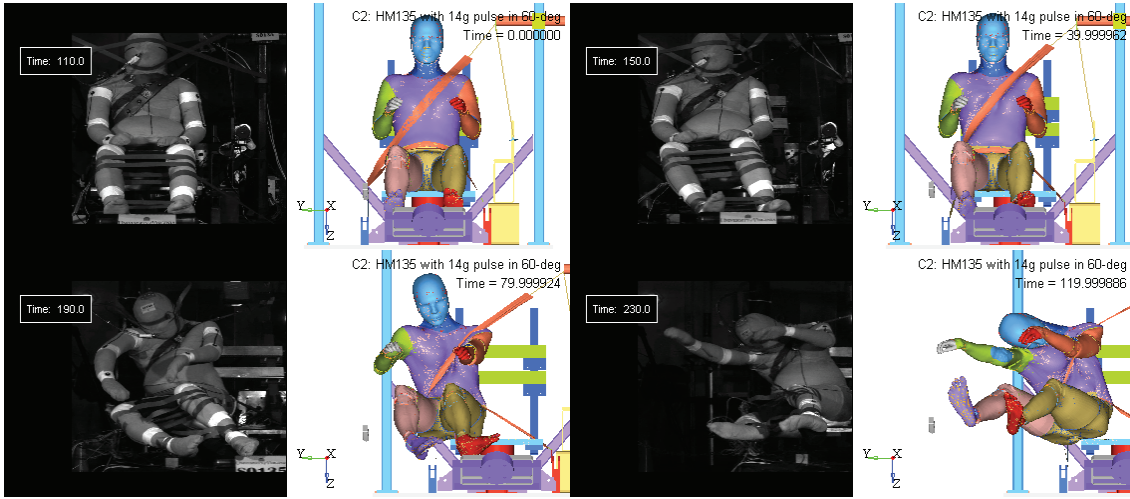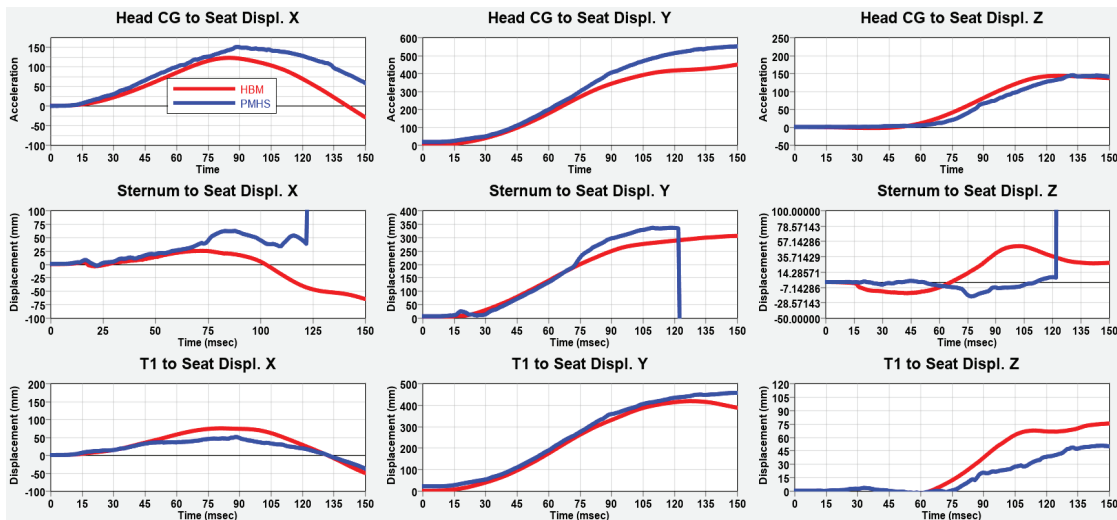

Figure 7. Snapshots of the GHBMC M50-O model v6.0 kinematics compared to the PMHS -602 video from the UVA sled test S0135 (14g pulse at 60deg) at 0msec, 40msec, 80 msec, and 120msec (Courtesy: The PMHS test data provided by UVA).

Figure 8 shows the time-histories of the relative displacements of the HBM head, sternum, T1, pelvis, left and right shoulders and knees compared to the Vicon data of PMHS -602 from the UVA oblique far-side sled test S0135 (14 pulse in 60deg). Overall, the HBM target displacements are close to the PMHS.
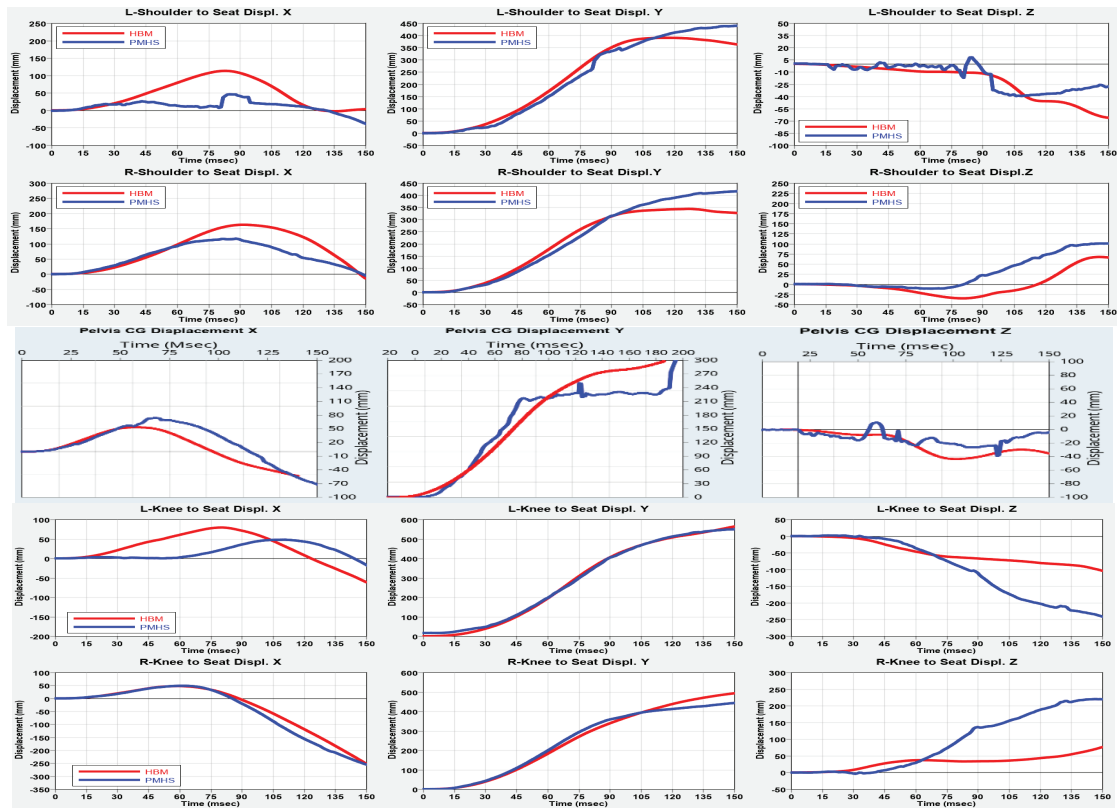
Figure 8. The time-histories of kinematics target relative-to-seat displacements of the GHBMC M50-O model v6.0 (red curve) compared to the test data of PMHS -602 (blue curve) from the UVA oblique far-side sled test S0135 (14g pulse at 60deg). (Courtesy: The PMHS test data provided by UVA).

Case C3: HM091 with 14g pulse in 90-deg

Figure 9 shows snapshots of the GHBMC M50-O model v6.0 kinematics compared to the PMHS -559 video from the UVA lateral far-side sled test S0091 (14 pulse in 90deg) at 0msec, 40msec, 80msec and 120msec.
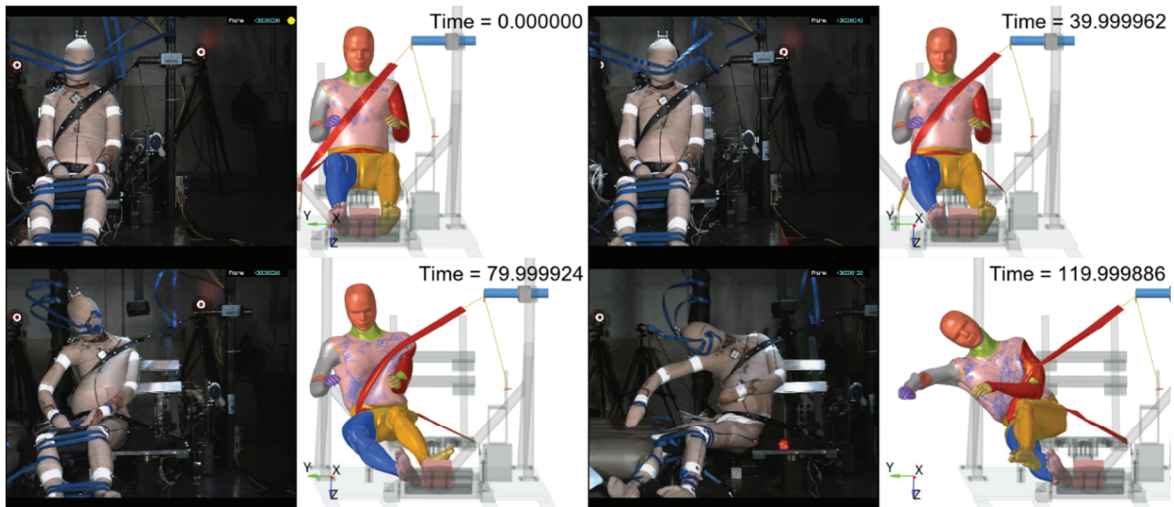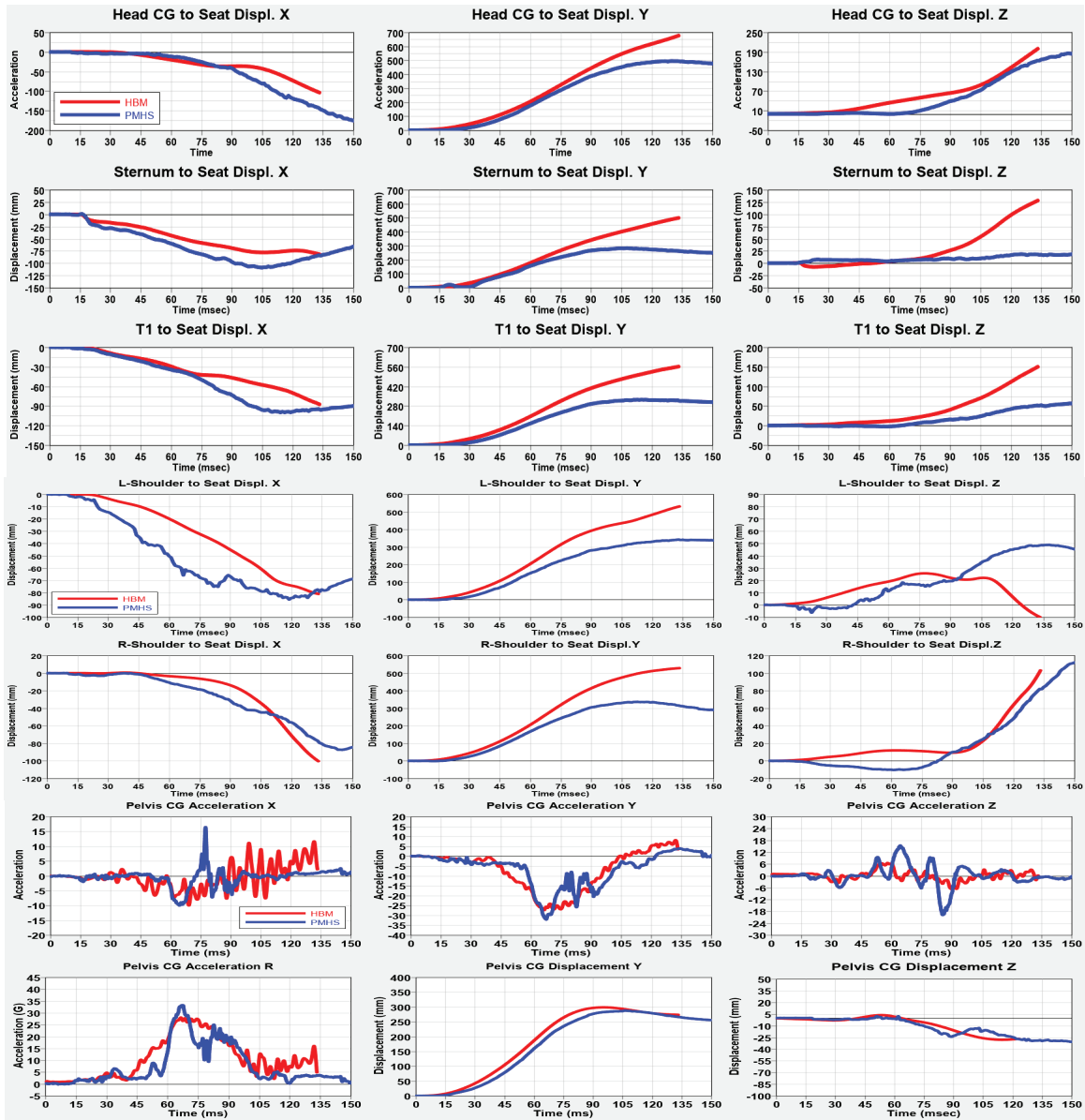

Figure 9. Snapshots of the GHBMC M50-O model v6.0 kinematics compared to the PMHS -559 test video from the UVA lateral sled test S0091 (14g pulse at 90deg) at 0msec, 40msec, 80 msec, and 120msec (Courtesy: The PMHS test data provided by UVA).

Figure 10 shows the time-histories of the responses and kinematics target relative-to-seat displacements of the GHBMC M50-O model v6.0 compared to the Vicon data of PMHS -559 in the UVA lateral far-side sled test S0091 (14g pulse in 90deg). It is seen from Figure 8 & 9 that the HBM kinematics is like the PMHS until ~80 msec. After then, the HBM has more lateral bending movement of the head/neck/torso compared to the PMHS mainly due to the seatbelt slipping down the HBM upper body after ~90msec. The difference of the body shape especially the abdomen between the PMHS -559 and the HBM is a major cause for the seatbelt loading path change. The fat abdomen of the PMHS holds the belt along the upper body longer.
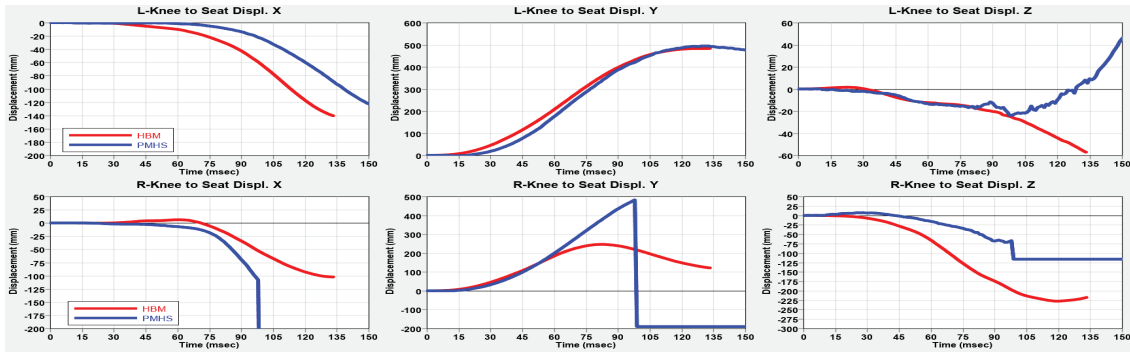
Figure 10. The time-histories of responses and kinematics target relative displacements of the GHBMC M50-O model v6.0 (Red curve) compared to the test data of PMHS -559 (Blue curve) from the UVA lateral far-side sled test S0091 (14g pulse at 90deg). (Courtesy: The PMHS test data provided by UVA).

Far-side Sled Test Occupant Simulations Results

Table B-1 in Appendix B lists the raw data of calculated responses and injury measures for all the sled simulation cases (C1 through C13) in matrix I & II with the three occupant models (GHBMC AM50-O v6.0 HBM, Humanetics WorldSid-50M model v7.6 & THOR model v1.8.1). Table B-2 in Appendix B summarizes the maximum relative-to-seat displacements of the kinematics targets of head, T1, T4, T12, pelvis, left and right shoulders and knees of those cases. Detailed data analysis results are presented in the following sub-sections.

THOR-HBM comparative analysis

Figure 11 shows snapshots of the GHBMC M50-O model v6.0 HBM kinematics at 0msec, 40msec, 80msec, and 150msec from the simulated sled test case (C2-HM135 in Table 4) with the steel seat in comparison to the paired THOR dummy case C6-TR138 (Table 4) at the 60 deg oblique sled test with 14g pulse, where the green is for the Thor dummy and the yellow for the HBM. It is seen that the Thor dummy has similar kinematics of the head/neck/torso but different lower legs movement compared to the HBM. The THOR pelvis and lower legs has much less lateral swing and upward movement than the HBM after ~80 msec.
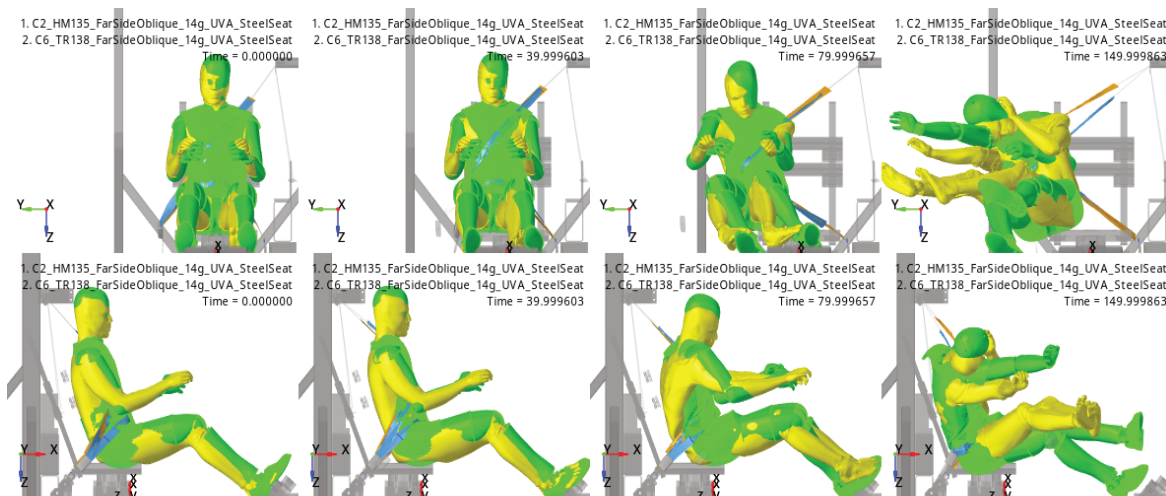

Figure 11. Snapshots of the kinematics of GHBMC M50-O model v6.0 from the simulated 14g 60 deg oblique far-side UVA sled test case C2-HM135 compared to the paired THOR dummy case C6-TR138. (Green: the Thor dummy; Yellow: the HBM).   .

Figure 12. Snapshots of the kinematics of GHBMC M50-O model v6.0 from the simulated 14g 60 deg oblique far-side sled test with the production seat (case C4-HM136) compared to the paired THOR dummy case C7-TR139. (Green: the THOR dummy; Yellow: the HBM).   .

The similar kinematics behavior of the THOR dummy is also shown in the 60 deg oblique sled test with 14g pulse with the production seat. Figure 12 shows snapshots of the GHBMC M50-O model v6.0 HBM kinematics at 0msec, 40msec, 80msec, and 150msec from the simulated sled test case C4-HM136 (Table 4) in comparison to the paired THOR dummy case C7-TR139 (Table 4).

More kinematics comparisons are made for the lateral relative-to-seat displacements of the body targets. Figure 13 compares the maximum relative-to-seat Y-displacements of the head, T1, T4, T12, pelvis, and left and right shoulders and knees between the THOR (in green) and the HBM (in yellow) for the three paired cases—C2-HM135/C6-TR138 with the UVA steel seat, C4-HM136/C7-TR139 with the production seat, and C5-HM137/C8-TR140 with the production seat and console. Under the three sled conditions, the THOR head/neck/torso moved laterally slightly more than the HBM while its lower legs lateral displacements were smaller.
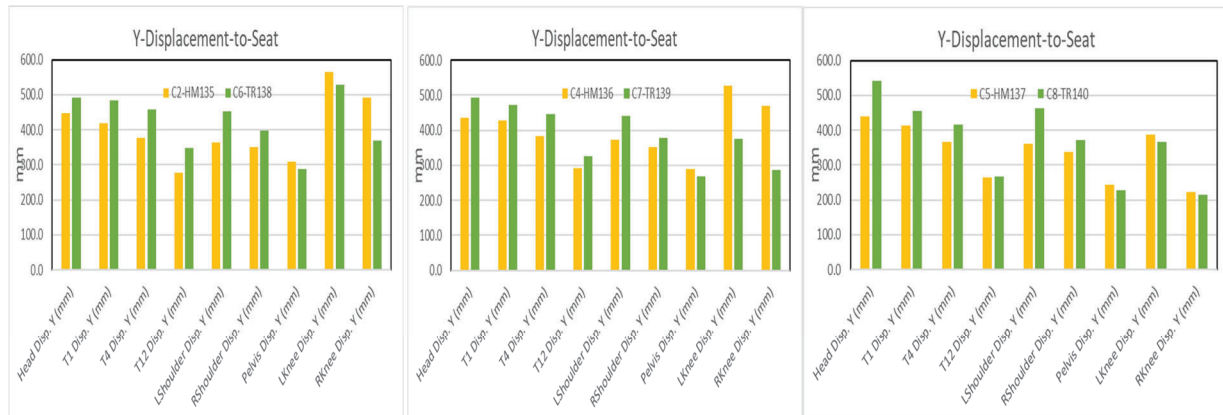

Figure 13. Comparison of the maximum relative lateral Y-displacements of the head, T1, T4, T12, pelvis, and left and right shoulders and knees between the THOR and the HBM for the three paired cases—C2-HM135/C6-TR138 with the UVA steel seat, C4-HM136/C7-TR139 with the production seat, and C5-HM137/C8-TR140 with the production seat and console. (Green: the THOR dummy; Yellow: the HBM).

Figure 14 compares the normalized responses and injury measures between the GHBMC M50-O model v6.0 HBM and the THOR dummy v1.8.1 for the three THOR-HBM paired cases. Compared to the HBM, the THOR has slightly higher BrIC and acetabulum forces while the other measures are close to the HBM for all the three cases.
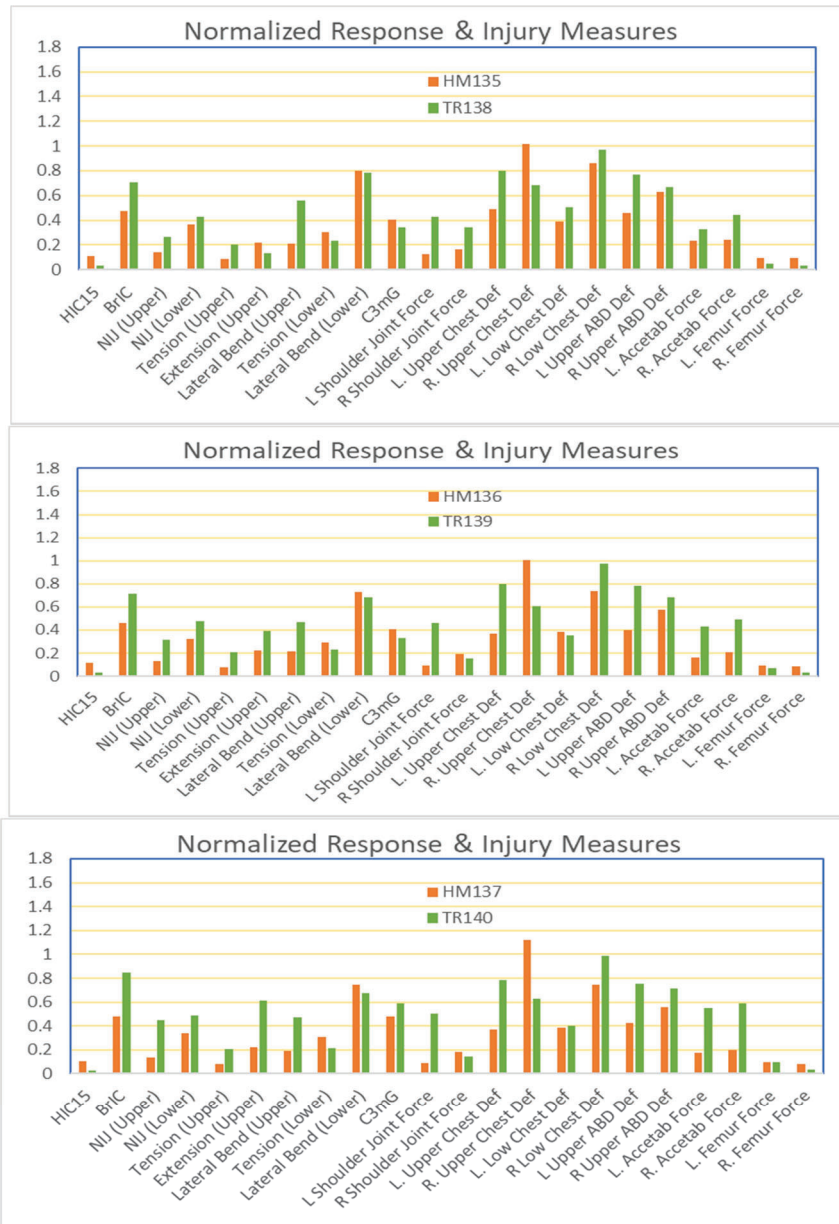
Figure 14. Comparison of the normalized responses and injury measures between the GHBMC M50-O model v6.0 and the THOR dummy model v1.8.1 for the three paired cases—C2-HM135/C6-TR138 with the UVA steel seat, C4-HM136/C7-TR139 with the production seat, and C5-HM137/C8-TR140 with the production seat and console. (Green: the THOR dummy; Yellow: the HBM).

Table 8 summarizes the calculated injury risks of the body regions of head, neck, thorax, abdomen, pelvis, and knee-thigh from the simulated far-side sled tests for the three paired THOR-HBM cases. The three THOR cases (TR138, TR139, TR140) are evaluated with the THOR model v1.8.1, and the HBM cases (HM135, HM136, HM137) are with the GHBMC M50-O model v6.0. Both the HBM and THOR models predict the highest injury risk for the chest, followed by high risks for the abdomen and pelvis regions. As the impact to the console where is at presence, the THOR model shows higher pelvis injury risk while the HBM has higher abdomen injury risk.

Figure 15. Snapshots of the kinematics of GHBMC M50-O model v6.0 from the simulated 14g 60deg oblique far-side steel seat sled test case C2-HM135 compared to the paired WORLDSID-50M dummy case C9-WS141. (Blue: the WorldSid-50M dummy; Yellow: the HBM).

Figure 16 shows snapshots of the GHBMC M50-O model v6.0 HBM kinematics at 0msec, 40msec, 80msec, and 150msec for the simulated sled test case C4-HM136 (Table 4) in comparison to the paired WORLDSID-50M dummy case C10-WS142 (Table 4) for the 60 deg oblique UVA sled test with 14g pulse with the production seat. The ATD-HBM kinematics differences are observed for this sled condition as well.

Figure 16. Snapshots of the kinematics of GHBMC M50-O model v6.0 in the simulated 14g 60deg oblique far-side production seat sled test case C4-HM136 compared to the paired WORLDSID-50M dummy case C10-WS141. (Blue: the WorldSid-50M dummy; Yellow: the HBM).

Figure 17 shows snapshots of the GHBMC M50-O model v6.0 HBM kinematics at 0msec, 40msec, 80msec, and 150msec from the simulated sled test case C5-HM137 (Table 4) in comparison to the paired WORLDSID-50M dummy case C11-WS143 (Table 4) for the 60 deg oblique UVA sled test with 14g pulse with the production seat and side console. With presence of the side console the WorldSID has more lateral bending movement but is still behind the HBM.
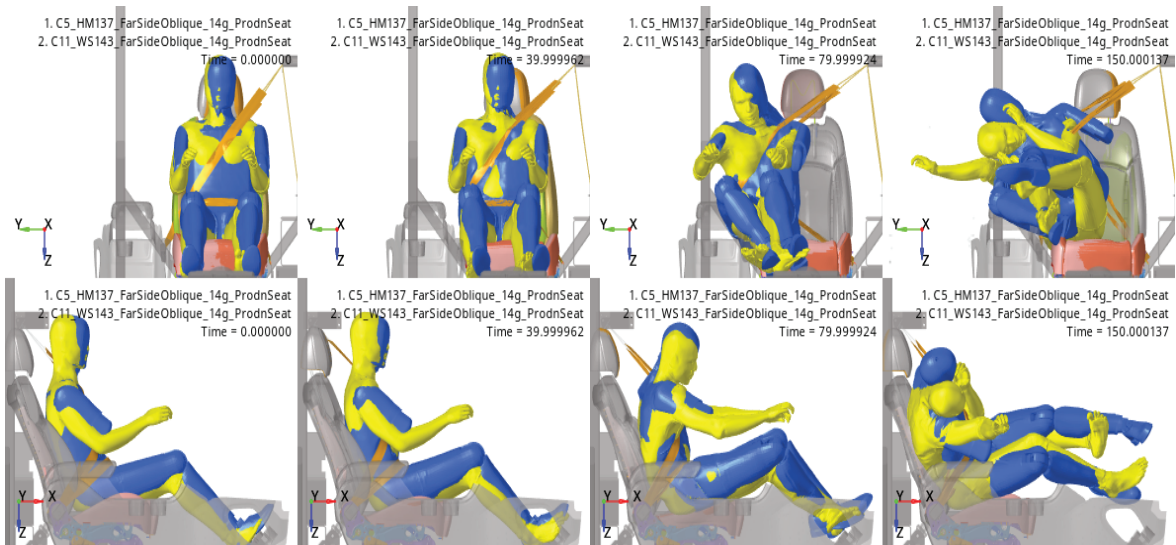
Figure 17. Snapshots of the kinematics of GHBMC M50-O model v6.0 in the simulated 14g 60deg oblique production seat/console sled test case C5-HM137 compared to the paired WORLDSID-50M dummy case C11-WS143. (Blue: the WorldSid-50M dummy; Yellow: the HBM)

Figure 18 shows snapshots of the GHBMC M50-O model v6.0 HBM kinematics at 0msec, 40msec, 80msec, and 140msec from the simulated sled test case C3-HM091 (Table 4) in comparison to the paired WORLDSID-50M dummy case C12-TR144 (Table 4) for the 90 deg lateral UVA steel sled test with the 14g pulse. Under such a lateral loading, the HBM has significantly more lateral torso bending and lateral head/neck excursion movement than the WorldSID dummy after ~70ms.
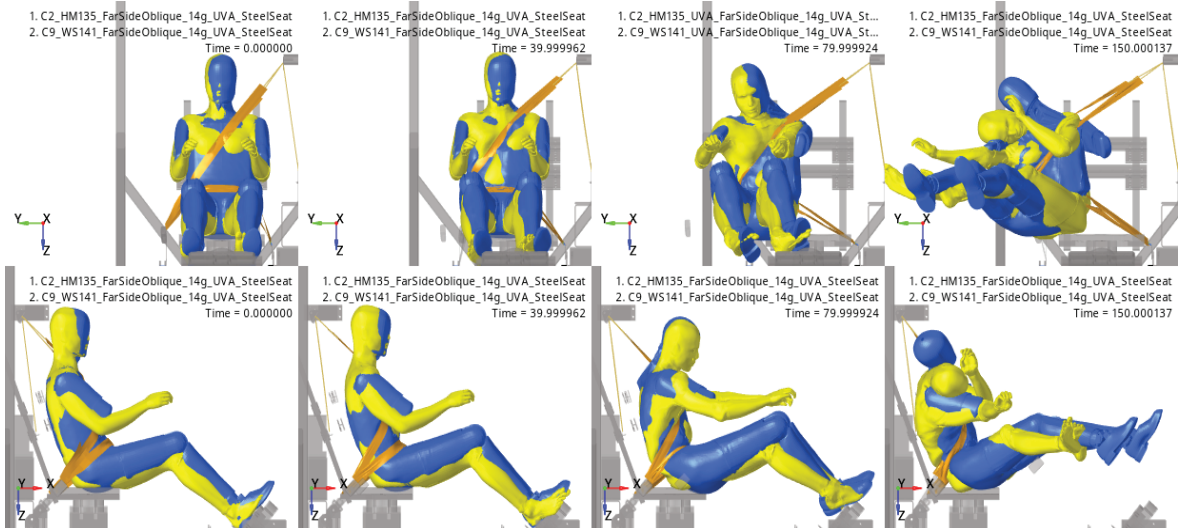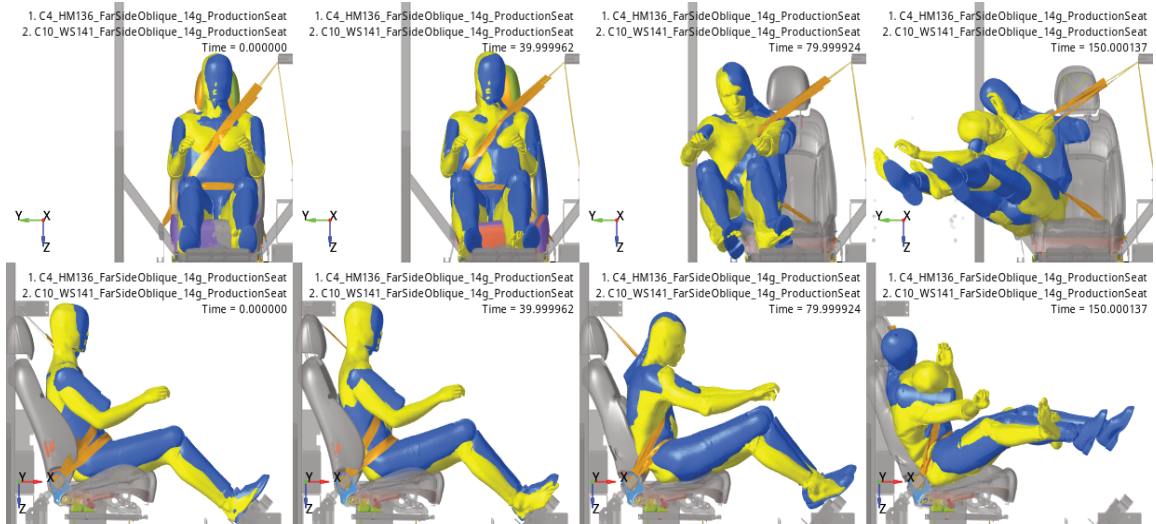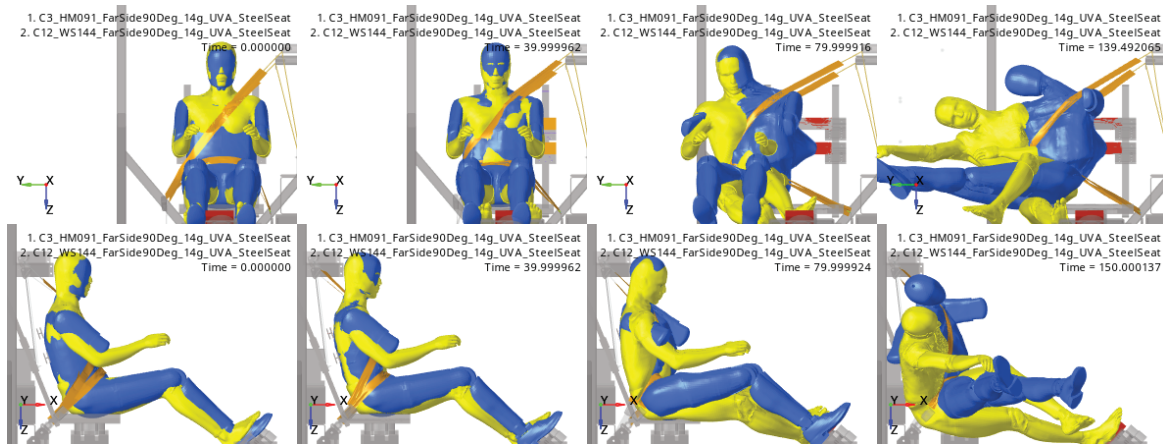
Figure 18. Snapshots of the kinematics of GHBMC M50-O model v6.0 in the simulated 14g 90deg lateral steel seat sled test case C3-HM091 compared to the paired WORLDSID-50M dummy case C12-WS144. (Blue: the WorldSid-50M dummy; Yellow: the HBM)

Figure 19 compares the maximum relative-to-seat lateral Y-displacements of the head, T1, T4, T12, pelvis, and left and right shoulders and knees between the WORLDSID and the HBM for the four paired cases (C2-HM135/C9-WS141, C4-HM136/C10-WS142, C3-HM091/C12-WS144, and C5-HM137/C11-WS143). It is seen that for the three 60 deg oblique sled test conditions (C2-C9, C4-C10, C4-C11) the maximum lateral displacements of the WORLDSID's head/neck/torso are close to the HBM, while the knees move laterally more than the HBM. For the 90deg side sled test conditions (C3-C12), however, the lateral displacements of the head/neck/torso of the WORLDSID are significantly smaller than the HBM, indicated a stiffer spine of the WORLDSID responding to the lateral loading.
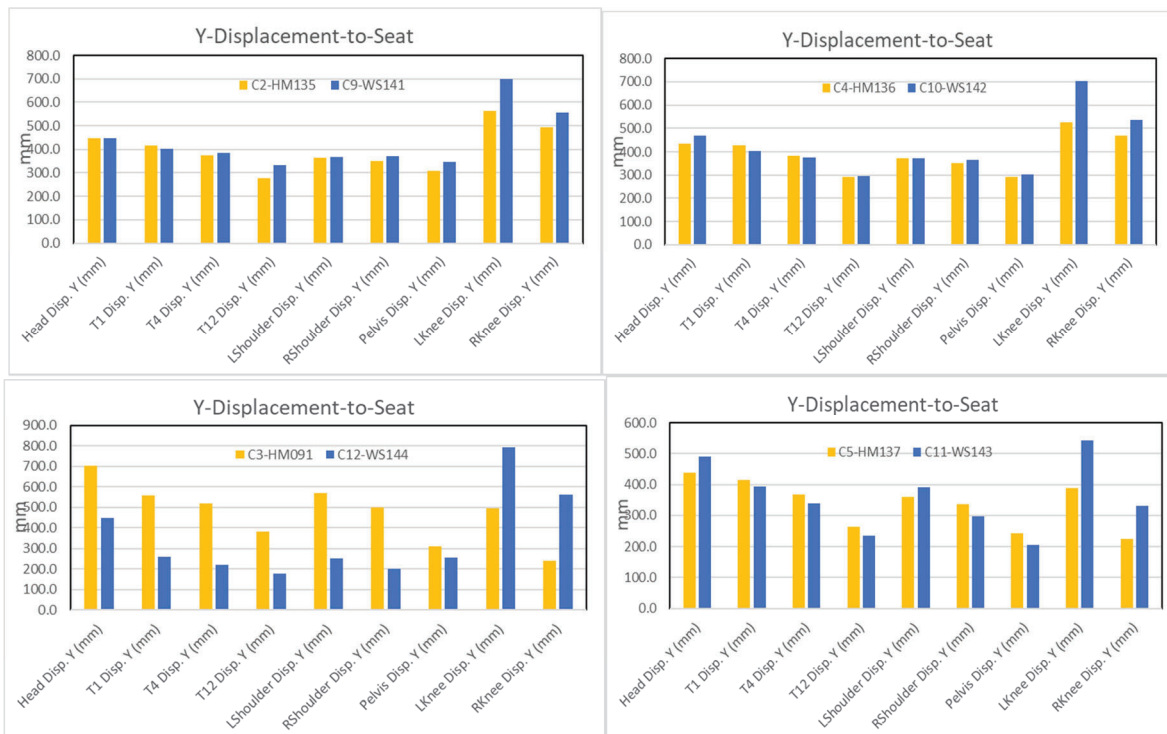
Figure 19. Comparison of the maximum relative-to-seat Y-displacements of the head, T1, T4, T12, pelvis, and left and right shoulders and knees between the THOR and the HBM of the four paired cases (HM135-WS141, HM136-WS142, HM137-WS143, HM091-WS144). (Blue: the WORLDSID dummy; Yellow: the HBM)

Figure 20 compares the normalized responses and injury measures between the GHBMC M50-O model v6.0 HBM and the WORLDSID dummy model v7.6 for the four paired cases (C2-HM135/C9-WS141, C4-HM136/C10-WS142, C3-HM091/C12-WS144, and C5-HM137/C11-WS143). It is seen that the chest/abdomen deflections of the WORLDSID are lower than the HBM for all the four simulated sled test conditions.
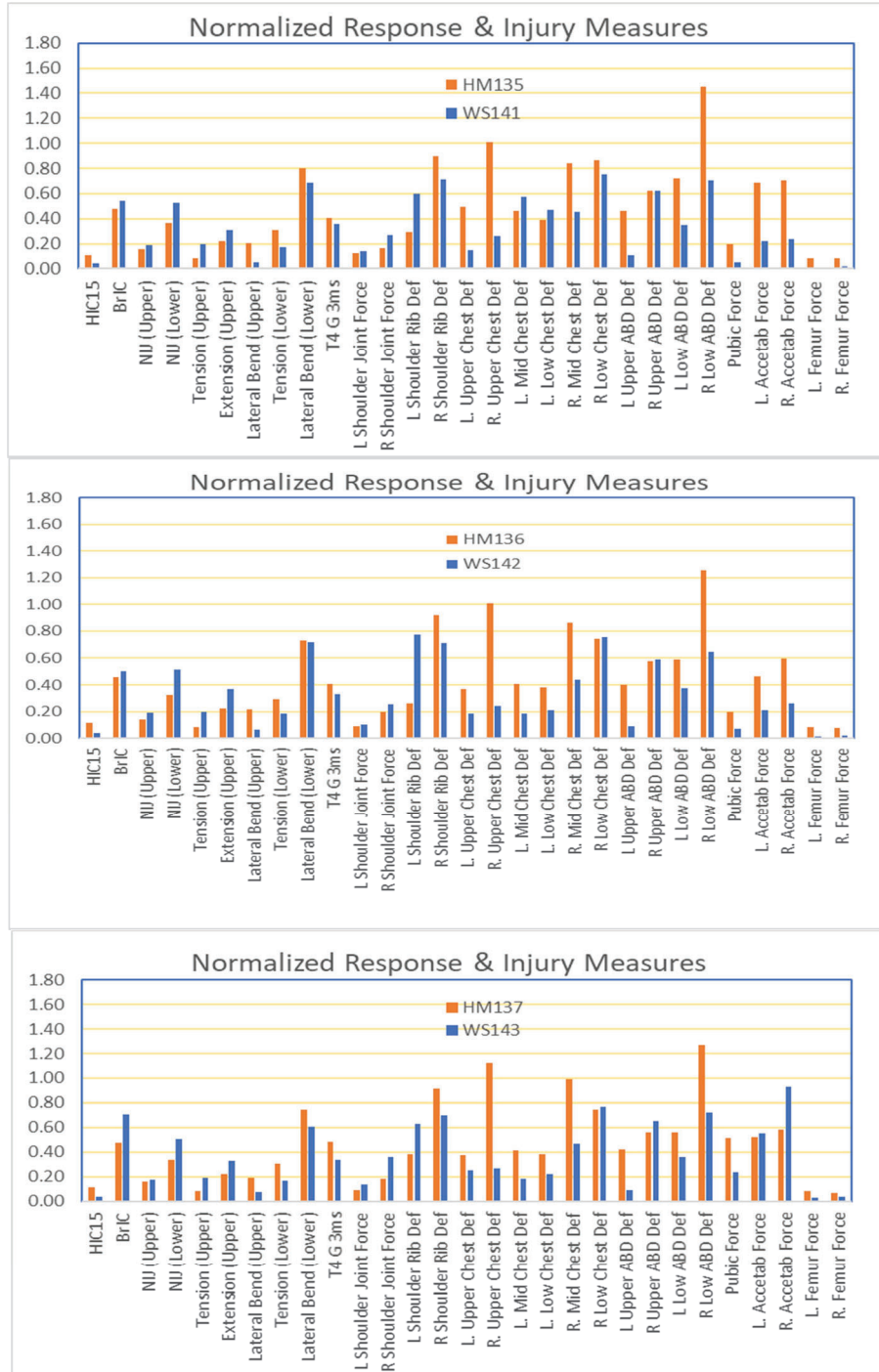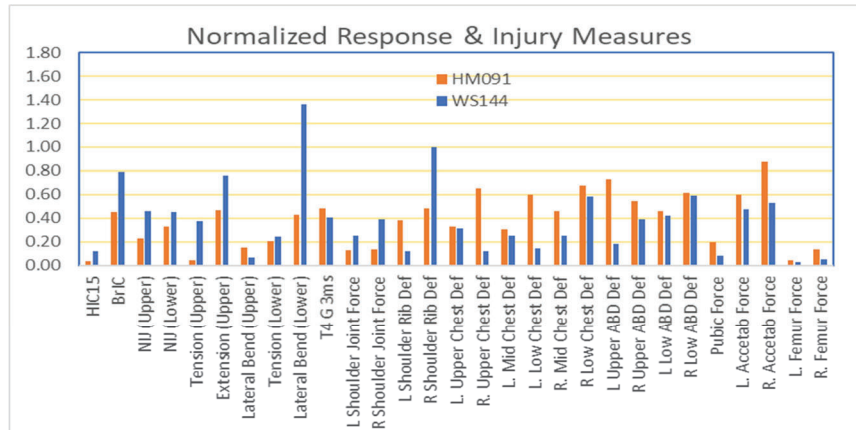
Figure 20. Comparison of the normalized responses and injury measures between the GHBMC M50-O model v6.0 and the WorldSid dummy model v7.6 for the four paired cases (C2-HM135/C9-WS141, C4-HM136/C10-WS142, C5-HM137/C11-WS143, and C3-HM091/C12-WS144).
(Blue: the WORLDSID dummy; Yellow: the HBM)

Table 9 compares the injury risks of the body regions for the four HBM simulation cases (HM135, HM136, HM 137, HM091) estimated with the GHBMC M50-O model v6.0 and the four paired WORLDSID-50M cases (WS141, WS142, WS144, WS143) estimated with the WORLDSID-50M model v1.8.1.

Table 9.
Comparison of HBM/WORLDSID-50M injury risks for the simulated far-side sled tests cases

Body Region	Measure	Risk	C2-HM135 60deg UVA Seat HBM Injury Risk	C4-HM136 60deg Prod Seat HBM Injury Risk	C5-HM137 60deg Prod SeatCC HBM Injury Risk	C3-HM091 90deg UVA Seat HBM Injury Risk	C9-WS141-60deg UVA Seat WSID Injury Risk	C10-WS142-60deg Prod Seat WSID Injury Risk	C11-WS143-60deg Prod Seat-CC WSID Injury Risk	C12-WS144-90deg UVA Seat WSID Injury Risk
Head	HIC	AIS3+	0.0%	0.0%	0.0%	0.0%	0.0%	0.0%	0.0%	0.0%
	BrIC	AIS 4+	0.0%	0.0%	0.0%	0.0%	0.1%	0.0%	9.8%	18.6%
Neck	Nt	AIS3+	0.0%	0.0%	0.0%	0.0%	0.0%	0.0%	0.0%	0.1%
	NIJ	AIS3+	0.5%	0.5%	0.5%	0.7%	6.0%	6.1%	5.8%	11.3%
Thorax	Max Thoracic rib Deflection	AIS3+	50.9%	49.7%	72.3%	5.2%	8.7%	8.8%	10.4%	49.6%
Abdomen	Max Abdomen rib Deflection	AIS2+	10.0%	5.7%	40.9%	0.0%	3.2%	1.6%	3.8%	0.7%
Pelvis	Max. Pubic Force (N)	AIS2+	2.2%	2.2%	9.0%	2.2%	0.0%	0.0%	0.1%	0.0%
KTH	Fz	AIS 2+	1.0%	1.0%	1.0%	1.2%	0.7%	0.7%	0.8%	0.8%
Whole Body	OIM		57.4%	54.3%	85.3%	9.1%	17.7%	16.4%	27.4%	64.2%

Vehicle Crash Far-side Occupant Simulations Results

Table C-1 in Appendix C lists the raw data of the calculated responses and injury measures calculated with the two occupant models (GHBMC AM50-O v6.0 HBM, and WorldSid-50M model v7.6) from the paired simulation cases in matrix III (Table 6) for the vehicle pole crash test. Table C-2 in Appendix C summarizes the maximum relative displacements of the kinematics targets of head, T1, T4, T12, pelvis, left and right shoulders and knees for the two cases. Detailed data analysis results are presented in the following sub-sections.

WORLDSID-HBM comparative analysis

Figure 21 shows snapshots of the GHBMC M50-O model v6.0 HBM kinematics at 0msec, 40msec, 80msec, and 150msec for the simulated vehicle pole crash test case C14-HM146 (Table 6) in comparison to the paired WORLDSID-50M dummy case C15-WS147 (Table 6), where the blue is for the WorldSid-50M dummy and the yellow for the human model (HBM). It is seen that the occupant represented with the HBM rotates far toward the right-hand side during the crash event.
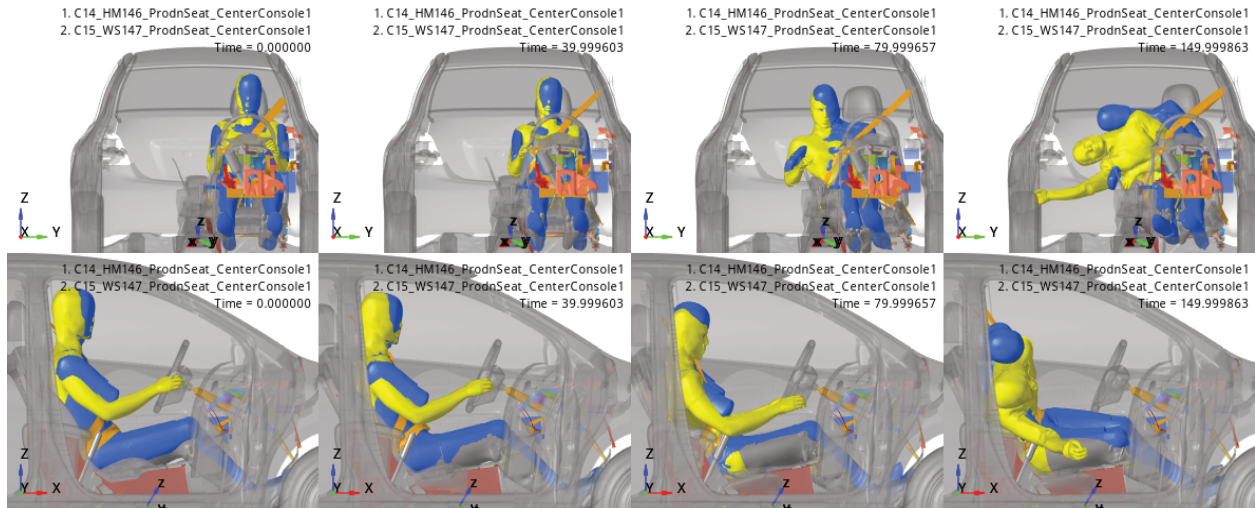
Figure 21. Snapshots of the kinematics of GHBMC M50-O model v6.0 in the simulated vehicle pole crash test case C14-HM146 in comparison to the paired WORLDSID-50M dummy case C15-WS147. (Blue: the WorldSid-50M dummy; Yellow: the HBM).

The WORLDSID-50M dummy model behaves similar kinematics like that from the lateral sled case C3-HM091 shown in Figure 19—the lateral excursion of the head/neck, shoulders and torso are less than the HBM for this vehicle crash case. Figure 22 further shows that the maximum relative displacement-Y of the head, T1, T4, T12, pelvis, and left and right shoulders and knees of the WORLDSID are all smaller than the HBM under the same FMVSS 214 subject vehicle pole crash condition.
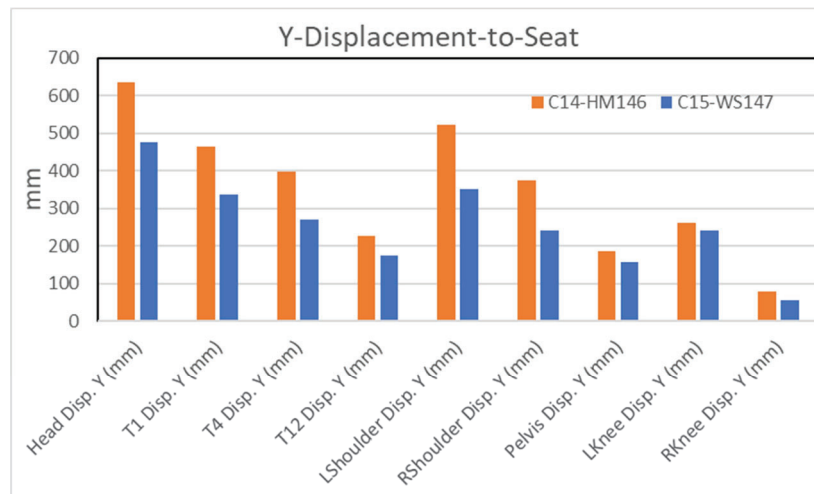
Figure 22. Comparison of the maximum relative lateral Y-displacements of the head, T1, T4, T12, pelvis, and left and right shoulders and knees between the WORLDSID and the HBM of the paired case (C14-HM146/C15-WS147) for the FMVSS 214 compact vehicle pole crash. (Blue: the WORLDSID dummy; Yellow: the HBM)

Figure 23 compares the normalized response and injury measures between the HBM and the WORLDSID-50M from the vehicle pole crash test simulations. The chest deflections from the WORLDSID-50M model are lower than that predicted with the HBM.
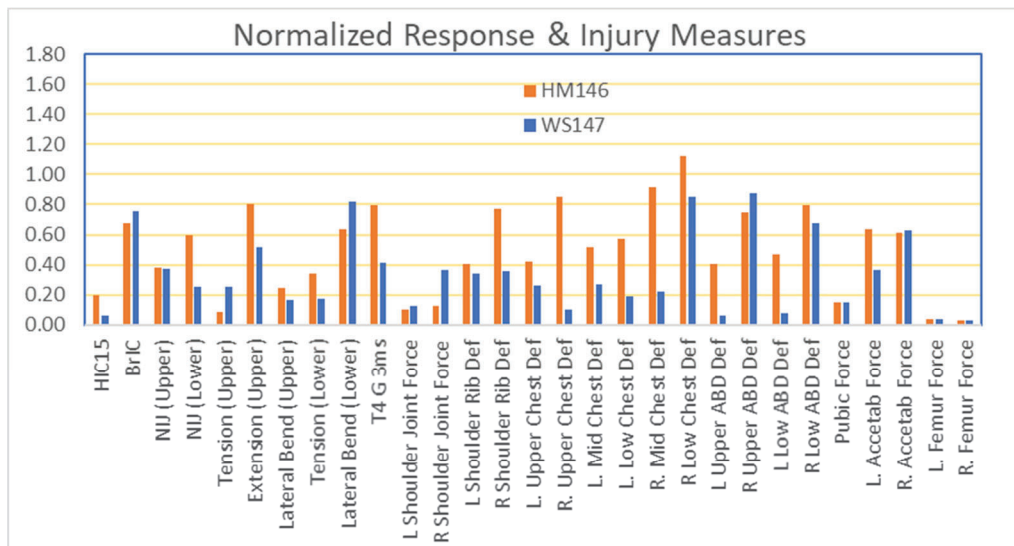
Figure 23. Comparison of the normalized response and injury measures between the AM50-O v6.0 HBM case C14-HM146 and the WorldSID-50M model v7.6 case C15-WS147 from the vehicle pole crash simulations. (Blue: the WORLDSID dummy; Yellow: the HBM)

Table 10 compares the body regions injury risks estimated with the GHBMC M50-O model v6.0 from the HBM vehicle crash simulation cases HM146 and the WORLDSID-50M model v7.6 from the paired WORLDSID-50M case WS147. The injury risks for all the other body regions are similar between the WorldSID and the HBM except for the chest where the WorldSID's estimated risk is lower than the HBM due to less chest deflections.

Table 10.
Comparison of HBM/WORLDSID-50M injury risks for the from the vehicle pole crash cases

Body Region	Measure	Risk	HM146- from Vehicle Pole Crash HBM Injury Risk	WS1147- from Vehicle Pole Crash WORLDSID Injury Risk
Head	HIC	AIS3+	0.1%	0.0%
	BrIC	AIS 4+	10.4%	14.9%
Neck	Nt	AIS3+	0.0%	0.0%
	NIJ	AIS3+	1.5%	9.3%
Thorax	Max Thoracic rib Deflection	AIS3+	73.4%	20.4%
Abdomen	Max Abdomen rib Deflection	AIS2+	12.2%	19.7%
Pelvis	Max. Pubic Force (N)	AIS2+	1.8%	0.0%
KTH	Fz	AIS 2+	0.8%	0.8%
Whole Body	OIM		80.0%	51.1%

DISCUSSIONS

Model Predicted Injury Risks Verification

Table 12 compares the model predicted injury risks with the PMHS post-test Autopsy examination results from the UVA far-side tests. For the PMHS 602 oblique sled test conditions, both the HBM and THOR model predicted high chest injury risk which is in line with the post-test observation. The WorldSID dummy model

underestimates the chest injury risk for this PMHS due to the lower chest deflections. For the PMHS 559 test condition, the WorldSID predicted high chest injury risk which is in line with the test outcomes while the HBM's prediction underestimates the risk. The cause is that the seatbelt slipping down the HBM body after ~80msec which lower the chest loading force for the HBM correlation case C3-HM091 as shown in Figure 9. This phenomenon may be occupant body shape dependent. This issue should be further investigated. The HBM correlation for the lateral sled case C3-HM09 will be improved.

Table 12.
Verification of HBM predicted injury risks with the Autopsy examination reported results

PMHS #	Body Region	Injury	AIS Code 2005 (1998 where different)	HBM Predicted Injury risk	WorldSID Predicted Injury risk	THOR Predicted Injury risk
PMHS 602	Thorax	Fractures of 5 Left ribs (L4, L5, L6, L7, L9) and 4 right ribs (R2, R3, R5, R6) (without flail)	450203.3 (450230.3)	AIS 3+ risk 57.4%	AIS 3+ risk 17.7%	AIS 3+ risk 54.3%
	Thorax	Sternum fracture* (note that this fracture involved one of the sternum instrument mount holes, thus may be artifactual)	450804.2			
	Lumbar Spine	Transverse process fracture, L2 left side	650620.2	NA	NA	NA
PMHS 559	Thoracic Spine	Vertebral body fracture (NFS), T10	650430.2	AIS 3+ risk 9.1%	AIS 3+ risk 64.2%	NA
	Thorax	Sternum fracture	450804.2			
	Thorax	Bilateral flail chest (by definition - ≥3 ribs fractured in more than one location, bilaterally)	450214.5 (450266.5)			

Kinematics & Response Differences between the HBM and the WorldSID Model

From the vehicle pole crash simulations, difference of the lateral movements of the WorldSID model and the HBM is observed during the vehicle crash event. The kinematics comparison is shown in Figure 21. Figure 22 indicates the less lateral displacements of the dummy targets than the HBM's. Figure 24 compares the external forces to the occupant between the HBM and the WorldSID-50M during the period of 130 msec. It is observed that the HBM has experienced larger contact force by the center console in the longer interaction duration even though the other external forces to the HBM from the seatbelt and seat are larger than the ATD. The larger console contact force causes much larger chest and abdominal deflections to the HBM. The WorldSID dummy model showed stiffer torso bending and earlier rebounce of the body away from the center console.
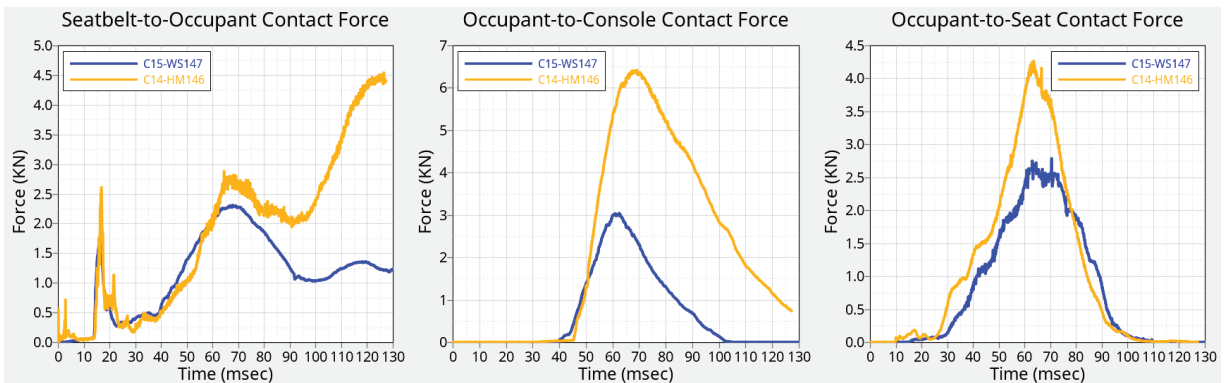
Figure 24. Comparison of the external forces to the occupant between the HBM case C14-HM146 and the WorldSID-50M case C15-WS147 from the vehicle pole crash simulations. (Blue: the WORLDSID dummy; Yellow: the HBM)

Kinematics & Response Differences between the HBM and the THOR Model

The THOR dummy model has the kinematics and response similar to the HBM from the simulated oblique sled tests, as shown in Figures 11 - 14. Major differences observed are the kinematics of the lower extremities. Compared to the HBM, the THOR lower legs have less lateral swing and upward movement in the oblique far-side

sled tests. Figure 25 shows comparison of the external forces to the occupant between the HBM and the WorldSID-50M during the period of 150 msec in the simulated far-side sled test S135 (14g pulse in 60deg), including the total seatbelt forces to the occcupant, and the forces from the foot plate to the left and right foot. Although all the relevant contact parameters such as the friction coefficients and penalty factors are defined same for those external contacts, the contact forces for the HBM and the WorldSID are still different. Compared to the HBM, the THOR dummy model has the longer duration in the right foot contact force and higher peak force to the left foot, which is mainly due to insufficient lift up motion of the THOR legs as compared to the observed from PMHS or the HBM in the test. This could indicate poor biofidelity of the THOR pelvis responding to the lateral inertia loads.
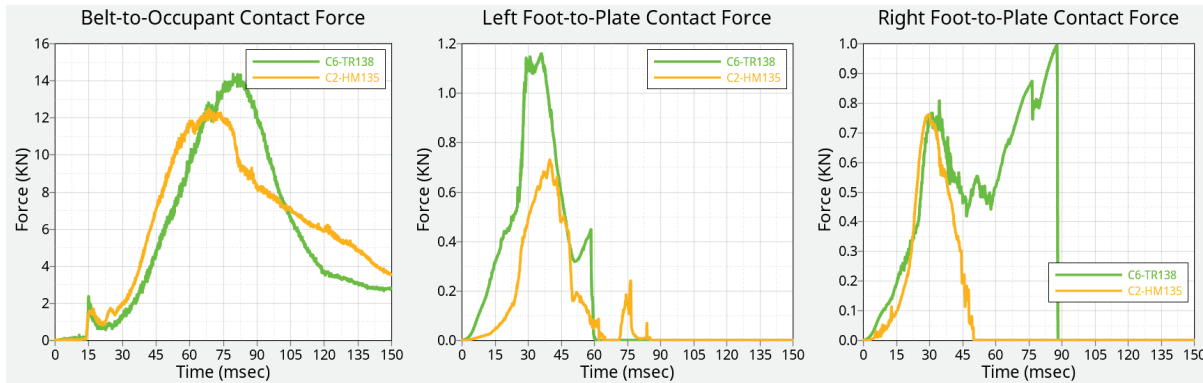
Figure 25. Comparison of the external forces to the occupant between the HBM case C2-HM135 and the THOR case C6-TR138 from the simulated far-side sled test S135 (14g pulse at 60deg).
(Yellow: the HBM; Green: the THOR)

Limitations of this Study

This study generates a large set of data from the thirteen sled test simulations and two vehicle crash occupant simulations with the HBM (the GHBMC AM50-O model v6.0), and the two ATD models (Humanetics WorldSID model v7.6 & THOR model v1.8.1). Although the two ATD models have been validated at some extent with other component and sled system level tests, the current simulated results with the ATDs are not validated directly with the physical far-side sled tests. This could be the next step for this study.

In this study, the results of the occupant body region injury risks predicted by the HBM and the ATDs show some inconsistence from case to case due to the differences of the kinematics and responses under the far-side crash loading conditions. As the kinematics and responses are mainly affected by the regular/non-regular restraints (seatbelt, seats, consoles, etc.) under the defined far-side crash mode, a larger set of restraint and environment component variants are not studied yet. More analysis and experimental verification for the restraint influence individually and comparably for the HBM and ATDs are helpful for identifying biofidelic deficiencies of the ATDs and improving the restraint performance as well. In addition, the injury risk functions for each of the mid-sized male occupant models used in this study could be further evaluated and improved.

CONCLUSIONS

The latest GHBMC 50th percentile male occupant model version v6.0 is validated with the PMHS tests under the two oblique (60deg) far-side sled tests varying the pulse severities from 6.6g to 14g. The HBM predicted high injury risks for the thorax under such test conditions are in line with the post-test PMHS injury observations.

For the 90deg lateral sled test under the 14g pulse, the HBM demonstrates reasonably biofidelic kinematic responses compared to the PMHS, although the case correlation can be further improved. It seems that for such a crash mode, the occupant body shape seems to have more influence on the seatbelt restraints which needs to be investigated.

The Humanetics mid-sized male THOR dummy v1.8.1 has similar head/neck/torso kinematic responses compared to the HBM in the oblique (60deg) far-side sled test condition. The swing and upward movements of the lower extremities are shown lagging behind the HBM from the simulated oblique far-side sled test, indicating poor biofidelity of the THOR pelvis and lower leg body regions responding to the lateral inertia loads.

The Humanetics mid-sized male WorldSID-50M model v7.6 has similar whole-body kinematics and responses to the HBM responding to the oblique far-side crashes. Responding to the lateral far-side loadings, the model has less body bending and thoracic rib deformations compared to the HBM, indicating a stiffer spine and thoracic ribcage.

ACKNOWLEDGEMENTS

REFERENCES

[1] FORMAN, J., Lopez-Valdes, F., et al. 2013. "Occupant kinematics and shoulder belt retention in far-side lateral and oblique collisions: a parametric study." Stapp Car Crash Journal, 57: pp.343–85.

[2] Diggers, K., Dalmotas, D., 2001. "Injuries to restrained Occupants in Far-side Crashes." In Proceedings of the 17th International Technical Conference on the Enhanced Safety of Vehicles, Amsterdam, 17-0351.

[3] Yoganandan, N., Pintar, F. A., Gennarelli, T. A., Maltese, M. R. 2000. "Patterns of abdominal injuries in frontal and side impacts." Annual Proceedings of the Association for the Advancement of Automotive Medicine, 44: pp.17–36.

[4] Gabler, H. C., Fitzharris, M., Scully, J., Fildes, B. N. 2005. "Far side impact injury risk for belted occupants in Australia and the United States. Proceedings of the 19th International Technical Conference on the Enhanced Safety of Vehicles, Washington D.C., 05-0420.

[5] Bahous, G., Murakhovskiy, D., Digges, K., Rist, H., Wiik, R. 2015. "Opportunities for reducing far-side casualties." Proceedings of the 24th International Technical Conference on the Enhanced Safety of Vehicles, Gothenburg, Sweden, 15-0444.

[6] Hosteler, Z. S., Fang, C. H., Barnard, R., Jones, D. A., Davis, M. L., Weave, A. A. 2021. "Injury Risk Curves in Far-side Lateral Motor Vehicle Crashes by AIS level, Body Region and Injury Code", in Traffic Injury Prevention, v21: pp 112-117.

[7] Euro NCAP, "Far Side Occupant Test & Assessment Procedure – Implementation 2023." 2022. in European New Car Assessment Programme version 2.3, 14th November 2022.

[8] Pintar, F. A., Yoganandan, N., et al. (2007). "Comparison of PMHS, WorldSID, and THOR-NT responses in simulated far side impact." Stapp Car Crash Journal, 51: pp. 313–360.

[9] Parent, D., Craig, M., Moorhouse, K. (2017). "Biofidelity Evaluation of the THOR and Hybrid III 50th Percentile Male Frontal Impact Anthropomorphic Test Devices". Stapp Car Crash Journal, 61: pp. 227-276.

[10] Rhule, H., Moorhouse, K., Donnelly, B., Stricklin, J. 2009. "Comparison of WorldSid and ES-2re Biofidelity Using an Updated Biofidelity Ranking System". In Proceedings of the 21st International Technical Conference on the Enhanced Safety of Vehicles, Stuttgart, Germany, 09-0562.

[11] Katagiri, M., Zhao, J., Kerrigan, J., Kent, R., Forman, J.. 2016. "Comparison of Whole-Body Kinematic Behavior of the GHBMC Occupant Model to PMHS in Far-Side Sled Tests." IRCOBI Conference 2016, IRC-16-88.

[12] Eppinger, R., et al., 1999, "Development of Improved Injury Criteria for the Assessment of Advanced Automotive Restraint Systems - II", NHTSA

[13] Eppinger, R., et al., 2000, "Supplement: Development of Improved Injury Criteria for the Assessment of Advanced Automotive Restraint Systems - II", NHTSA.

[14] Takhounts, E., Craig, JC., Moorhouse, K., and McFadden, J. 2013. "Development of Brain injury Criteria (BrIC)", Stapp Car Crash Journal Vol 57: 343-266.

[15] Laituri, T., et al., 2005, "Derivation and Evaluation of a Provisional, Age-Dependent, AIS3+ Thoracic Risk Curve for Belted Adults in Frontal Impacts", SAE World Congress, 2005-01-0297.

[16] Rouhana, S. W., El-Jawahri, R. E., Laituri. T.R., 2010. "Biomechanical Considerations for Abdominal Loading by Seat Belt Pretensioners", Stapp Car Crash Journal, Vol 54: pp. 381-406.

[17] Leport, T., Baudrit, P., Trosseille, X., Petit, P., Palisson, A., Vallancien, G., 2007. "Assessment of the Pubic Force as a Pelvic Injury Criterion in Side Impact". Stapp Car Crash Journal, Vol 51: pp. 467-488.

[18] Kuppa, S., et al., 2001, "Lowe Extremity Injuries and Associated Injury Criteria", 24th ESV Conference, Paper No. 457.

[19] Petitjean, A., Trosseille, X., Praxl, N., Hynd, D., Irwin, A. 2012. "Injury Risk Curves for the WorldSID 50th Male Dummy", Stapp Car Crash Journal 56: 323-347.

[20] Craig, M., Parent, D., Lee, E., Rudd, R., Takhounts, E., Hasija, V., 2020. "Injury Criteria for the THOR 50th Male ATD". from ISO/TR 19222:2021(en) https://www.iso.org/obp/ui/#iso:std:iso:tr:19222:ed-1:v1:en.

Appendix-A: Injury Risk Functions for the HBM and ATDs

The risk injury functions for the body regions and the whole body of the HBM, THOR dummy and WORLDSID-50M dummy were summarized in Table A-1, A-2 & A-3 below.

Table A-1.
The injury risk functions for the 50th%ile male HBM

Body Region	Injury Measure	Function	Reference
Head	HIC	$P(AIS\,3+) = \emptyset\left[\dfrac{\ln(HIC) - 7.45231}{0.73998}\right]$	[13]
	BrIC	$P(AIS\,3+) = 1 - e^{-\left(\frac{BrIC - 0.523}{0.531}\right)^{1.8}}$	[14]
Neck	Max. Upper Neck Tension, Nt (KN)	$P(AIS\,3+) = \dfrac{1}{1 + e^{(10.9745 - 2.375*Nt\,or\,Nc)}}$	[13]
	NIJ	$P(AIS\,3+) = \dfrac{1}{1 + e^{(6.047 - 5.44*NIJ)}}$	[20]
Thorax	Max Thoracic rib Deflection DC (mm)	$P(AIS\,3+) = \dfrac{1}{1 + e^{(12.597 - 0.05861*65 - 26.90118*CD/210)}}$	[15]
Abdomen	Max Abdomen Vmax*Cmax (1/Sec)	$P(AIS\,2+) = \dfrac{1}{1 + e^{(8.07533 - 2.77263*Vmax*Cmax)}}$	[16]
Pelvis	Max. Pubic Force, Fp (KN)	$P(AIS\,2+) = \dfrac{1}{1 + e^{(4.70 - 1.5*Fp)}}$	[17]
Thigh/Knee	Max. Femur Force, Fz (KN)	$P(AIS\,2+) = \dfrac{1}{1 + e^{(4.9795 - 0.326*Fz)}}$	[18]

Table A-2.
The injury risk functions for the WorldSID-50M dummy

Body Region	Injury Measure	Function	Reference
Head	HIC	$P(AIS\,3+) = \emptyset\left[\dfrac{\ln(HIC) - 7.45231}{0.73998}\right]$	[13]
	BrIC	$P(AIS\,3+) = 1 - e^{-\left(\frac{BrIC - 0.523}{0.531}\right)^{1.8}}$	[14]
Neck	NIJ	$P(AIS\,3+) = \dfrac{1}{1 + e^{(3.227 - 1.969*NIJ)}}$	[12]
Shoulder	Shoulder Rib Force, Fs (N)	$P(AIS\,3+) = 1 - e^{-\left(\frac{Fs}{2379.584}\right)^{7.409474}}$	[19]
Thorax	Max Thoracic rib Deflection CD (mm)	$P(AIS\,3+) = \dfrac{1}{1 + e^{(3.693638 - LN(CD)/0.123132)}}$	[19]
Abdomen	Max Abdomen Deflection ABD (mm)	$P(AIS\,3+) = 1 - e^{-\left(\frac{ABD}{52.3975}\right)^{8.611282}}$	[19]
Pelvis	Max. Pubic Force, Fp (N)	$P(AIS\,3+) = 1 - e^{-\left(\frac{Fp}{2456.761}\right)^{4.599182}}$	[19]
Thigh/Knee	Max. Femur Force, Fz (KN)	$P(AIS\,2+) = \dfrac{1}{1 + e^{(4.9795 - 0.326*Fz)}}$	[18]

Table A-3.
The injury risk functions for the THOR dummy

Body Region	Injury Measure	Function	Reference
Head	HIC	$P(AIS\ 3+) = \emptyset\left[\dfrac{\ln(HIC) - 7.45231}{0.73998}\right]$	[13]
	BrIC	$P(AIS\ 3+) = 1 - e^{-\left(\frac{BrIC - 0.523}{0.531}\right)^{1.8}}$	[14]
Neck	NIJ	$P(AIS\ 3+) = \dfrac{1}{1 + e^{(6.047 - 5.44*NIJ)}}$	[20]
Thorax	Max Thoracic rib Deflection DC (mm)	$P(AIS\ 3+) = 1 - e^{-\left(\frac{CD}{58.183}\right)^{2.977}}$	[20]
Abdomen	Max Abdomen Deflection DC (mm)	$P(AIS\ 3+) = 1 - e^{-\left(\frac{ABD}{106.222}\right)^{4.3127}}$	[20]
Pelvis	Max. Pubic Force, Fp (KN)	$P(AIS\ 2+) = \emptyset\left[\dfrac{\ln(1.429*F) - 1.6058}{0.2339}\right]$	[20]
Thigh/Knee	Max. Femur Force, Fz (KN)	$P(AIS\ 2+) = \emptyset\left[\dfrac{\ln(1.229*FLC) - 2.62}{0.3014}\right]$	[20]

Appendix-B: The Far-side Sled Test Simulation Matrix I & II Results

Table B-1.
Responses and injury measures of the occupant models (GHBMC AM50-O v6.0 HBM, WorldSid-50M model v7.6 & THOR model v1.8.1) of the sled simulation cases in matrix I & II

Body Region	Injury Measure	C1 HM 134	C2 HM 135	C3 HM 091	C4 HM 136	C5 HM 137	C6 TR 138	C7 TR 139	C8 TR 140	C9 WS 141	C10 WS 142	C11 WS 143	C12 WS 144	C13 WS 145
Head	**HIC15**	2.95	85.48	26.11	91.13	87.22	26.1	23.4	21.7	33.69	31.50	28.14	97.4	23.7
	BrIC	0.23	0.48	0.46	0.46	0.48	0.71	0.71	0.85	0.54	0.50	0.71	0.79	0.65
Neck	**NIJ (Upper)**	0.29	0.14	0.20	0.13	0.14	0.26	0.32	0.45	0.24	0.25	0.22	0.59	0.38
	NIJ (Lower)	0.31	0.36	0.33	0.32	0.34	0.64	0.72	0.73	0.79	0.77	0.75	0.68	0.85
	Tension (Upper)	0.08	0.36	0.19	0.33	0.34	0.84	0.86	0.87	0.84	0.82	0.79	1.57	0.82
	Extension (Upper)	2.98	5.53	11.72	5.55	5.52	4.58	13.72	21.49	10.88	12.79	11.43	26.59	14.21
	Lateral Bend (Upper)	10.67	20.78	14.88	21.57	19.17	84.33	70.72	70.46	7.38	9.79	10.67	10.32	15.14
	Tension (Lower)	0.49	1.28	0.84	1.22	1.29	0.98	0.96	0.90	0.73	0.76	0.70	1.01	0.60
	Extension (Lower)	36.27	79.78	43.19	73.25	74.25	7.85	9.85	25.03	103.62	107.34	91.20	204.30	89.22
	Lateral Bend (Lower)	20.00	24.18	28.89	24.34	28.87	118.0	101.9	101.1	21.64	19.81	20.01	24.36	23.51
Thorax	**T4 G 3ms**	0.18	0.25	0.26	0.18	0.18	20.53	19.70	35.20	0.31	0.22	0.31	0.57	0.49
	L Shoulder Joint Force	0.10	0.34	0.28	0.39	0.36	1.07	1.15	1.26	0.61	0.57	0.81	0.88	1.03
	R Shoulder Joint Force	12.83	20.01	26.24	17.85	26.12	0.86	0.39	0.36	23.99	30.9	25.27	4.79	29.99
	L Shoulder Rib Def	39.58	60.80	33.00	62.60	62.04	--	--	--	28.46	28.4	27.97	40.1	14.35
	R Shoulder Rib Def	16.98	33.46	22.08	24.97	25.29	--	--	--	5.85	7.48	10.10	12.4	17.43
	L. Upper Chest Def	30.19	68.87	44.54	68.50	76.07	43.76	43.84	43.18	10.30	9.61	10.60	4.81	3.86
	R. Upper Chest Def	23.38	31.25	20.96	27.59	28.04	37.51	33.21	34.51	22.90	7.37	7.40	10.0	9.10
	L. Mid Chest Def	22.94	26.44	40.41	26.02	26.17	--	--	--	18.72	8.37	8.82	5.80	5.76
	L. Low Chest Def	23.83	57.14	31.09	58.82	67.27	27.88	19.64	21.94	18.04	17.4	18.61	10.1	9.98

	R. Mid Chest Def	26.28	58.78	45.86	50.27	50.65	--	--	--	30.10	30.2	30.83	23.2	26.09
	R Low Chest Def	20.89	34.46	54.56	29.89	31.71	53.43	53.79	54.47	5.60	4.48	4.61	9.19	9.99
Abdomen	**L Upper ABD Def**	21.91	46.98	40.82	43.10	42.08	73.06	74.28	71.29	31.03	29.60	32.61	19.30	26.63
	R Upper ABD Def	28.30	53.91	34.49	44.27	41.95	63.11	65.04	67.61	17.66	18.84	18.03	20.98	23.50
	L Low ABD Def	47.18	109.00	46.13	94.20	94.94	--	--	--	35.26	32.45	35.92	29.50	37.84
	R Low ABD Def	0.27	0.54	1.08	0.38	0.43	--	--	--	33.69	31.50	28.14	97.35	23.72
	L Upper ABD Vmax*Cmax	0.17	0.42	0.73	0.35	0.33	--	--	--	--	--	--	--	--
	R Upper ABD Vmax*Cmax	0.27	0.65	0.53	0.49	0.51	--	--	--	--	--	--	--	--
	L Low ABD Vmax*Cmax	0.70	2.12	0.97	1.90	2.78	--	--	--	--	--	--	--	--
	R Low ABD Vmax*Cmax	0.20	0.60	0.62	0.61	1.59	--	--	--	--	--	--	--	--
Pelvis	**Pubic Force**	1.15	2.36	2.07	1.60	1.79	0.00	0.00	0.00	0.17	0.56	0.20	0.09	0.17
	L. Acetabulum Force	1.03	2.42	3.03	2.05	2.01	1.94	2.58	3.28	0.84	2.19	1.89	1.03	0.84
	R. Acetabulum Force	0.35	1.16	0.58	1.14	1.18	2.65	2.94	3.56	1.03	3.73	2.11	1.81	1.03
KTH	**L. Femur Force**	0.43	1.12	1.87	1.06	0.94	0.47	0.73	0.98	0.12	0.26	0.31	0.28	0.12
	R. Femur Force	2.95	85.48	26.11	91.13	87.22	0.33	0.35	0.38	0.19	0.37	0.52	0.36	0.19

Table B-2.

Kinematics target relative displacements of the occupant models (GHBMC AM50-O v6.0 HBM, WorldSid-50M model v7.6 & THOR model v1.8.1) of the sled simulation cases in matrix I & II

Target	C1	C2	C3	C4	C5	C6	C7	C8	C9	C10	C11	C12	C13
	HM 134	HM 135	HM 091	HM 136	HM 137	TR 138	TR 139	TR 140	WS 141	WS 142	WS 143	WS 144	WS 145
Head Disp. Y (mm)	280.8	447.9	702.2	436.1	439.2	490.5	492.7	540.8	447.8	467.9	490.9	446.4	700.3
T1 Disp. Y (mm)	245.1	417.5	558.2	426.8	413.6	483.8	472.2	455.0	401.4	402.1	393.3	259.0	525.7
T4 Disp. Y (mm)	215.4	376.2	518.3	383.7	366.8	458.1	446.9	415.4	385.3	374.4	338.4	221.2	463.7
T12 Disp. Y (mm)	171.9	277.9	380.8	291.1	263.2	346.8	325.8	265.9	332.6	295.8	235.0	176.6	317.1
LShoulder Disp. Y (mm)	215.5	364.0	568.9	373.2	360.2	453.1	441.3	464.0	368.3	372.0	391.1	250.2	542.5
RShoulder Disp. Y (mm)	213.7	350.7	499.5	351.4	337.0	398.2	377.9	370.9	372.4	363.5	297.0	200.0	428.2
Pelvis Disp. Y (mm)	188.4	308.0	309.0	290.3	243.1	286.5	268.7	227.3	346.6	303.6	204.2	255.3	267.8
LKnee Disp. Y (mm)	294.4	563.9	495.6	526.2	387.6	526.9	375.6	365.1	700.0	703.7	543.2	792.8	790.2
RKnee Disp. Y (mm)	282.0	492.7	241.2	469.7	223.2	369.0	286.0	215.0	557.2	536.3	330.3	561.1	594.1

Appendix-C: The FMVSS214 Compact Car Pole Crash Far-side Occupant Simulation Matrix III Results

Table C-1.
Responses and injury measures of the occupant models (GHBMC AM50-O v6.0 HBM, WorldSid-50M model
v7.6 & THOR model v1.8.1) of the sled simulation cases in matrix III

Body Region	Injury Measure	C14	C15
		HM146	WS147
Head	HIC15	161.25	51.25
	BrIC	0.68	0.76
Neck	NIJ (Upper)	0.34	0.48
	NIJ (Lower)	0.60	0.38
	Tension (Upper)	0.37	1.05
	Extension (Upper)	20.13	18.16
	Lateral Bend (Upper)	24.27	24.48
	Tension (Lower)	1.43	0.72
	Extension (Lower)	63.97	123.39
	Lateral Bend (Lower)	47.82	24.60
Thorax	T4 G 3ms	0.202	0.29
	L Shoulder Joint Force	0.249	0.82
	R Shoulder Joint Force	27.51	13.56
	L Shoulder Rib Def	52.28	14.24
	R Shoulder Rib Def	28.90	10.41
	L. Upper Chest Def	58.17	4.02
	R. Upper Chest Def	35.07	10.96
	L. Mid Chest Def	38.68	7.55
	L. Low Chest Def	62.05	8.99
	R. Mid Chest Def	76.54	33.99
	R Low Chest Def	30.55	3.17
Abdomen	L Upper ABD Def	56.09	43.95
	R Upper ABD Def	35.47	4.04
	L Low ABD Def	59.72	33.75
	R Low ABD Def	0.52	51.25
	L Upper ABD Vmax*Cmax	0.66	--
	R Upper ABD Vmax*Cmax	0.60	--
	L Low ABD Vmax*Cmax	2.20	--
	R Low ABD Vmax*Cmax	0.48	--
Pelvis	Pubic Force	2.19	1.48
	L. Accetab Force	2.11	2.52
	R. Accetab Force	0.51	0.41
KTH	L. Femur Force	0.41	0.32
	R. Femur Force	161.25	0.37

Table C-2.
Kinematics target relative displacements of the occupant models (GHBMC AM50-O v6.0 HBM, WorldSid-50M model v7.6 & THOR model v1.8.1) of the sled simulation cases in matrix III

Target	C14	C15
	WS 146	WS 147
Head Disp. Y (mm)	635.5	476.6
T1 Disp. Y (mm)	465.4	336.7
T4 Disp. Y (mm)	399.0	271.0
T12 Disp. Y (mm)	228.2	174.9
LShoulder Disp. Y (mm)	521.9	353.1
RShoulder Disp. Y (mm)	373.7	240.6
Pelvis Disp. Y (mm)	185.6	157.4
LKnee Disp. Y (mm)	261.3	243.1
RKnee Disp. Y (mm)	78.5	56.2